Full title: Dynamic metabolic reprogramming in dendritic cells: an early response to influenza infection that is essential for effector function

Short Title: Metabolic rewiring is vital for influenza infected dendritic cells

Svetlana Rezinciuc[1], Lavanya Bezavada[1], Azadeh Bahadoran[1], Susu Duan[6], Ruoning Wang[2], Daniel Lopez-Ferrer[3], Erika E. Zink[4], David Finklestein[5], Douglas R. Green[6], Ljiljana Pasa-Tolic[4], Paul G. Thomas[6] & Heather S. Smallwood[1*]

[1]Department of Pediatrics, University of Tennessee Health Science Center, Memphis, Tennessee, United States of America

[2]Center for Childhood Cancer and Blood Disease, The Research Institute at Nationwide Children's Hospital, The Ohio State University School of Medicine, Columbus, Ohio, United States of America.

[3]Chromatography and Mass Spectrometry Division, Thermo Fisher Scientific. 355 River Oaks Parkway, CA 95134.

[4]Environmental Molecular Sciences Laboratory, Pacific Northwest National Laboratory, Richland, Washington, United States of America.

[5]Biostatistics Department, St. Jude Children's Research Hospital, Memphis, Tennessee, United States of America.

[6]Department of Immunology, St. Jude Children's Research Hospital, Memphis, Tennessee, United States of America.

*Corresponding author

E-mail: hsmallwo@uthsc.edu (HS)

Abstract

Infection with the influenza virus triggers an innate immune response aimed at initiating the adaptive response to halt viral replication and spread. However, the metabolic response fueling the molecular mechanisms underlying changes in innate immune cell homeostasis remain undefined. Thus, we compared the metabolic response of dendritic cells to that of those infected with active and inactive influenza A virus or treated with toll like receptor agonists. While influenza infects dendritic cells, it does not productively replicate in these cells, and therefore metabolic changes upon infection may represent an adaptive response on the part of the host cells. Using quantitative mass spectrometry along with pulse chase substrate utilization assays and metabolic flux measurements, we found global metabolic changes 17 hours post infection, including significant changes in carbon commitment via glycolysis and glutaminolysis, as well as ATP production via TCA cycle and oxidative phosphorylation. Influenza infection of dendritic cells led to a metabolic phenotype, distinct from that induced by TLR agonists, with significant resilience in terms of metabolic plasticity. We identified Myc as one transcription factor modulating this response. Restriction of either Myc activity or mitochondrial substrates resulted in significant changes in the innate immune functions of dendritic cells, including reduced motility and T cell activation. Transcriptome analysis of inflammatory dendritic cells isolated following influenza infection showed similar metabolic reprogramming occurs *in vivo*. Thus, early in the infection process dendritic cells respond with global metabolic restructuring that is present in lung DC 9 days following infection and impacts their effector function, suggesting that metabolic switching in dendritic cells plays a vital role in initiating the immune response to influenza infection.

Author Summary

In response to influenza infection we found that dendritic cells, cells that are critical in mounting an effective immune response, undergo a profound metabolic shift. They alter the concentration and location of hundreds of proteins, including c-MYC, mediating a shift to a highly glycolytic phenotype that is also flexible in terms of fueling respiration. Dendritic cells initiate the immune response to influenza and activate the adaptive response allowing viral clearance and manifesting immune memory for protection against subsequent infections. We found that limiting access to specific metabolic pathways or substrates diminished key immune functions. Previously we described an immediate, fixed, hypermetabolic state in infected respiratory epithelial cells. We now show the metabolic responses of epithelial and dendritic cells are distinct. Here, we also demonstrate that dendritic cells tailor their metabolic response to the pathogen or TLR stimulus. This metabolic reprogramming occurs rapidly *in vitro* and it is sustained in inflammatory dendritic cells *in vivo* for at least 9 days following influenza infection. Thus, drugs targeting metabolism are likely to have cell- and pathogen-specific activities in the context of infection. These studies open the possibility of modulating the immune response to viral infection via customizing metabolic therapy to enhance or diminish the function of specific cells.

Introduction

The influenza virus is associated with significant disease burden in the human population and is of particularly high risk to children, the elderly, and those with certain medical conditions, such as pregnancy, obesity, or metabolic disease. In a productive infection, the influenza virus co-opts the host cell's molecular machinery to induce a virus centric shift in macromolecular production for budding virions. In connection to this, we have previously shown influenza A virus infection of human respiratory epithelial cells leads to a fixed hypermetabolic state[1]. Dendritic cells are dispersed throughout the respiratory tract (including the lung parenchyma, alveolar space, and the airway epithelium), are a heterogeneous population with respect to surface phenotype and function, and are constantly surveying and sampling for pathogens or foreign material at this delicate barrier between the environment and blood stream [2-5]. Following IAV infection, dendritic cells have a critical role linking the innate and adaptive immune responses. These antigen presenting cells are dependent on the binding of different pattern-recognition receptors binding to pathogen-associated molecules such as toll-like receptors (TLRs), typically engaged on the cell surface or in endosomes. Influenza is sensed intracellularly by TLR3, TLR7, TLR8, and TLR9, sensing either viral envelope proteins or nucleic acids, respectively [6-12]. These TLRs are expressed at variable levels in human and murine cells of the upper respiratory tract, such as epithelial cells, macrophages, and dendritic cells [13]. Combined stimulation of these intracellular receptors tailor the antiviral response via retinoic acid-inducible gene-I (RIG-I) and NOD-like receptors, or lack thereof, creating a cell-specific response to influenza infection [13]. One molecular driver underpinning immune activation is an increase in metabolism to fuel effector functions requisite for pathogen elimination [14-17]. Recently, seminal papers in the field have demonstrated that activation of dendritic cells with the TLR4 agonist lipopolysaccharide (LPS) has profound metabolic consequences that may correlate to altered immune function [17-

97 19]. However, the metabolic response of dendritic cells to influenza infection remains undefined,
98 as does its relationship to TLR stimulation and inactive virus.

99 To gain a better understanding of the molecular events that initiate the systemic immune
100 response to influenza infection, we performed quantitative proteomics on influenza A virus strain
101 A/Puerto Rico/8/1934 H1N1 (IAV) infected and uninfected bone marrow derived dendritic cells
102 (DC) that were differentiated *in vitro*. Given that cellular location is pivotal to metabolic enzyme
103 activity, we divided the DC proteins into soluble and insoluble fractions to increase proteome
104 coverage while defining protein redistribution in response to infection. We found that metabolic
105 pathways dominated the enriched protein networks, accompanied by localization changes in
106 metabolic enzymes in response to IAV infection. The functional impact of these abundance and
107 localization changes were determined with pulse chase experiments using labeled metabolic
108 substrates, bioenergetics, and metabolite quantification. Similar to our previous findings in
109 epithelial cells[1], we identified upregulation of the transcription factor c-MYC and found that c-
110 MYC inhibition restored infected DC bioenergetics to quiescent levels. However, unlike IAV-
111 infected epithelial cells, infected DC increased their metabolic plasticity by reprogramming
112 glycolysis, glutaminolysis, and respiration better adapting to use diverse fuels to meet the
113 challenges of high energy demand and anabolism needed for activation. To dissect the DC
114 response to specific activation pathways, we quantified metabolic flux rates in response to TLR3,
115 4, or 7/8 agonists, genome replication-incompetent virus, and wild type virus. Intriguingly, DC
116 displayed treatment specific differences in glycolysis and mitochondrial respiration concomitant
117 to differences in coupling efficiency and ATP production. The response of DC to viral infection
118 induced a consistent and robust increase in glycolysis that was decoupled from the canonical
119 TCA cycle. Our results revealed that IAV-infected DC rely on glycolysis and glutamine over
120 pyruvate utilization. Further, we analyzed changes in infected DC motility, phagocytosis, and T
121 cell activation and found that inhibiting c-MYC activity or import of specific mitochondrial

122 substrates significantly reduced key immune functions. We then determined that this metabolic
123 reprogramming occurs in inflammatory lung dendritic cells 9 days following infection and results
124 in a very significant increase in glycolytic enzymes over those in the TCA cycle. Thus, in response
125 to IAV infection, global protein expression and localization changes occur in DC and are
126 associated with controlled metabolic restructuring that is necessary for DC function.
127 Consequently, loss of metabolic homeostasis in dendritic cells or their lung microenvironment
128 may have profound functional consequence for the overall immune response to influenza
129 infection.

130 # Results

131 **Influenza induces significant changes in DC metabolic proteins and pathways**

132 Two quantitative labeling strategies were used to determine proteomic changes after
133 influenza virus infection. We infected in vitro differentiated DC with the PR8 mouse-adapted H1N1
134 influenza strain A/Puerto Rico/68/34 (IAV) at a multiplicity-of-infection (MOI) of 5 for 17 hours. In
135 mouse DC, IAV replication is abortive (i.e. IAV replicates and virions build up intracellularly instead
136 of being released) and has a much lower infectivity rate than in human DC [20-22]. Thus, we
137 used a higher MOI than in our previous studies and validated effective infection of DC at this time
138 point, as determined by viral protein production (S1A Fig). After cells were harvested, soluble and
139 insoluble fractions were subjected to specialized trypsinization strategies to enhance coverage of
140 proteins with complex tertiary structures (i.e., either filter-aided sample preparation (FASP)
141 digestion, isobaric tags for relative and absolute quantitative (iTRAQ) labeling, or several rounds
142 of high intensity focused ultrasound (HIFU) and pressurization followed by stable isotope labeling
143 (SIL) (S1B Fig). The entire DC proteome (soluble and insoluble fractions ± infection) are publicly
144 available at the Proteomics Identifications (PRIDE) repository (PRIDE access number made
145 available on acceptance for publication). Approximately 25,000 peptides were detected with

146 corresponding reporter ions; of these, 7520 mapped to National Center for Biotechnology
147 Information (NCBI) reference sequence accession numbers (Table A S1 File). Of the 7,520
148 peptides, 70% had 2 or more peptide hits and were included in the quantitative analysis: 72% of
149 the proteome did not change, and 28% responded to infection with ≥ 2-fold change in peptide
150 abundance (Table 1). Most dynamic changes occurred in the insoluble fraction, with 855 proteins
151 increased and 649 decreased after IAV infection (Table 1 and S1C Fig).

152 **Table 1. Net changes in DC proteins in response to IAV infection after 17 hours.**

Fraction	Up	No Change	Down	Total
Insoluble	**855**	**2547**	**649**	**4051**
Soluble	**239**	**2003**	**427**	**2669**
Both	**74**	**1103**	**64**	**1241**

153 **Table 1 iTRAQ and SIL analysis of influenza virus infected BMDC.** The intensities of the
154 isobaric tag reporter ions were quantified by using the MASIC tool with the exclusion of missing
155 reporter-ion channels or by calculating the SIL ratio for each peptide pair after accounting for
156 singly or doubly labeled species in the $^{16}O/^{18}O$ ratio and correcting for labeling efficiency. Then,
157 the MS/MS data were searched and filtered by using 0.5% FDR; peptides passing the filter were
158 quantified then peptides-to-protein rollup was performed.
159
160 To validate the iTRAQ results, we used the well-established SIL method ($^{16}O/^{18}O$ labeling)
161 and HIFU with the same infection protocol [23]. This technique identified more than 20,000
162 peptides, resulting in about 10,000 unique International Protein Index accession numbers, and
163 2000 protein identifications. As in the iTRAQ DC proteomes, the majority (73%) of DC peptides
164 remained unaltered by IAV infection, which induced ≥2-fold change in the abundance of 27% of
165 DC proteins (Table A S1 File). Similar to the iTRAQ proteome, SIL samples had more changes in
166 the insoluble fraction. Although iTRAQ provided expanded coverage of the DC proteome, more
167 than half of all peptides identified by using SIL were also present in the iTRAQ data sets, with
168 similar trends (S1C Fig). Next, we used bioinformatic tools to identify the major pathways altered
169 by influenza. Proteomic data were segregated into increasing and decreasing sectors of ≥2-fold
170 change. iTRAQ and SIL proteomes were combined, and the most significant peptides were
171 selected. The lists of upregulated and downregulated proteins were submitted to the Database

172 for Annotation, Visualization, and Integrated Discovery (DAVID) v6.8 and queried for enrichment
173 groups [24]. 17 hours following IAV infection of DC, we found that metabolism accounts for the
174 majority of KEGG Orthology (KO) Class processes and was significantly enriched in both the
175 decreasing and increasing proteomes (Fig 1A & B respectively). Surprisingly, only a small fraction
176 (8.6% up and 11% down) of the enriched pathways were in the immune system or infectious
177 disease KEGG KO subclasses in the BRITE hierarchy (Table B S1 File).

178 A global view of influenza-induced changes in the abundance and localization of metabolic
179 proteins is depicted in Figure 1C, represented as previously described [25]. In this network
180 summary of metabolic protein dynamics, KO metabolic class proteins were organized based on
181 location in the soluble or insoluble fraction (Fig 1C left and right, respectively). Metabolic proteins
182 with relative expression changes of two-fold or greater were connected to their location in the
183 soluble or insoluble fraction by red or blue edges (up or down, respectively). Each protein node
184 is colored by KEGG subclass with significantly enriched KEGG metabolic pathways delineated in
185 the legend. Protein coverage per pathway and statistical information for pathway enrichment is
186 provided in Supplementary File 1 Tables B and C. Thus, the circle size of each KEGG metabolic
187 class is proportional to the number of proteins with significant fold changes in it (Fig 1C). We
188 found many of the proteins with significant abundance changes were involved in carbohydrate
189 metabolism (Fig 1C red nodes and S2D Fig). In the insoluble increased proteome, we found
190 carbohydrate metabolism had the largest number of proteins dispersed in several significantly
191 enriched KEGG pathways such as glycolysis, pentose phosphate pathway, fructose/mannose,
192 galactose, starch/sucrose, amino sugar/nucleotide metabolism, as well as carbon metabolism in
193 general (Fig 1C red nodes with red edges). Indeed, in the increased proteome, carbohydrate
194 metabolism accounted for 47% of the significantly enriched pathways, including glycolysis. On
195 the other hand, in the insoluble decreased proteome, carbohydrate metabolism had fewer
196 proteins, and these were associated with TCA cycle, glyoxylate/dicarboxylate, and propanoate

197 metabolism (Fig 1C red nodes blue edges). This differential expression of proteins controlling
198 carbon metabolism may indicate uncoupling of glycolysis from oxidative phosphorylation
199 (OXPHOS).

200 We identified 432 differentially expressed metabolic proteins (i.e. ≥2-fold abundance changes)
201 that mapped to well-known metabolic pathways (Table 2 and Table B S1 File). Significant
202 enrichment of glycolysis in the KEGG analysis led us to more closely examine protein changes in
203 this pathway. Coverage for glycolytic proteins was complete in both fractions. We found that most
204 soluble glycolytic proteins in this network increased (S1C Fig green). The insoluble fraction had
205 fewer proteins that increased two-fold or more, which is not surprising given that glycolysis occurs
206 in the cytosol. Some proteins increased in both fractions, including α-Enolase. α-Enolase is a
207 glycolytic protein that also rapidly increases and dimerizes at the surface of activated monocytes
208 to form a plasminogen receptor critical for immune cell recruitment to the lung [26]. We validated
209 α-Enolase increase in both soluble and insoluble fractions with western blots (S1C Fig).

210 Related to but not contingent upon expression levels, metabolic proteins are also
211 regulated by changes in subcellular location [25, 27-30]. In response to infection, we detected 48
212 metabolic proteins that relocalized from the soluble to insoluble fraction or vice versa (Table 2).
213 Some of the proteins undergoing localization changes were associated with metabolic pathways.
214 For example, we found proteins involved in valine, leucine, and isoleucine degradation were
215 decreased in the insoluble proteome while increased in the soluble (Fig 1C orange nodes and
216 Table B & C S1 File). Conversely, we found key players in the biosynthesis of amino acids
217 decreased in the soluble and increased in the insoluble fractions (Fig 1C orange nodes and Table
218 B & C S1 File). We also found metabolic pathways that were uniformly altered irrespective of
219 location such as the fatty acid degradation pathway (Fig 1C yellow nodes and Table C S1 File).
220 Taken together, these results demonstrate that in response to IAV infection, DC coordinate
221 changes in metabolic protein abundances and location.

Table 2. Infection induced changes in the relative abundance of DC metabolic proteins

	Protein	Fraction	FC
Glycolysis	aldehyde reductase	Insol	2
	aldehyde reductase	Sol	-2
	aldolase	Insol	2
	enolase	Insol	5
	galactose mutarotase	Insol	2
	galactose mutarotase	Sol	-1
	glucose phosphate isomerase	Insol	2
	glucose phosphate isomerase	Sol	-1
	hexokinase	Insol	2
	hexokinase	Sol	1
	phosphofructokinase	Insol	2
	phosphofructokinase	Sol	-2
	phosphoglucomutase	Insol	3
	phosphoglucomutase	Sol	-1
	phosphoglycerate kinase	Insol	2
	phosphoglycerate kinase	Sol	-1
	phosphoglycerate mutase	Insol	2
	phosphoglycerate mutase	Sol	1
	pyruvate kinase	Insol	2
	pyruvate kinase	Sol	1
	triosephosphate isomerase	Sol	1
	triosephosphate isomerase	Insol	2
TCA Cycle	citrate synthase	Insol	-2
	dihydrolipoamide dehydrogenase	Insol	-2
	dihydrolipoamide dehydrogenase	Sol	-2
	isocitrate dehydrogenase	Insol	-2
	isocitrate dehydrogenase	Sol	2
	isocitrate dehydrogenase	Insol	-2
	malate dehydrogenase	Insol	-2
	malate dehydrogenase	Sol	1
	oxoglutarate dehydrogenase	Insol	-2
	pyruvate dehydrogenase	Insol	-2
	pyruvate dehydrogenase	Insol	-2
	succinate dehydrogenase	Insol	-3
	succinate-CoA ligase	Insol	-2
	succinate-CoAligase	Insol	-2
Fatty Acid Beta oxidation	acetyl-CoAacyltransferase	Insol	-6
	acetyl-CoAacyltransferase	Sol	-2
	acyl-CoA synthetase	Insol	1
	acyl-CoA synthetase	Sol	-2
	acyl-CoAdehydrogenase	Insol	-2
	acyl-CoAdehydrogenase	Sol	-1
	acyl-CoAoxidase	Insol	1
	acyl-CoAoxidase	Sol	-2.5
	aldehyde dehydrogenase	Sol	-2
	aldehyde dehydrogenase	Insol	-2
	dodecenoyl-Co A δ isomerase	Insol	-2
	enoyl CoAhydratase	Insol	-2
	enoyl CoAhydratase	Sol	-1
	hydroxyacyl-Co A dehydrogenase	Insol	-2

	Protein	Fraction	FC
Oxidative Phosphorylation	ATPase 16 kDa proteolipid subunit	Insol	2
	ATP synthase beta subunit	Sol	-0.5
	ATP synthase alpha subunit	Insol	-2
	ATP synthase alpha subunit	Sol	-3
	ATP synthase subunit f	Insol	5
	ATP synthase, subunit b	Insol	-3
	ATPase	Insol	3
	ATPase	Sol	-2.5
	ATPase subunit A1	Sol	-3
	ATPase subunit C	Insol	2
	ATPase subunit C1	Sol	2
	ATPase subunit D1	Sol	-2
	ATPase subunit D2	Sol	-3
	ATPase subunit F	Insol	2
	ATPase subunit H	Sol	-2
	cytochrome c oxidase	Insol	2
	NADH dehydrogenase A6	Insol	2
	NADH dehydrogenase S8	Insol	2
	NADH dehydrogenase S2	Insol	2
	NADH dehydrogenase S3	Insol	2
	NADH dehydrogenase A2	Insol	1
	NADH dehydrogenase 4	Insol	3
	NADH dehydrogenase	Insol	2
	NADH-ubiquinone oxidoreductase	Insol	3
	pyrophosphatase	Insol	2
	pyrophosphatase	Sol	-1
	ubiquinol-cytochrome c reductase	Insol	-2
Pentose Phosphate Cycle	2-deoxy-D-ribose 5-phosphate aldolase	Insol	2
	2-deoxy-D-ribose 5-phosphate aldolase	Sol	1
	6-phosphogluconolactonase	Insol	2
	6-phosphogluconolactonase	Sol	-2
	aldolase	Insol	1.5
	aldolase	Sol	2
	glucose phosphate isomerase	Insol	2
	glucose phosphate isomerase	Sol	-1
	glucose-6-phosphate dehydrogenase	Insol	2
	glucose-6-phosphate dehydrogenase	Sol	2
	GTPase	Sol	1
	phosphofructokinase	Insol	1.5
	phosphofructokinase	Sol	1
	phosphoglucomutase	Insol	3
	phosphoglucomutase	Sol	-1
	phosphogluconate dehydrogenase	Insol	3
	phosphogluconate dehydrogenase	Sol	-1
	ribulose-5-phosphate-3-epimerase	Insol	2
	ribulose-5-phosphate-3-epimerase	Sol	1
	transaldolase	Insol	2
	transketolase	Insol	2

	Protein	Fraction	FC
Biosynthesis of Amino Acids	3-phosphoglycerate dehydrogenase	Insol	1
	3-phosphoglycerate dehydrogenase	Sol	-3
	aconitase	Insol	2
	aconitase	Sol	-1
	aldolase	Insol	1.5
	aldolase A	Sol	2
	aldolase C	Sol	2
	aminoacylase	Insol	2
	aminoacylase	Sol	-1
	aminotransferase	Sol	2
	arginase	Sol	1
	arginase	Insol	3
	argininosuccinate lyase	Insol	2
	argininosuccinate lyase	Sol	-2
	argininosuccinate synthetase	Sol	-2
	argininosuccinate synthetase	Insol	-1
	branched chain aminotransferase	Insol	1
	enolase	Insol	5
	glutamate oxaloacetate transaminase	Sol	-2
	glutamate oxaloacetate transaminase	Insol	2
	glutamine synthetase	Insol	1
	glutamine synthetase	Sol	-2
	isocitrate dehydrogenase	Insol	1
	isocitrate dehydrogenase	Sol	1
	methionine adenosyltransferase	Insol	3
	methionine adenosyltransferase	Sol	-1
	phosphofructokinase	Insol	1.5
	phosphofructokinase	Sol	1
	phosphoglycerate kinase	Insol	2
	phosphoglycerate kinase	Sol	-1
	phosphoglycerate mutase	Insol	2
	phosphoglycerate mutase	Sol	1
	pyruvate kinase	Insol	2
	pyruvate kinase, muscle	Sol	-1
	ribulose-5-phosphate-3-epimerase	Insol	2
	ribulose-5-phosphate-3-epimerase	Sol	1
	serine hydroxymethyltransferase	Insol	-2
	serine hydroxymethyltransferase	Sol	-3
	transaldolase	Insol	2
	transaldolase	Sol	-1
	transketolase	Insol	2
	transketolase	Sol	-1
	triosephosphate isomerase	Insol	2
	triosephosphate isomerase	Sol	1

224 **Table 2. Infection induced changes in DC protein abundance and localization.** Influenza
225 virus strain A/PuertoRico/68/34 (IAV) was added to DC for 2 hours, infection medium replaced,
226 and the infection proceeded for 17 hours followed by cell lysis and protein extraction. Proteins
227 were labeled with either SIL or iTRAQ subjected to LC-MS/MS. Both proteomes were combined,
228 redundancies removed and confidently identified peptides with abundance changes of 2-fold or
229 greater linked to protein identifiers. The lists of upregulated and downregulated proteins were
230 submitted to the Database for Annotation, Visualization, and Integrated Discovery (DAVID) v6.7
231 and mapped to KEGG pathways. Significantly enriched major metabolic pathways were listed
232 with proteins, soluble (Sol) or insoluble (Insol) fraction and fold change (FC) designated.

233 **DC restructure metabolism during IAV infection**

234 Next, we sought to determine whether the changes in metabolic protein networks in our
235 proteomic analysis were reflected in DC metabolism. To validate the protein network analysis and
236 further characterize influenza-induced changes in metabolism, we quantified glucose, pyruvate,
237 glutamine, and palmitic acid oxidation as previously described [14]. Isotopically labeled metabolic
238 substrates were used to monitor generation of $^{3}H_2O$ from glycolysis or beta oxidation and $^{14}CO_2$
239 from the pentose phosphate pathway, glutamine utilization, or TCA cycle. Glucose detritiation
240 occurs early in glycolysis when fructose-6-phosphate is converted to fructose-1,6-bisphosphate.
241 By monitoring glucose detritiation, we found that influenza infection significantly increased
242 glycolysis (Fig 2A). PPP provides ribose 5-phosphate for nucleotide synthesis and NADPH as a
243 cofactor for fatty acid synthesis. We quantified the oxidative portion of this pathway, following the
244 release of CO_2 from glucose-6-phosphate, and found the pentose phosphate pathway was
245 unchanged by IAV infection (Fig 2B).

246 Glycolysis is linked to the TCA cycle by the conversion of pyruvate to acetyl-CoA and CO_2
247 by the pyruvate dehydrogenase complex. To assess TCA cycle, we quantified the aggregate
248 release of $^{14}CO_2$ from [2-^{14}C]-pyruvate in 3 steps of the cycle. Consistent with the enrichment of
249 this pathway in the decreased proteome, we found TCA cycle was significantly reduced following
250 influenza infection of DC (Fig 2C). Based on the network and flux analyses, we further examined
251 the pyruvate dehydrogenase complex. This is a large multifaceted protein complex. It was
252 completely covered in the proteome, and most pyruvate dehydrogenase subunits decreased after

253 infection (Table 3). In the canonical TCA cycle, in addition to pyruvate-derived acetyl-CoA,
254 oxidation of fatty acids or glutamine can be used to produce ATP and intermediates. Glutamine
255 is also a substrate for reductive carboxylation in the non-canonical reversal of the cycle. When
256 we measured the release of isotopically labeled glutamine, we found DC increased glutaminolysis
257 during IAV infection (Fig 2D). However, palmitic acid oxidation was unchanged in IAV infected DC
258 concomitant to a decrease in intracellular free fatty acids (Fig 2E & F). Together, the increase in
259 glycolysis and decrease in TCA cycle utilization of pyruvate is reminiscent of the Warburg effect
260 that occurs in some cancers, in which the two major metabolic pathways become uncoupled to
261 maintain ATP production while increasing metabolic plasticity [31-36].

262 **Table 3. Proteomic coverage of the pyruvate dehydrogenase complex**

Subunit Function	Fold Change	Subunit Name	Fraction
E1 Regulatory (Activator)	-2	Pyruvate dehydrogenase kinase 1	Insol
E1 Regulatory (Activator)	-2	Pyruvate dehydrogenase kinase 3	Insol
E1 Catalytic	-1	Pyruvate dehydrogenase beta	Sol
E1 Catalytic	-1	Pyruvate dehydrogenase alpha	Sol
E1 Catalytic	-2	Pyruvate dehydrogenase beta	Insol
E1 Catalytic	-2	Pyruvate dehydrogenase alpha	Insol
E3 Non-catalytic	-2	Pyruvate dehydrogenase component X	Insol
E2 Catalytic	1	Dihydrolipoamide S-acetyltransferase	Insol
E2 Catalytic	-2	Dihydrolipoamide S-acetyltransferase	Sol
E3 Catalytic	1	Dihydrolipoamide dehydrogenase	Sol
E3 Catalytic	-2	Dihydrolipoamide dehydrogenase	Insol
E1 Regulatory (Inhibitor)	-2	Pyruvate dehydrogenase phosphatase	Insol

263 **Table 3. Abundance change in pyruvate dehydrogenase complex subunits from proteome.**
264 The proteome was queried for components of the pyruvate dehydrogenase complex and subunits
265 reported with corresponding functions, fold changes, names, and localization to soluble (Sol) or
266 Insoluble (Insol). Summary of identified metabolic proteins that relocalized from soluble to
267 insoluble fraction or vice versa. Fold enrichment significance was generated from DAVID
268 functional annotation clustering and the biological significance indicated with p-value derived from
269 KEGG pathways. Fold changes from non-unique proteins identified in the same metabolic
270 pathway were averaged.
271
272 Some cancers and T cells display dynamic metabolism by acquiring more flexibility in
273 metabolic substrate oxidation to facilitate macromolecule synthesis and ATP production [14, 15,
274 28, 37-42]. To determine the contribution of pyruvate, palmitic acid, and glutamate to DC
275 bioenergetics, we monitored oxygen consumption via mitochondrial respiration using the XF Mito
276 Fuel Flex Test as previously described [1, 43, 44]. This test was run on an XF Extracellular Flux

277 Analyzer (Xfe96) that kinetically measures oxygen consumption rates (OCR) to monitor
278 mitochondrial respiration over time while injecting stimulants or inhibitors. Xfe96 respirometry, in
279 the context of inhibitor treatments, allowed us to probe DC energy utilization, substrate
280 preference, and metabolic plasticity by selectively blocking mitochondrial oxidation of pyruvate,
281 palmitic acid, or glutamate with UK5099, etomoxir, or BPTES, respectively. Note that while
282 etomoxir can have off-target metabolic effects at high concentrations[45], it is a specific inhibitor
283 of fatty acid oxidation in this context. Thus, the capacity of DC for oxidizing an isolated substrate
284 was determined by quantifying the OCR after blocking the other two substrates, and, conversely,
285 dependency on a single substrate was determined by inhibiting its oxidation (S2A-C Fig). We then
286 combined the percent oxidation capacity or dependence and compared the infected and
287 uninfected DC (Fig 2G & H). DC adopted a slight increase in capacity for oxidation of glucose,
288 glutamine, and fatty acids to fuel mitochondrial respiration following infection (Fig 2G). However,
289 IAV infection did not significantly alter DC dependence on mitochondrial oxidation of these
290 substrates (Fig 2H). Together, capacity and dependency determine the flexibility of mitochondrial
291 substrate oxidation (i.e. flexibility is the difference between the capacity to use a substrate and
292 the dependency on that substrate). Overall, the mitochondrial flexibility for diverse metabolic
293 substrates in DC was increased after IAV infection (Fig 2I).

294 Previously, we showed that neither the dependence nor capacity for oxidizing these
295 mitochondrial substrates was dramatically impacted by IAV infection of epithelial cells, even
296 though the trend for glutamine dependence increased [1]. However, when we calculated the
297 individual contribution by substrate, we found quiescent DC had a significantly lower capacity and
298 dependence on glutamine than on pyruvate and fatty acid oxidation (S2D Fig open bars). Yet, in
299 response to IAV infection, DC significantly increased their capacity to use glutamate to fuel
300 mitochondrial respiration (S2D Fig). When we blocked pyruvate entrance into the TCA cycle or
301 fatty acid import for β-Oxidation, we found a significant reduction in intracellular glutamine in IAV

302 infected DC, presumably due to increased glutaminolysis in the absence of other oxidative
303 substrates (S2E Fig). Next we wanted to determine if IAV infected DC would increase glutamate
304 dehydrogenase enzyme activity to drive glutaminolysis in the absence of the other mitochondrial
305 oxidative substrates. α-ketoglutarate enzyme activity significantly increased when we blocked
306 pyruvate with UK5099 in IAV infected DC (S2F Fig). Taken together**,** these data reveal that IAV-
307 infected DC significantly increase glycolysis without increased shuttling of acetyl CoA from
308 pyruvate into the TCA cycle, while also improving their capacity and flexibility for mitochondrial
309 substrate oxidation, including markedly increasing glutaminolysis.

310 **IAV infected DC increase glycolytic bioenergetics similar to TLR stimulation**

311 Substrate consumption for ATP production and product efflux vary with cellular
312 metabolism and can be used to measure bioenergetic states. Thus, we also used the Xfe96 to
313 determine the extracellular acidification rate (ECAR) as an indirect measure of glycolysis. Indeed,
314 lactic acid excretion per unit time in glycolysis accounts for the majority of pH change in most cell
315 types and glycolysis correlates well with extracellular lactic acid accumulation (i.e. R^2 = 0.9101)
316 [46, 47]. However, phagocytes employ radical generation and pH in signaling and innate effector
317 functions, and therefore we used the glycolytic stress test to isolate glycolytic ECAR from lactate
318 and non-glycolytic ECAR as previously described [47-49]. In keeping with our flux analysis, we
319 found that influenza infected DC significantly increased glycolysis resulting in a mean difference
320 of 26.5242 95% CI [1.62, 51.43] (Fig 3A). While previous reports indicated detritiation of D-[3-^{3}H]-
321 glucose underestimates glycolysis [50], we found the IAV-induced increases in glycolytic flux and
322 bioenergetic measures of glycolysis were comparable (Figs 2A and 3A). We also infected DC with
323 the 2009 pandemic H1N1 influenza A/California/04/2009 (CA04) and the H3N2 subtype influenza
324 reassortment virus X31 that carries the HA and NA genes of A/Hong Kong/1/1968 in the
325 background of PR8. Similar to the PR8 (Fig 2A-IAV), we found CA04 infected DC significantly

326 increased glycolysis, resulting in a mean difference of 17.60 95% CI [6.017, 29.18] while the
327 increase by X31 was not significant (S4A Fig).

328 We then sought to distinguish between cell-mediated responses to viral entry and innate
329 recognition and to determine if DC restructure glycolysis equally with activating stimuli or tailor it
330 in response to IAV infection. To this end, we treated DC with different TLR agonists and β-
331 propiolactone (BPL) inactivated IAV (IAV^{BPL}) and compared these responses to active IAV.
332 Influenza infects and replicates its genome producing viral proteins within DC, but virions are not
333 released [21, 22]. In contrast, BPL treatment prevents genome replication but allows IAV to attach,
334 fuse, and stimulate TLR7 in the endolysosome [51-53]. We used the TLR3 agonist polyinosinic
335 polycytidylic acid (structurally similar to IAV dsRNA), TLR4 agonist lipopolysaccharide (LPS) to
336 simulate DC detection of IAV-infected dead cells, and imidazoquinoline R848 (R848) for activation
337 of both TLR7 and 8 and its adapter MyD88. Like IAV, these treatments significantly increased
338 glycolysis (Fig 3A). ATP synthase inhibition with oligomycin decreases the ATP/ADP ratio thereby
339 increasing glycolysis to maximal output, allowing us to calculate the glycolytic capacity of DC (i.e.
340 maximal ECAR post oligomycin less non-glycolytic acidification). The glycolytic capacity was also
341 increased by IAV infection, PolyIC, and R848, but not LPS (Fig 3A). The difference between the
342 maximal glycolytic output and basal glycolysis is the glycolytic reserve, which remained constant
343 across treatments (Fig 3A). The final injection of 2-DG allowed us to quantify any extracellular
344 acidification occurring independent of glycolysis. We found that non-glycolytic acidification was
345 significantly increased by active influenza infection and LPS treatment resulting in a mean
346 difference from control of 13.16 and 23.29 respectively (Fig 3A and S3A Fig). We then quantified
347 glucose uptake to determine if substrate import was coordinated with the increase in glycolysis.
348 We found, in comparison to control, IAV and LPS significantly increased glucose uptake resulting
349 in similar mean differences (Fig 3B and S3B Fig). Interestingly, glucose uptake in DC infected
350 with active IAV was significantly higher than inactivate IAV^{BPL} (S3B Fig**)**. Thus, in response to IAV

351 infection DC increased both glucose uptake and glycolysis. However, in general these activators
352 stimulated an uptick in glycolysis, which may provide additional energy and glucose-derived
353 metabolic intermediates for macromolecule biosynthesis as both are necessary to fuel effector
354 functions such as increased motility, phagocytosis, and cytokine production.

355 **IAV infected DC mitochondrial respiration is distinct from TLR stimulation**

356 Next, we used respirometry with the Xfe96 to quantify and isolate individual components
357 that contribute to mitochondrial respiration with the mitochondria stress test as previously
358 described [54, 55]. This test is based on the principle that the amount of oxygen consumed during
359 respiration is stoichiometrically related to the amount of ADP and substrate in respiratory
360 oxidation. It probes respiration efficiency using sequential inhibition of complex V (ATP synthase)
361 and complexes I and III of the electron transport chain with oligomycin and a mixture of rotenone
362 and antimycin A, respectively, and the uncoupler FCCP to activate proton conductance. Using an
363 analysis of variance (ANOVA) on all the treatments yielded significant variation among conditions
364 ($p < .0001$) and with a post hoc Tukey's Honest Significant Difference test we showed that control
365 untreated and IAV infected DC differed significantly at $p < .0001$ (Fig 3C). Only IAV increased
366 respiration, resulting in a mean difference of 22.51 pmol/min/RFU with a 95% CI [3.48, 41.54]
367 between IAV and control (S3C Fig). Conversely, PolyIC, LPS, and R848, all reduced basal
368 respiration by mean differences of 2.3, 7.6, and 12.4 pmol/min/RFU, respectively, but only the
369 R848 group difference was significant (Fig 3C). Accordingly, we also showed IAV differed
370 significantly from PolyIC, R848, and LPS at $p \leq 0.0033$ (S3C Fig). Similarly, we found modest but
371 reliable increases in respiration when DC were infected with either the CA04 or X31 that are H1N1
372 and the H3N2 subtypes, respectively (S4B Fig). Therefore, in response to IAV infection, DC
373 significantly increase basal respiration and this response is significantly different from PolyIC,
374 LPS, or R848 treatment.

375 After three basal respiratory measures were taken the ATP synthase inhibitor oligomycin
376 was added to isolate OCR linked to ATP production. IAV infection induced a modest increase in
377 oxygen consumption linked to ATP synthase activity in DC, whereas LPS and R848 treatments
378 significantly reduced respiratory ATP production (Fig 3C). Like basal respiration, these opposing
379 responses resulted in significant differences in respiratory ATP production between the IAV
380 infected and PolyIC, LPS, or R848 treated DC (S3C Fig). To maximize respiratory OCR, we then
381 uncoupled oxygen consumption from ATP production with the addition of the protonophore FCCP.
382 This allowed us to calculate the maximal oxygen consumption of DC for respiration, which was
383 significantly impaired by LPS or R848 treatment but unperturbed by IAV infection (Fig 3C). These
384 three measures demonstrate that IAV infected DC increase basal oxygen consumption that is
385 associated with mitochondrial respiration whereas in response to R848 and LPS treatments both
386 ATP production and maximal respiration are impaired.

387 The difference between maximal and basal respiration, or the spare respiratory capacity,
388 indicates how closely cells are operating near their OXPHOS threshold. Untreated and PolyIC
389 treated DC displayed similarly low basal and high maximal respiration, resulting in similar spare
390 respiratory capacity (Fig 3C). In contrast, DC treated with either R848 or LPS failed to respond to
391 FCCP resulting in very low maximal respiration and spare respiratory capacity (Fig 3C and S3C
392 Fig). By comparison, IAV infected DC increased OCR when FCCP activated proton conductance
393 but had no change in maximal respiration (Fig 3C top). This was due to the significantly higher
394 basal rate, near DC maximal respiration, thereby reducing spare respiratory capacity of IAV
395 infected DC. Indeed, the mean difference in IAV infected DC and untreated controls spare
396 respiratory capacity is -40.62 with 95% CI [-69.16, 12.09], a significant difference $P < 0.0001$ (Fig
397 3C and S3C Fig). Therefore, IAV, LPS, and R848 treated DC had significantly reduced spare
398 respiratory capacity, but different respiratory responses. Thus, due to IAV inducing an uptick in
399 basal respiration the infected DC were already operating closer to their maximal respiratory output

400 thereby diminishing their capacity to increase respiration, whereas LPS stimulated DC had a well-
401 documented respiratory collapse and did not respond to uncoupling [18, 19].

402 The final inhibitor combination of rotenone and antimycin A blocks proton transport in the
403 electron transport chain by inhibiting complex I and III for the quantification of proton leak and
404 residual OCR from other sources (e.g. NADPH oxidases, arachidonic acid metabolism, NOX
405 enzymes, etc.). OXPHOS proton leak is the respiratory OCR that is not coupled to respiratory
406 ATP production and, under these conditions, it is unresponsive to fluctuations in substrate
407 oxidation and unaffected by variations in ATP turnover [56]. IAV infection and LPS treatment
408 showed significantly more proton leak than controls (Fig 3C). Mitochondrial coupling efficiency is
409 the amount of ATP produced through the electron transport chain per reduction of consumed
410 oxygen, it is similar to the traditional phosphate oxygen ratio and both are sensitive to
411 mitochondrial dysfunction [56]. Proton leak does respond to respiratory dysfunction from
412 uncoupling and can indicate severe mitochondrial damage [56]. However, we found that the
413 respiratory coupling efficiency of DC was stable for IAV, IAV^{BPL}, and PolyIC as opposed to LPS
414 and R848 treatments that were significantly reduced (Fig 3C). Taken together, the impaired
415 FCCP response of both LPS and R848 and diminished coupling efficiency indicate mitochondrial
416 damage, which is in keeping with current reports on the impact of LPS on DC respiration [18, 19].

417 We also found that the non-mitochondrial respiration oxygen consumption rates were
418 significantly increased by active IAV influenza infection, R848, and LPS treatment (Fig 3C). This
419 was not surprising, given that activated phagocytes produce reactive oxygen species (ROS) from
420 inflammatory enzymes cyclooxygenases, lipooxygenases and NADPH oxidases, NADPH
421 oxidases alone can account for up to 90% of total cellular oxygen consumption in these cells [57].
422 ROS damages mitochondria and varies with non-mitochondrial respiration OCR [58]. Thus it is
423 possible that R848 and LPS over activate proinflammatory enzymes that divert oxygen away from
424 respiration creating a significant increase in non-mitochondrial OCR concomitant to reducing OCR

425 in basal respiration lowering ATP production and potentially damaging mitochondria as is evident
426 by the lack of FCCP response creating significant drops in maximal and spare respiration along
427 with decreased coupling efficiency, as well as proton leak for LPS (Fig 3C). Non-mitochondrial
428 OCR rose 175% in DC with LPS treatment and was significantly higher than all other treatment
429 groups (Fig 3C and S3C Fig). Combined, these measures provide an indication of the
430 bioenergetic state of activated DC. Impairment of the electron transport chain will lower coupling
431 efficiency, mitochondrial ATP production, and spare respiratory capacity while increasing proton
432 leak. However, cells can still meet their metabolic demands with proton leak and in the presence
433 of heightened basal respiration that lessens the dynamic range and prevents dramatic bursts in
434 respiration [58].

435 In lieu of mitochondrial impairment, these measures of pyruvate flux, glutamine flux, and
436 respirometry showed that influenza infection significantly reduced normal pyruvate oxidation while
437 increasing glutamine oxidation for fueling the TCA cycle. This makes sense given 17 hours after
438 IAV infection DC had significantly depleted glucose in their surrounds (i.e. a mean difference of -
439 6.680 mg/dl glucose with 95% CI [-12.24, -1.115]) (Fig 3B). Further, when glucoses derived
440 pyruvate is lacking DC are known to shift to glutaminolysis to fuel TCA cycle to support OXPHOS
441 [19, 58-62]. Thus, even though we find IAV infection results in significant increases in DC
442 glycolysis it appears to uncouple from the TCA cycle, via reduced pyruvate dehydrogenase,
443 concomitant to a modest increase in glutaminolysis acting to fuel OXPHOS related oxygen
444 consumption without evidence of mitochondrial damage as measured by FCCP response and
445 coupling efficiency.

446 **IAV infection DC increase ATP production via glycolysis distinct from TLR agonists**

447 Normally, the majority of cellular ATP is derived from OXPHOS downstream of glycolysis
448 and the TCA cycle. However, glucose import, oxidation, and basal glycolysis significantly
449 increased after infection of DC, concomitant to declining pyruvate oxidation while respiration and

450 respiratory capacity and flexibility increased (Figs 2 and 3). Collectively these findings support a
451 transition of DC metabolism to more aerobic glycolysis and non-canonical TCA, reducing the
452 efficiency of ATP production per oxidized substrate. To determine the source of ATP production
453 in IAV infected DC, we measured total ATP production rates and that derived from glycolysis or
454 mitochondrial OXPHOS. Changes in the relative output of ATP from glycolysis and mitochondrial
455 respiration often reflects the cell's metabolic phenotype. Consistent with our previous bioenergetic
456 measures of glycolysis and respiration, we found that DC paired into three distinct metabolic
457 phenotypes: hyper metabolic IAV and IAV^{BPL} (black and gray), metabolically impaired R848 and
458 LPS (yellow and blue), and normal Ctl and PolyIC (open circle and green) (Fig 3D top). DC
459 significantly increased total ATP production in response to IAV infection, irrespective of BPL
460 inactivation, (Fig 3D). Indeed, following IAV infection DC had a striking 39% increase in glycolytic
461 ATP production resulting in a mean difference of 418.6 pmol/min/RFU with 95% CI [297.1, 540.1]
462 when compared to controls (Fig 3D & S3D Fig). In contrast, IAV infection diminished mitochondrial
463 ATP while R848 or LPS treatment significantly reduced it (Fig 3D & S3D Fig). One hallmark
464 indicator of a fundamental shift in metabolic phenotype is a change in the ATP ratio from
465 mitochondrial to glycolytic ATP production. Due to the dramatic and very significant increase in
466 glycolytic ATP production concomitant to modest changes in mitochondrial ATP production
467 following infection, the ATP rate index significantly decreased DC following infection (Fig 3D
468 bottom). This indicates DC change to a more glycolytic and less oxidative phenotype following
469 IAV infection. In contrast, DC activated with either LPS or R848 also exhibit a significant decrease
470 in the ATP rate index, but this was due to a very significant reduction in mitochondrial ATP
471 production without a change in glycolytic ATP (Fig 3A & D). Collectively these metabolic and
472 bioenergetic studies reveal that DC re-wire their metabolism in response to IAV infection in a
473 manner that resembles Warburg metabolism in cancer and is distinct from TLR4 and TLR7/8
474 agonist treatment.

475 **Transcriptional regulation of DC metabolic phenotype**

476 One transcription factor promoting the highly glycolytic and glutaminolytic metabolic
477 transition in cancer and activate T lymphocytes is c-MYC [14, 63-67]. DC express variable levels
478 of three Myc family members (c-MYC, n-MYC, and l-MYC) that regulate immune cell
479 development, differentiation, and activation [14, 68, 69]. We found IAV infection induced transient
480 c-MYC expression peaking at 4 hours (Fig 4A). This increase in c-MYC expression in IAV-infected
481 DC was reflected in increased protein levels by 17 hours (Fig 4A inset). In many cancers, some
482 c-Myc driven, this metabolic phenotype is also associated with sensitivity to glucose and
483 glutamine deprivation that results in rapid cell death if these metabolites are restricted and is often
484 referred to as glucose and glutamine addiction [63, 65-67, 70-72]. We previously found c-Myc
485 transiently increased in IAV infected epithelial cells and glucose and glutamine restriction caused
486 an approximate 50% decrease in their viability [1]. Therefore, we quantified DC viability and cell
487 death using CalcienAM and ethidium bromide homodimer (EthD-1) per total cell content via DAPI.
488 Cell death was minimal, impacting less than 10% of DC, irrespective of metabolite restriction or
489 treatment (S4C Fig). In the absence of glucose, the proportion of viable DC dropped (S4C Fig
490 open bars). However, neither infection nor activation with TLR agonists increased cell death (i.e.
491 reduce the live to dead ratio) in the absence of glucose (S4C Fig). The same was true when
492 glutamine was restricted apart from R848 and LPS, these treatments significantly reduced cell
493 death thereby increasing the live to dead ratio (S4C Fig). In contrast to epithelial cells, removal of
494 both glutamine and glucose had no adverse effect on IAV-infected DC (S4C Fig open and solid
495 bars). LPS was the only treatment to slightly increase DC cell death, from 6.4% or 7.1% for the
496 complete or deplete controls, to 9.8% for DC treated with LPS in the absence of both glutamine
497 and glucose (S4C Fig red vertical stripes). We observed high levels of viability with very little cell
498 death in all treatments, indicating that metabolic differences were not simply due to population
499 decline or adverse effects from treatment with high concentrations of agonists. Further, the

500 viability of infected DC was more stable with varying metabolite levels than we previously
501 observed in IAV-infected respiratory epithelial cells [1]. These findings were surprising, given the
502 transient in c-Myc (Fig4A), but were in keeping with DC not developing substrate dependency
503 (Fig 2H) and likely due to the significant increase in metabolic flexibility and capacity to utilize
504 diverse substrates that DC acquire with infection (Fig 2G & I).

505 To determine if DC require c-MYC activity to modulate their metabolic response to
506 infection, we pretreated DC with a c-MYC inhibitor (MI) also known as 10058-F4, for 4 hours, then
507 infected them and measured glycolysis and non-glycolytic acidification. After infection DC
508 increased glycolysis by 54.3%, but c-MYC inhibition caused this to drop significantly to 10.2%
509 similar to uninfected levels (Fig 4B). MI treatment also reduced non-glycolytic acidification
510 following IAV infection (Fig 4C). Increases in c-MYC primarily boost metabolism through the
511 glycolytic pathway by increasing levels of lactate dehydrogenase A, glucose transporter 1,
512 phosphoglucose isomerase, phosphofructokinase, glyceraldehyde-3-phosphate dehydrogenase,
513 phosphoglycerate kinase, and enolase [73-75]. We found many of these proteins increased in the
514 proteome, including α-enolase (S1 A&D Fig). However more recent studies have implicated c-
515 MYC in regulating mitochondrial metabolism and biogenesis as well [67, 76-78]. To determine if
516 c-MYC was regulating the modest IAV induced changes in respiration we quantified basal
517 respiration and non-mitochondrial oxygen consumption and found MI treatment had less effect
518 (Fig 4D-E). Thus, in response to IAV infection, DC increased c-MYC expression and glycolysis
519 and inhibiting c-MYC activity blocked the IAV induced glycolytic increase.

520 **Metabolic rewiring in IAV infection is necessary for DC effector functions**

521 DC are controllers of innate and adaptive immunity and they are the primary immune cell
522 population responsible for inducing the IAV virus specific CD8 T cell response requisite for viral
523 elimination. Thus DC migration from the lungs to the lymph nodes is a critical first step in bridging
524 the innate and adaptive response to IAV [5]. Increases in DC trafficking occur quickly after IAV

525 infection and peak *in vivo* around 18 hours [79, 80]. We used a fluorescent cell migration assay
526 to quantify DC motility in response to IAV infection. We found a very significant increase in DC
527 migration after IAV infection (Fig 5A black). Myc inhibition had no effect on the migration of
528 uninfected DC, while completely ablating IAV-infected DC migration (Fig 5A orange). Similarly,
529 inhibiting the oxidation of pyruvate via the TCA cycle with UK5099 had no impact on the migration
530 of uninfected DC (open bars), but significantly reduced infected DC migration by approximately
531 30% (Fig 5A red). Nonetheless, this migration was significantly higher than the controls (Fig 5A).
532 Inhibiting fatty acid or glutamine oxidation in the mitochondria resulted in the same changes in
533 DC migration as inhibiting pyruvate, primarily a significant decline in infected DC mobility that
534 remained much higher than uninfected controls (Fig 5A blue and green). We then sought to
535 determine if phagocytic activity of infected DC could be modulated by targeting these same
536 pathways and found no effect (S5B Fig). While the role for DC phagocytosis post infection is
537 unclear, and likely minimal we also found no differences among uninfected drug treated controls
538 (S5B Fig open bars). Thus, inhibiting c-MYC ablates IAV-induced DC migration while blocking
539 mitochondrial oxidation of pyruvate, glutamine, or fatty acids, significantly impairs it.

540 Initial studies of DC function *in vitro* revealed that IAV can infect and stimulate DC
541 maturation into potent antigen presenting cells that elicit robust IAV-specific T cell response
542 relative to other APC without the addition of exogenous cytokines [81-83]. To delineate the roles
543 of c-MYC, glycolysis, and mitochondrial substrate oxidation in DC maturation, we inhibited each
544 and then infected the DC with IAV for 17 hours. The DC were then transferred to plates of freshly
545 purified, wild type CD8 and CD4 T cells from naïve or homologously primed C57BL/6 mice at a
546 ratio of 1 to 5 and co-cultured for 24 or 48 hours. It is well documented that T cells rapidly respond
547 to activation with an immediate and robust glycolytic switch that increases ECAR and can be
548 monitored to determine their activation state and distinguish T cell responses after anti-CD3/CD28
549 beads stimulation [14, 84-88]. Indeed, using this T cell activation assay as previously described

550 [85-88], we found primary splenic T cells rapidly responded to anti-CD3/CD28 bead stimulation
551 with clear and measurable increases in ECAR (Fig 5B). Furthermore, this ECAR peak was
552 significantly increased when these T cells were co-cultured with IAV-infected DC as compared to
553 uninfected controls (Fig 5B). Irrespective of inhibition of glycolysis or glutaminolysis with prior
554 treatment of DC with c-MYC inhibitor or BPTES respectively, IAV infected DC effectively primed
555 T cells resulting in a significant increase in T cell activation with bead stimulation (Fig 5C orange
556 and green). In contrast, inhibition of pyruvate or fatty acid oxidation prevented effective IAV
557 induced DC priming of T cells resulting in activation peaks that were the same as uninfected
558 controls (Fig 5 C red and blue).

559 Following DC-T cell co-culture, we assessed CD8+ T cell populations staining positive for
560 CD8, CD25 and CD44 with flow cytometry (S5C Fig). Only etomoxir treatment reduced CD8+ T
561 cells (S5D Fig). DC that were pretreated with metabolic inhibitors reduced the CD25+ T cell
562 population following co-culture (S5E Fig). However, due to the response heterogeneity of the T
563 cell population from naive mice we move to a transgenic system. We purified CD8+ T cells from
564 spleens of C57BL/6-Tg (TcraTcrb)1100Mjb/J (OT1) mice that contain transgenic inserts for Tcra-
565 V2 and Tcrb-V5 genes. OT1 T cell receptor interacts with the ovalbumin amino acid sequence
566 SIINFEKL, corresponding to residues 257-264, in the context of H2Kb. Dendritic cells were then
567 vehicle or drug treated and infected for 17 hours with a PR8 influenza virus reverse engineered
568 to express the SIINFEKL OVA peptide in the neuraminidase stalk (IAV^{OVA}) that was generously
569 provided by Dr Richard Webby as previously described [89]. We used three controls: T cells
570 without DC (-DC), T cells co-cultured with uninfected and untreated control DC (Ctl), and T cells
571 co-cultured with untreated DC infected with IAV^{OVA}. We found DC infection with IAV^{OVA}
572 significantly increased the population of CD8+ T cell irrespective of drug treatment (Fig 5D and
573 S5E Fig). We used cell surface staining and flow cytometry to quantify to CD25+ and CD44+
574 populations of CD8 T cells. In keeping with our previous results, we found that modulation of DC

575 metabolism can significantly reduce the population of CD8+ T cells expressing the early activation
576 marker CD25 compared to IAV^{OVA} alone (Fig 5E and S5F Fig). However, in the transgenic OT1
577 system IAV^{OVA} infection induced a significant rise in the proportion of T cells expressing CD25
578 irrespective of drug treatment (Fig 5E and S5F Fig). Similarly, metabolic inhibition of DC was not
579 strong enough to abolish the significant increase in expression of CD44 on OT1 T cells in
580 response to co-culture with IAV^{OVA} infected DC (Fig 5F). Importantly, in each of the 3 separate
581 experiments DC treated with Myc inhibitor, etomoxir or BEZ235 significantly lower the population
582 of CD44+ relative to IAV (Fig 5F and S5D&E). Based on our previous studies in IAV infected
583 epithelial cells and DC, we knew the PI3K/mTOR inhibitor BEZ235 would block the IAV induced
584 increase in glycolysis (1). Thus, we wanted to compare T cell response to DC treated with these
585 inhibitors and found that BEZ235 significantly reduced the CD25 or CD8 positive T cells similar
586 to Myc inhibitor (Fig 5E&F orange and yellow). Collectively these data show specific metabolic
587 pathways are critical to DC functions such as motility and T cell activation. Namely, limiting
588 glycolysis ablated IAV induced DC migration, a critical step for DC to get to the lymph nodes to
589 initiate the adaptive response, and reduces CD25/CD44 positive CD8 T cell populations. In
590 contrast, access to diverse fuels for mitochondrial respiration appears to have less effect on
591 migration but play an more important role in rapid T cell activation and induction of the CD25
592 positive CD8 population.

593 **Lung TipDC globally reprogram metabolism in response to IAV infection *in vivo***

594 We have speculated that glycolysis and specific mitochondrial substrates that fuel
595 OXPHOS are critical for DC migration and T cell priming *in situ* based on our *in vitro* models, and
596 asserted the former is particular likely to affect immune response during influenza infection given
597 DC translocation is a major determinant of outcome [79, 80, 90]. To determine if these metabolic
598 pathways were relevant *in vivo* we intranasally infected C57BL/6 mice with IAV or mock for 9 days
599 and removed the lungs. We isolated immune cells from the lungs and sorted DC based on

600 CD11b^{hi}, Ly6c/GR-1^{hi}, MHCII ^{hi} DC surface marker staining (TipDC). TipDC are known for being
601 inflammatory and producing TNF-α and inducible nitric oxide synthase. In previous studies we
602 showed this DC subset presents antigen to CD8 T cells in the lungs of mice infected with influenza
603 A viruses and found TipDC are required to produce adequate influenza-specific CD8+ T cell
604 proliferation in the infected lung to mediate viral clearance [91]. We purified RNA from the TipDC,
605 generated cDNA libraries and subjected them to sequencing using the HiSeq2000 system
606 (Illumina, San Diego CA) as previously described [92]. The paired end RNA-Seq data was
607 aligned, concordant pairs were kept (MAPQ>10), a read number assigned to each gene (45,142
608 reads) and all genes with less than 3 counts or FDR > 0.05 were excluded. Thus, after
609 redundancies were aggregated by mean, there were 13,285 confidently identified transcripts
610 (Table A in S2 File). To evaluate the group trends, sample uniformity and identify potential outliers
611 unsupervised multivariant principal component analysis (PCA) was employed. F1 and F2
612 explained the total variance with a cumulative percent variability of 91.35% (S6A Fig). We find the
613 IAV has similar component 1 values and the controls have similar component 1 values, indicating
614 the samples within each group have similar gene expression levels (S6A Fig). The double filtered
615 volcano plot in Supplemental Figure 6B describes the selection criterion with the statistical effects
616 on the y-axis and biological effects on the x-axis (dotted lines mark fold change ≥ |2.7| on the x
617 axis and p-value ≤ 0.001on the y axis).

618 These data were then independently k-means clustered followed by ascendant
619 hierarchical clustering based on Euclidian distances. Genes with very little variability were non-
620 specifically filtered using a standard deviation threshold of 50% to simplify the graph. The data
621 matrix was rearranged according to the corresponding clustering with similarity proportional to a
622 closer spatial relationship for DC columns and transcript rows. These clustering results were also
623 represented via a dendrogram displayed vertically for genes and horizontally for TipDC. This
624 resulted in clean separation of the TipDC from day 0 and the TipDC from day 9 of the IAV infection

625 (Fig 6A). The data values of the permuted matrix were replaced by corresponding color intensities
626 based on interquartile range with color scale of blue to red through white resulting in a heat map
627 that vividly demonstrates the difference in gene expression of these infected and uninfected
628 TipDC (Fig 6A).

629 We then used the OMICS data analytics package (Addinsoft, New York) to identify gene
630 transcripts that were significantly affected by IAV infection in the context of specific criteria. We
631 used the Differential Expression Analysis tool to apply a non-specific filtering threshold of 50%
632 based on standard deviation and identifying significant differences in expression based on p-
633 values generated from a parametric comparison of differences (Tukey honest significant
634 difference test for multiple comparisons) with a post-hoc false discover rate correction (Benjamini-
635 Hochberg). When compared to day 0 uninfected controls (Ctl), we found 4,788 transcripts were
636 significantly altered on day 9 of IAV infection (Table B in S2 File). Gene identifiers of transcripts
637 that increased with infection were input to DAVID for KEGG pathway enrichment analysis. Fifty
638 pathways were significantly enriched, many of these were expected for TipDC in the IAV infected
639 lung such as those governing immune response (e.g. Lysosome, Toll-like receptor signaling
640 pathway, phagosome, TNF signaling pathway, endocytosis, Fc gamma R-mediated
641 phagocytosis, etc.) as well as Influenza A (Table C in S File). Of the 50, global Metabolic Pathways
642 (mmu01100) was the second most significantly enriched (Table C in S2 File). Like the *in vitro*
643 differentiated DC proteome, we found pathways within the Metabolism KEGG Class comprise a
644 large proportion of the increased TipDC transcriptome (Fig 6B). However, for the TipDC the
645 Human Disease class was larger (Fig 6B). This is not surprising, given it includes infectious
646 disease and cancer accounting for 8 and 6 out of 17 pathways, respectively. We then input the
647 genes from the 11 significantly enriched metabolic pathways into DAVID to identify the diversity
648 of the metabolic pathways associated with these transcripts that were significantly increased
649 following IAV infection (Table D in S2 File). Glycolysis, oxidative phosphorylation, purine

650 metabolism, and amino acid metabolism are some of the pathways these proteins regulate. Figure
651 6D depicts the enzymes and products of glycolysis with the transcripts that were significantly
652 altered by IAV infection, we see expression of the majority of these key enzymes was upregulated.
653 Thus, among TipDC transcripts that significantly increased nine days following IAV infection we
654 find eleven metabolic pathways were significantly enriched, including the global Metabolic
655 pathway ($p < 0.00001$) and glycolytic enzymes were significantly enriched ($p < 0.00001$).

656 In contrast, metabolism only made up 3% of the KEGG Classes and the global Metabolic
657 pathways (KEGG ID mmu01100) was not found in the enrichment analysis of the TipDC
658 transcripts that decreased following IAV infection (Fig 6C and Table E in S2 File). However, we
659 did find two pathways associated with metabolism in the decreased transcriptome (Purine
660 metabolism and Metabolism of xenobiotics by cytochrome P450). Many pathways enriched in the
661 down regulated transcriptome reflect pathways one would anticipate being suppressed in TipDC
662 on day 9 of the infection (e.g. leukocyte transendothelial migration, extra cellular matrix (ECM)-
663 receptor interactions, cell adhesion molecules (CAMs), focal adhesions, etc.). We were surprised
664 to see Influenza A pathway enriched in the transcripts that decreased with IAV. On closer analysis
665 we found it was differentially regulated, as was Cytokine-cytokine receptor interaction, and Fc
666 gamma R-mediated phagocytosis (Table F in S2 File). These include increased expression of
667 viral sensors TLR4, TLR3, IFNAR1, IFNAR2 and related signaling molecules such as MyD88,
668 STAT1, and STAT2 concomitant to decreased expression of FAS, FASLG and TRAIL along with
669 NS1 regulated proteins NFX1, NFX 2, NFX 3, NFX5, PIK3CA, PIK3CB, PIK3CD, PIK3R1,
670 PIK3R2, PIK3R, and PIK3R3. While the glycolysis pathway was significantly enriched in the
671 increased transcripts, when we input all transcripts that were significantly altered by IAV infection
672 we found a few proteins related to glycolysis were decrease (Fig 6D blue).

673 Importantly, when we compare the *in vitro* and *in vivo* IAV infected DC datasets we find
674 many similarities. In figure 6D, the overwhelming number of TipDC transcripts corresponding to

675 glycolytic proteins were increased. Likewise, most of the proteins in the glycolytic protein network
676 from *in vitro* IAV infected DC were increased (S1D Fig). In terms of glycolysis, TipDC significantly
677 increased hexokinase, phosphofructokinase, triosephophate isomerase, phosphoglycerate
678 kinase, and enzymes that convert pyruvate to acetyl CoA and lactate (Fig 6D). We then overlaid
679 gene symbols identified from the TipDC transcripts and *in vitro* differentiated DC proteins on the
680 enzymes of Glycolysis, pyruvate metabolism, and TCA cycle (Fig 7A). The glycolytic enzymes
681 tended to have positive log2 ratios, indicating an increase with IAV infection, while the TCA cycle
682 enzymes were skewed negatively (Fig 7A). Then we combined the transcripts from each
683 metabolic pathway compared them. We found the IAV to control log2 ratios of transcripts of
684 glycolytic enzymes were significantly higher than those of the TCA cycle for *in vitro* differentiate
685 DC (Fig 7B). Likewise, when we performed the same analysis of the TipDC isolated from mouse
686 lungs following IAV, we found a very significant difference in IAV to control log2 ratios of glycolysis
687 verse TCA cycle enzyme transcripts (Fig 7B). In both these cases, the values above zero log2
688 ratio reflect enzymes whose gene transcripts or protein peptides increased with IAV. Thus,
689 irrespective of strain used *in vitro*, *in vitro* or *in vivo* DC differentiation, or infection *in vitro* or *in*
690 *vivo* we find dendritic cells globally reprogram metabolism in response to influenza infection.

691 **Discussion**

692 Our data indicate dendritic cells alter their metabolism in response to IAV infection similar,
693 yet distinct from, our previous findings in human primary respiratory epithelial cells[1]. Unlike our
694 previous observation in epithelial cells, the only significant metabolic difference (p= 0.0102) in DC
695 infected with replicating and non-replicating virus was lowered proton leak (Fig 3C and S3C Fig).
696 This makes sense given IAV non-productively infects DC whereas epithelial cells are the primary
697 source of IAV propagation in the lungs and viral propagation requires high metabolic activity [79,
698 93, 94]. In our previous epithelial study, we found glycolysis was significantly lower in the absence
699 of viral replication and epithelial cells infected with replicating IAV lack metabolic flexibility and die

700 rather than adapt to changes in available nutrients [1]. In contrast, here we found IAV infection
701 increased DC glycolysis as well as capacity and flexibility for fueling respiration without loss of
702 viability in substrate limiting conditions (S4C Fig). These data reinforce the idea that metabolic
703 reprogramming of parasitized cells reflects aberrant changes driven by viral replication while
704 infected dendritic cells are harboring the virus while maintain metabolic control. However, we
705 found processes such as non-glycolytic extracellular acidification, non-mitochondrial oxygen
706 consumption, and glucose uptake were significantly lower when IAV was BPL inactivated. These
707 differences in DC transduction of signals that govern metabolic substrate import and product
708 export may be worthy of closer examination.

709 Viral infections, like those caused by IAV, have devastating consequences for cancer
710 patients, who often receive metabolic modulators in their treatment regimens that have the
711 potential to alter immune function. Our current findings, in the context of our previous work,
712 indicate the effects of these treatments may be cell and pathogen specific. Indeed, in the past 10
713 years there has been considerable focus on shared pathways in T lymphocytes and cancer
714 metabolism and more recently it has become clear that APC metabolism can also be altered by
715 activation with TLR agonists PMA and LPS [14, 16-19, 41, 95, 96]. However, little was known
716 about the metabolic demands of innate immune cells in response to IAV infection or IAV
717 associated TLR activation. Based on the work of pioneers in this field, we anticipated IAV and
718 LPS would have stark differences in bioenergetics [18, 19, 59, 61, 97]. Indeed, when we compared
719 IAV infection to LPS activated DC we found basal respiration, maximal respiration, coupling
720 efficiency, and ATP production were significantly increased (Fig 3C and S3C Fig). Perhaps the
721 most striking and significant difference was in glycolytic ATP production, where IAV infected DC
722 produced an average of 393.5 pmol/min/RFU 95%CI [259.9, 527.1] more ATP than LPS treated
723 DC (Fig 3D and Sup3D). Using both healthy controls and LPS as reference points, allowed us to
724 compare a spectrum of mitochondrial fitness and determine that IAV infected DC retain respiratory

725 function based on their FCCP response in the mitochondrial stress test (Fig 3). Further, while the
726 proportion of ATP production from OXPHOS was significantly lower than that produced by
727 glycolysis, the mitochondrial ATP production upon IAV infection was only reduced by 20% in DC
728 indicating that, unlike with LPS treatment, respiration was not severely impaired. However, we
729 were surprised to find DC stimulated by TLR agonists with considerable overlap in signaling
730 pathways (i.e. endosomal TLR3 and 7/8 viral RNA mimetics PolyIC or R848, respectively) had a
731 very different response to FCCP. This resulted in significant differences in maximal respiration,
732 spare respiratory capacity, coupling efficiency, and mitochondrial ATP production (S3C Fig). The
733 later was confirmed with an FCCP independent ATP rate assay that showed R848 produced
734 57.47 pmol/min/RFU 95%CI [-75.56, -39.38] less mitochondrial ATP than PolyIC ($p < 0.0001$)
735 even though both agonists increased DC glycolysis similarly (Fig 3A&D and S3D Fig). Thus, we
736 have highlighted an additional layer of complexity in the mechanisms underlying activated DC
737 metabolic rewiring and found that TLR agonists and IAV infections induce unique bioenergetics.
738 Future studies in this area will better dissect these signaling pathways and tease apart how they
739 orchestrate metabolic reprogramming.

740 Using quantitative proteomics and transcriptomics we found global rewiring of metabolism
741 early in the DC response to IAV infection *in vitro* and in TipDC 9 days following IAV infection *in*
742 *vivo*. We found a pronounced shift in metabolic protein abundance levels and localization in DC
743 resulting in significant enrichment of metabolic pathways, and this was validated by measuring
744 metabolism of specific substrates, extracellular and intracellular metabolite concentrations,
745 substrate product and flux rates for glycolysis and respiration, and bioenergetic functional assays
746 of ATP production or metabolic capacity and flexibility**.** Combined these observations delineate
747 the central features of the metabolic response of DC to IAV infection, showing a significant
748 increase in glycolysis and glycolytic ATP production, that is decoupled from canonical pyruvate
749 oxidation in the TCA cycle in favor of utilizing glutamine. This phenomenon is reminiscent of

750 Warburg metabolism, a phenotype that reflects an increase in demand for anabolic metabolites
751 and the energy to assemble them into macromolecules necessary for cell proliferation. Further,
752 this metabolic reprogramming has been shown to be pivotal for proliferation and effector functions
753 of other immune cells [14, 15, 39-42, 84, 85, 96, 98]. Given IAV infected DC have increased
754 capacity to utilize diverse substrates and the flexibility to toggle between them, we are currently
755 unable to fully explain why inhibiting oxidation of specific substrates in the mitochondria would
756 significantly reduce migration or effect DC priming of T cells (Fig 2&5). However, these
757 mitochondrial inhibitors did not ablate the DC response to infection, and this may indicate the
758 metabolic compensation by DC to use suboptimal mitochondrial fuels comes at a cost that
759 diminishes their effector function. Our findings extend our understanding of immune metabolism
760 into influenza infection of a critical cell type that bridges innate to adaptive immunity and
761 establishes an appropriate *in vitro* model to study of this metabolic phenomenon.

762 It has long been appreciated that DC migration from the lungs to draining lymph nodes is
763 critical to mounting an effective immune response to IAV, and motility is an energy-demanding
764 process that is directly coupled to ATP availability [79, 90, 99, 100]. We observed a dramatic
765 increase in DC mobility following IAV infection and found IAV-infected DC derive approximately
766 17 times more ATP from glycolysis than mitochondrial OXPHOS corresponding to 10 fmol/min
767 verses 0.6 fmole/min per infected DC (Fig 5A and 3D). One intriguing possibility is that this pool
768 of glycolytic ATP is critical for infected DC trafficking. In support of this, we found inhibiting c-Myc
769 abolished IAV induced glycolysis and translocation of DC (Fig 4B and 5A). IAV-infected DC
770 appear to acquire a high level of plasticity in energy substrate metabolism, including greater
771 carbon and energy source flexibility. Indeed, decoupling of glycolysis and TCA cycle in cancers
772 was once presumed to be a mitochondrial defect but is now postulated to produce a more robust
773 and flexible metabolic program [43, 101]. c-Myc is considered a master regulator of cancer
774 metabolism, and metabolic reprogramming by c-Myc is thought to allow cancer and activated

775 immune cells to sustain supplies of anabolic building blocks while generating energy for their
776 assembly[14, 63, 64, 68, 72]. Our data supports applying this idea to IAV-infected DC, given we
777 found c-MYC expression increased in response to IAV infection and c-Myc inhibition significantly
778 reduced glycolysis, respiration, and glutamine import, while preventing IAV-induced DC migration
779 and induction of CD25+ and CD44+ CD8 T cells (Figs 4, 5A-F, and S5E Fig). However, an
780 important and related recent discovery is that, as DC mature they down regulate expression of c-
781 MYC and n-MYC while maintaining constant expression of l-MYC even after activation [68, 69].
782 Paradoxically, mice with l-MYC-deficient dendritic cells have reduced T cell response during either
783 bacterial or viral infection [68, 69]. In this respect, while it is possible that our reagents were
784 nonspecific we suggest that is unlikely for several reasons: the primers we used are specific for
785 c-MYC [102], these primers only amplified one species, and the c-Myc antibodies we used
786 detected a single band at the appropriate size. Moreover, we observed a transient increase in
787 response to activation stimuli (i.e. IAV infection) at the RNA and protein levels, whereas others
788 report l-MYC remains constant in activated DC [69]. Importantly, we found c-Myc inhibitor
789 treatment blocked or diminished critical DC immune functions. The exact cause of this effect
790 remains unclear, but it correlates with a loss of DC glycolytic response to IAV. With respect to the
791 interplay of the Myc paralogs and determining their specific roles in relationship to DC stimuli,
792 phenotype, and pathogen response there remains an open questions [69, 103] that now include
793 the specific role of c-Myc in IAV infection.

794 In addition to its other roles in cancer metabolism, c-Myc directly regulates glutaminase,
795 transcriptionally activates glutamine transporters, promotes glutamine metabolism including
796 glutamine catabolism to glutamic acid for anaplerosis and NADPH, and in cancer c-Myc
797 transcriptionally coordinates increased glutaminolysis, dependence on exogenous glutamine and
798 glutamine addiction that is c-Myc dependent and can't be rescued by anti-apoptotic proteins or
799 TCA intermediates[65, 66, 104-109]. In cancer, glutamine utilization confers several advantages

800 over classical glycolysis coupled to TCA cycle for energy production. This is primarily because
801 during the conversion of glutamate to α-ketoglutarate, and steps that follow it, normal levels of
802 reducing equivalents are produced independently of Acetyl CoA, glycolysis, and FAO while
803 supplying ample building blocks for *de novo* protein synthesis, purine nucleoside biosynthesis,
804 and *de novo* fatty acid and cholesterol biosynthesis. Thus, glutamine metabolism has the added
805 benefit of increasing proton buffering capacity and cellular redox homeostasis including
806 glutathione synthesis from glutaminase enzymes [71, 110] and when glutaminolysis is inhibited
807 ROS increases [111]. Meanwhile, the first step of the TCA cycle is sensitive to ROS [64, 112-114]
808 as is the respiratory chain and membrane permeability, and this mitochondrial damage
809 potentiates ROS [115, 116]. Hence, it is conceivable that glutamine oxidation may have important
810 advantages for an activated innate immune cell that produces ROS in conjunction with other
811 effector functions that require high anabolism and energy production. This is consistent with our
812 observations that infected DC redirect a large portion of pyruvate away from the TCA cycle while
813 simultaneously increasing glutaminolysis, capacity for oxidizing glutamine, glutamine import and
814 significantly depleting intracellular glutamine concentrations and α-ketoglutarate concentrations if
815 the mitochondrial pyruvate carrier in inhibited and increase c-Myc (Fig 2C&D, 4A, and S2E Fig).
816 Recently sustained import and utilization of glucose and glutamine were shown to stabilize c-MYC
817 and were required for T cell renewal and clonal expansion [117]. Determining the mechanistic
818 underpinnings of glutamine utilization in dendritic cells will advance our understanding of their
819 basic metabolism and will lead to a clearer picture of immune function in the IAV-infected lung
820 microenvironment.

821 In conclusion, our findings support the view that dendritic cells specifically rewire their
822 metabolism based on activation stimuli or IAV infection and the latter significantly increased
823 glycolysis, glycolytic ATP production, glutaminolysis, and metabolic plasticity concomitant to
824 reducing pyruvate utilization in the TCA cycle. This metabolic reprogramming is preceded by a

825 transient increase in c-Myc expression and ablating its activity restored normal glycolysis and
826 motility and reduced T cell priming. We clearly demonstrated IAV infected DC acquires the
827 majority of ATP from glycolysis, nevertheless restricting mitochondrial fuels significantly impairs
828 DC function. Collectively our data indicate increased metabolic rewiring and plasticity while also
829 highlighting the impact of specific metabolic substrates on DC migration and T cell priming. This
830 is significant, given reducing DC migration after viral infection profoundly reduces the amplitude
831 of the T cell response and the strength of antigenic stimulation regulates T cell progression [90,
832 118]. It remains to be determined if these restraints on DC metabolism result in a defect in antigen
833 capture, processing or MHC loading/presentation, or if long term quantity or quality of expanded
834 virus-specific T cells is impacted. Importantly, it appears dendritic cells orchestrate coordinated
835 bioenergetic and metabolic changes in response to IAV infection irrespective of strain and are
836 similar regardless of DC origin or infection model (i.e. *in vitro* differentiated or lung Tip DC and *in*
837 *vitro* or *in vivo,* respectively). Although incomplete, these data suggest the net result of blocking
838 metabolic reprogramming therapeutically in patients or limiting metabolites *in situ* could have
839 detrimental consequences in terms of mounting an appropriate immune response. It is also
840 tempting to postulate that local metabolite depletion in the lung may act to limit lung injury by
841 placing a governor on the immune response. However, the metabolite milieu of the IAV-infected
842 lung and lung-lining fluid has not been well established, and this must be addressed to determine
843 if variability in metabolite concentrations impact cellular responses or secondary infections. It also
844 remains to be determined if metabolic reprogramming occurs in humans with community-acquired
845 respiratory viral infections and, if so, if it can be exploited therapeutically to enhance or reduce
846 the immune response to IAV.

847 Materials and Methods

848 **Ethics Statement:** All experiments using mice were done in compliance with the Guidelines of
849 Care and Use of Laboratory Animals and approved by University of Tennessee Health Science

850 Center Animal Care and Use Committee. Experiments were conducted under IACUC protocol #
851 16-138.0.

852 **Tissue Culture and Mouse work**.

853 **Bone marrow derived dendritic cells (DC).** Female C57BL/6J (B6) mice purchased from The
854 Jackson Laboratory (Bar Harbor, ME) and were maintained in specific-pathogen-free facilities at
855 the University of Tennessee Health Science Center (UTHSC), Memphis, TN. Primary bone
856 marrow derived dendritic cells were isolated and differentiated as previously described (104).
857 Briefly, after removal of the epiphysis bone marrow was flushed out, red blood cells lysed, cell
858 viability determined with AO/PI and 2 million viable precursors per 100 cm^2 polystyrene plate were
859 seeded in 10 ml RPMI supplemented with Penicillin (100 U/ml), Streptomycin (100 µg/ml), fetal
860 bovine serum (10% v/v) (Gibco Grand Island, NY) and 20 ng GM-CSF (R&D systems,
861 Minneapolis, MN) per ml medium. 20 ng GM-CSF/ml medium was supplemented on days 3, 6,
862 and 8 then DC were harvested on day 10.

863 **T cell isolation.** Mice were chemically restrained with 2,2,2-tribromoethanol (Sigma Aldrich) with
864 a dose adjusted to the individual body weight and infected intra-nasally with 10^4 LD_{50} of PR8 dose
865 of virus in 30 µl of sterile PBS. Weight loss and survival of infected mice were monitored daily
866 over a 21-day period. Mice were sacrificed and spleens harvested from virus challenged (primed)
867 or naïve 8-12 week-old C57BL/6 or C57BL/6-Tg(TcraTcrb)1100Mjb/J (OT1) male and female
868 mice. T cells from challenged mice were only used for flow cytometry experiments. Spleens were
869 manually disrupted by grinding organ tissue between the frosted ends of two sterile glass
870 microscope slides in sterile PBS containing 2% fetal bovine serum. T cells were isolated by
871 magnetic separation using EasyStep™ Mouse CD8+ T Cell Isolation Kit with anti-CD8 magnetic
872 beads (StemCell™ Technologies) (purity>99%) for CD8+T Cells or EasySep™ Mouse T Cell
873 Isolation Kit (StemCell™ Technologies) for T cells isolation by negative selection.

874 **Intranasal infection and lymphocyte isolation.** Female and male 6–8 week-old C57BL/6 mice
875 were purchased from Jackson Laboratories (Bar Harbor, ME). All mice were acclimated for two
876 weeks prior to inoculation with IAV. All infections were conducted in an ABSL2+ facility where
877 animals were assessed daily. Those with severe morbidity (greater than 30% weight loss plus
878 severe clinical impairment) were humanely euthanized according to our approved protocol. Prior
879 to intranasal delivery of 30 µl of virus diluted at EID_{50} 2000 the mice were chemically restrained
880 by intraperitoneal injection of 2,2,2-tribromoethanol (Avertin). Throughout the course of the
881 infection mice were monitored by daily weighing and assessment of the clinical distress symptoms
882 (e.g. ruffled fur, hunched back, lethargy etc.). At day 0 or 9 mice were euthanized and the lungs
883 were collected after perfusion *in situ* via the ventricles with 40–50 ml of PBS. The lungs were
884 rinsed with PBS, minced with fine scissors and gently pushed through a 40-µm strainer with a
885 syringe plunger. The suspension was then washed with Click's medium and incubated in digestion
886 buffer (Click's plus 50 U/ml collagenase IV and 0.001% DNase I (Sigma-Aldrich)) for 30-90
887 minutes at 37°C on a rocking platform. Lungs tissue was then passed through a 1µm sieve and
888 cells collected, washed (40 ml of Click's medium), and resuspended in sterile 2%-PBS.
889 Lymphocytes were isolated with percoll density gradient.

890 **Virus propagation and titer.** A/PuertoRico/8/34, referred to in the text as IAV, is a mouse
891 adapted highly pathogenic influenza virus (PR8) [119]. This virus was cultured in pathogen free
892 antibiotic treated eggs (generously provided by Dr Paul Thomas) that was inoculated on day 9 in
893 bulk from a single viral stock each. Allantoic fluid was harvested 48 hours following inoculation
894 and aliquoted into 50 ml conical tubes and stored at -80°C. Individual bulk viral stock was then
895 thawed, aliquoted, stored at -80°C and titer was determined. Tissue culture infectious dose at
896 50% ($TCID_{50}$) were then determined by serial dilution on near confluent Madin-Darby canine
897 kidney (MDCK) cells (purchased from American Type Culture Collection (ATCC CCL-34)) in the
898 presence of 1 mg/ml trypsin (Sigma Aldrich), verified with 50% egg infectious doses (EID_{50}) and

899 calculated according to the Reed and Muench method [120]. A/PuertoRico/8/34 virus was added
900 at a multiplicity of infection (MOI) of 5 for 2 hours to DC. Virus laden medium or blank infection
901 medium was then removed, and the infection was allowed to proceed for indicated times.

902 **Proteomics: sample preparation, mass spectrometry, and data processing.**

903 We have previously described these proteomics methods elsewhere in detail. Details regarding
904 sample acquisition, MS parameters, and data processing can be found in Smallwood et al 2011
905 **(**PMCID: PMC3241613). Details specific to quantitative proteomics using isobaric tags can be
906 found in Smallwood et al 2017 [1]. Details specific to quantitative proteomics using stable
907 isotopically labeled proteomics see Lopez-Ferrer et al 2009 [23]. Brief summaries of pertinent
908 details are also provided below.

909 **Sample Preparation.** DC were infected for 17 hours with PR8 (MOI 5 or 1) followed by lysis,
910 homogenization, and fractionation by centrifugation. iTRAQ samples were tryptically digested by
911 using a FASP Protein Digestion Kit (Protein Discovery, San Diego, CA) according to the
912 manufacturer's instructions with slight modifications (Supplemental Data), samples were desalted
913 by C18 solid-phase extraction (SPE) before isobaric labeling (SUPELCO). Digested samples
914 were then processed according to the manufacturer's directions for iTRAQ 4-plex labeling
915 (ABSciex). A separate set of DC samples was processed by performing trypsin-catalyzed ^{18}O
916 labeling. Before fractionating via high-pH reverse-phase fractionation with concatenated pooling,
917 samples were desalted by C^{18} SPE (SUPELCO). All samples were processed in a custom liquid
918 chromatography system using reversed-phase C^{18} columns. The iTRAQ samples were analyzed
919 by using a Velos Orbitrap mass spectrometer (Thermo Scientific), and ^{18}O-labeled samples were
920 analyzed by using an LTQ-Orbitrap mass spectrometer (Thermo Scientific). Both systems were
921 equipped with custom ion funnel–based atmospheric pressure ionization sources and
922 electrospray ionization interfaces.

923 **Data processing**. Raw files were compared with a concatenated NCBI *Mus musculus* database
924 and contaminant database by using SEQUEST v.27 (rev. 12). The resulting sequence
925 identifications were rescored by using MS-GF and filtered to a 1% false-discovery rate by using
926 the target-decoy approach and MS-GF–derived spectral probabilities. Reporter-ion intensities
927 were quantified by using the MASIC tool (2). Missing reporter ion channel results were excluded
928 from analysis. Redundant peptide identification reporter ions were summed across fractions, and
929 median central tendency normalization was used to account for channel bias and then log_2-
930 transformed. Soluble and insoluble fractions were analyzed separately by using DanteR software.
931 The analysis of variance model included treatment and peptide effects. The remaining treatment
932 effect and p-value were calculated by using Student's *t*-test. Benjamin-Hochberg multiple-testing
933 error correction was applied to the results of this hypothesis testing, and proteins having a p-value
934 ≤0.05 were considered statistically significant.

935 **Bioinfomatics**. Peptide identifiers were converted to ENSEMBL and ENTREZID gene identifiers
936 and protein names with DAVID. The log2 ratio of statistically significant peptides was converted
937 to fold change and the soluble and insoluble proteins were separated by fold change (i.e.
938 increasing and decreasing ≥2-fold). iTRAQ and SIL proteomes were combined, and redundancies
939 removed by selecting the most significant peptide. The ≥2-fold protein lists were then submitted
940 to DAVID for enrichment analysis as previously described [24]. KEGG Orthology (KO) pathways
941 were then cross referenced with KO Class and subcategory. Network summary of localization
942 changes in confidently identified proteins with significant enrichment in metabolic pathways was
943 performed as previously described [25]. Briefly, subclasses of KO metabolic proteins were
944 organized based on location in the soluble or insoluble fraction and connected to protein nodes
945 with red or blue edges based on increasing or decreasing abundance, respectively. Protein nodes
946 were then colored by KEGG subclass: carbohydrate metabolism (red), amino acids metabolism
947 (orange), nucleotide metabolism (purple), energy metabolism (green), lipid metabolism (yellow),

948 and glycan biosynthesis and metabolism (blue). Cytoscape network was built essentially as
949 previously described [121]. Briefly, we submitted both the soluble and insoluble SIL proteomes to
950 DAVID to select proteins in the KEGG glycolysis pathway. We used PPI spider to determine the
951 glycolytic protein-protein interaction network [122]. We then mapped the interaction network to
952 the glycolytic network and used Cytoscape to overlay abundance data from the proteomes.

953 **Transcriptomics: sample preparation, RNA Seq, and data processing.**

954 **Sample preparation.** RNA was extracted from sorted Tip DC using 1 mL TRIzol reagent
955 (Invitrogen). RNA was extracted from Trizol suspensions using the Zymo Research Direct-zol
956 RNA miniprep kit, treated with 10 U DNAse for 20 min at RT and then concentrated using the
957 Qiagen RNeasy MinElute clean up kit. Purified RNA quality checked using the Nano Total RNA
958 kit on an Agilent 2100 Bioanalyzer.

959 **RNA seq.** We used Illumina's TruSeq RNA v2 sample preparation protocol according to
960 manufacturer's instructions for generation of RNA-seq libraries. Briefly, this protocol involved the
961 following steps: A. cDNA Synthesis: mRNA was purified via oligo(dT) beads followed by
962 fragmentation using divalent cations and heat. The 1st strand cDNA synthesis was performed
963 using random primers, followed by 2nd strand cDNA synthesis. B. cDNA library preparation.
964 cDNA fragments were DNA blunt end repaired followed by addition of 3' adenylation of DNA
965 fragment. Sequencing adapters were then ligated to the ends utilizing T-A pairing of adapter and
966 DNA 2 fragments. This was then followed by PCR amplification of the library. The cDNA libraries
967 were run on an Illumina HiSeq2000.

968 **Data Processing**. Data quality was checked with fastqc software. Paired end RNA-Seq data was
969 aligned to Mouse mm10 genome using TopHat (with Bowtie2). Only concordant pairs with
970 mapping quality > 10 were kept. The number of reads assigned to each gene was found using
971 Bioconductor R package. Count data was analysed using edgeR Bioconductor package (GLM

972 formulation). Before doing this genes, which did not have >= 3 counts in every sample for at least
973 one group, were filtered out. Genes were declared DE if they had FDR < 0.05 and log2 FC > 1.
974 Multidimensional Scaling (MDS) as implemented in EdgeR function plotMDS (in two dimensions)
975 was used for data visualization. Briefly, MDS takes as input the set of pairwise distances between
976 any two samples and plots points in 2-dimensional space (plane) attempting to preserve as much
977 as possible the original distances between any two samples.

978 **Bioinfomatics**. Transcript identifiers were converted to official gene symbols with DAVID and
979 linked to expression levels in Excel. The XLSTAT OMICS data analytics package was used for
980 generating the heat map and expression analysis. Differential expression was determined from
981 three day 0 controls and four day 9 IAV infected samples. The standard deviation threshold for
982 this analysis was 50%, eliminating 6,643 transcripts out of 13,285. Significant differences in
983 expression were selected based on p-values generated from a parametric comparison of
984 differences using Tukey honest significant difference test for multiple comparisons with Benjamini-
985 Hochberg post-hoc corrections.

986 **Metabolic assays.**

987 **Metabolite depletion – Live/dead viability assay.** DC were cultured as described above. After
988 24 hours of adherence, RPMI 1640 complete medium was replaced with fresh RPMI 1640
989 complete medium or RPMI metabolite depleted medium for 3 hours (*i.e.* RPMI without glucose or
990 without glutamine or without both, respectively). Later the cells were treated as above in complete
991 or deplete media followed by infection for 17 hours. The cells were labelled with calcein-AM (2μM)
992 and EthD-1(4μM) incubated for 20 minutes at room temperature and the viability was measured
993 using Live/Dead Viability/Cytotoxicity assay kit for mammalian cells (Thermo Scientific) with a
994 fluorescent plate reader at 494/517nm and 528/617nm, respectively.

995 **Metabolic Flux.** Glycolytic flux was determined by measuring the detritiation of [3-^{3}H]glucose
996 (Sigma Aldrich) as previously described [123]. Fatty acid beta-oxidation flux was determined by
997 measuring the detritiation of [9,10-^{3}H]-palmitic acid (Sigma Aldrich) as previously described [124].
998 Glutamine oxidation flux was determined by calculating the rate of $^{14}CO_2$–release from [U-^{14}C]-
999 glutamine (Sigma Aldrich) as previously described [125]. Pyruvate oxidation flux was determined
1000 by calculating the rate of $^{14}CO_2$–release from [2-^{14}C]-pyruvate (Sigma Aldrich) as previously
1001 described [126]. Glucose oxidation flux through the pentose phosphate pathway (PPP) was
1002 determined by calculating the rate of $^{14}CO_2$–release from [1-^{14}C]-glucose (Sigma Aldrich) as
1003 previously described [14, 127]. The concentration of free fatty acids (≥C8) was determined using
1004 the Free Fatty Acid Assay (AbCam) by a coupled enzyme assay which results in a fluorometric
1005 assay with the fluorescent emission/excitation wavelengths 535/587 nm. The resulting
1006 fluorometric product was proportional to the free fatty acids present and quantifiable with the
1007 palmitic acid standards.

1008 **Glucose and Glutamine Quantification.** DC were treated as above and after 17 hours cells or
1009 supernatants were collected alongside blank medium controls incubated together but without
1010 cells. Extracellular glucose was quantified with a glucometer against glucose standards essential
1011 as previously described [1]. Glucose levels (mg/dl) in the blank medium was determined alongside
1012 DC +/- treatments. Glucose uptake was calculated by subtracting the glucose in the control, IAV,
1013 IAV^{BPL}, PolyIC, R848 or LPS medium from the cell free blank medium. Internal and external
1014 glutamine was quantified from supernatant and cell lysates, respectively, following the
1015 Glutamine/Glutamate Glo assay manufacturer's protocol (Promega). Upfront sample processing
1016 such as dilution is required to fit in to the linear range of the glutamine or glutamate standard
1017 curve. All the standard and sample dilutions were prepared in PBS and for each assay 25 µl
1018 sample and 25 µl standard were transferred to a 96 well luminescence assay plate and 25 µl of
1019 Glutaminase Buffer was added. The reactions were incubated for 30 minutes at room

1020 temperature. Later, 50µl of Glutamate Detection Reagent was added and incubated for additional
1021 60 minutes. The metabolite detection was done using bioluminescent NADH detection method
1022 consisting of glutamine conversion to glutamate by Glutaminase and glutamate detection with the
1023 Glutamate Detection Reagent (containing glutamate dehydrogenase, NAD+, Reductase,
1024 Reductase Substrate and Luciferase) and luminescence was measured using BMG CLARIOstar
1025 microplate reader.

1026 **Bioenergetic assays on the Xfe96 bioanalyzer.**

1027 ECAR, OCR, and PPR were measured by using the XFe-96 Extracellular Flux Analyzer (Agilent).
1028 We first optimized seeding density, plate coatings, and inhibitor concentrations. The final
1029 concentrations were: 10 mM Glucose, 50mM 2-DG, 1µM Oligomycin, 2µM FCCP, and 0.5µM
1030 antimycin/rotenone. We essentially followed the manufacture's protocols. Briefly, $1.5x10^5$ cells
1031 per well in Poly D-Lysine coated Seahorse XFe96 microplates at 37°C in 5% CO_2 for 24 hours.
1032 The cells were either left untreated (control) or infected for 17 hours at (MOI) of 5 using viable
1033 virus or IAV^{BPL} or treated with LPS (50ng/ml), PolyIC (1µg/ml), or R848 (1µg/ml). At the end of 17
1034 hours of infection the cells were switched to XF base medium (non-buffered DMEM with no phenol
1035 red). XF media was supplemented with L-glutamine (2 mM) for Glyco stress test or with glucose
1036 (10 mM), L-glutamine (2 mM), and sodium pyruvate (1 mM) for Mito stress test and ATP assay.
1037 Injection cartridges were hydrated overnight, cells equilibrated for 1 hour and ECAR, OCR, and
1038 PPR monitored for 2 hours. After each run cells per well were quantified with CyQUANT™
1039 (Thermo Scientific) to derive normalization factors. Rates were calculated using the Seahorse XF
1040 real time report generator and imported to GraphPad for statistical analysis.

1041 **Glyco and Mito stress test with c-MYC inhibitor.** DC were seeded as described above and
1042 were left untreated (control), pretreated with c-Myc Inhibitor (MilliporeSigma) for 4 hrs at 0.5 uM,
1043 1.0 uM, and 2.0uM respectively, infected for 17 hours at (MOI) of 5 with PR8 viable virus.

1044 **Mito Fuel Flex Test.** DC were treated as described above. Calculations were performed with the
1045 Seahorse Mito Fuel Flex Test Report Generator plug in for excel and inhibitor injections
1046 essentially followed manufacturer protocols using sequential or combined injections of 4 μM
1047 etomoxir, 3 μM BPTES, and 2 μM UK5099. Targets and calculations are briefly summarized:

Test	Injection 1	Injection 2
Glucose Dependency	UK5099	BPTES/Eto
Glutamine Dependency	BPTES	UK5099/Eto
Fatty Acid Dependency	Etomoxir	UK5099/BPTES
Glucose Capacity	BPTES/Eto	UK5099
Glutamine Capacity	UK5099/Eto	BPTES
Fatty Acid Capacity	UK5099/BPTES	Etomoxir

$$\left[\frac{Baseline\ OCR - Injection\ 1\ OCR}{Baseline\ OCR - Injection\ 2\ OCR}\right] * 100\% \qquad (1)$$

$$\left[1 - \left[\frac{Baseline\ OCR - Injection\ 1\ OCR}{Baseline\ OCR - Injection\ 2\ OCR}\right]\right] * 100\% \qquad (2)$$

1059 Dependency Equation (1), Capacity Equation (2), and Flexibility (i.e. the difference between the
1060 capacity and the dependency for each substrate) were calculated with Seahorse XF Flex Fuel
1061 Report generator and imported to GraphPad for statistical analysis. The combined percent
1062 oxidation capacity or dependence is the sum of the individual values for glucose, glutamine, and
1063 fatty acids.

1064 **Functional Assays.**

1065 DC were untreated (control) or pretreated with 2 μM cMyc inhibitor (MI), 3 μM Bis-2-(5-
1066 phenylacetamido-1,3,4-thiadiazol-2-yl)ethyl sulfide (BPTES), 2 μM UK5099, or 4 μM etomoxir
1067 (Eto) respectively for 4 hours then infected for 17 hours with IAV at MOI of 5. Fresh T cells
1068 (purified as described above) were added to DC at 1:5 ratio and incubated for 24 and 48 hours.

1069 **Cell migration assay**. DC were seeded on Poly-D-lysine 100 ug/ml (Sigma Aldrich) precoated
1070 Oris™ 96-well migration plate (Platypus Technologies) at the density of $1x10^5$ per well with silicon
1071 stoppers in place. Cells were maintained at 37 °C in a humidified incubator with 5% CO2
1072 overnight. After attachment, stoppers were removed, growth media replaced and the DC cells

1073 were treated with c-MYC inhibitor (2 uM), BPTES (3 uM), etomoxir (4 uM) or UK5099 (2 uM) and
1074 infected with PR8 for up to 17 hours at (MOI) of 5. Following incubation, the cells were rinsed
1075 with PBS and labelled with calcein-AM for 20 minutes at 37 °C from Live/Dead
1076 Viability/Cytotoxicity kit for mammalian cells (Thermo Scientific). After staining, plate was read on
1077 BMG CLARIOstar plate reader with FITC excitation/emission filter 485/528nm. The combined
1078 effects of migration and stimulation were evaluated by comparing the fluorescent signal detected
1079 in the non-infected wells to the signal in the virus infected wells. Data tables from multiple
1080 experiments were combined and plotted in GraphPad Prism.

1081 **FITC-dextran phagocytosis.** Cellular uptake of FITC-dextran was determined as reported earlier
1082 [128]. DC were left untreated (control) and pretreated with cMyc (2 μM), BPTES (3 μM) and
1083 UK5099 (2 μM) and etomoxir (4 μM) respectively, infected for 17 hours at (MOI) of 5 with PR8
1084 viable virus and LPS (50 ng/ml) as positive control. After 17 hours of infection cells were labelled
1085 with 1 mg/ml FITC-Dextran 40S (Sigma Aldrich) and incubated for 1 hour at 37°C and 4°C,
1086 respectively. Uptake was terminated by washing the cells 3x with ice-cold PBS. Cells were
1087 resuspended in FACS buffer (PBS containing 2% bovine serum albumin and 0.1% sodium azide).
1088 FITC fluorescence of cells was measured using Sony SH800 cell sorter (Sony, Japan).
1089 Fluorescence values were reported as mean fluorescence intensity (MFI).

1090 **Flow cytometry.** Fluorescence-activated cell sorting (FACS) analysis was performed using
1091 standard methodology. Briefly, after Fc blocking, 1 × 10^6 cells were stained with appropriate
1092 antibodies for 30 min at 4° and then washed with phosphate-buffered saline (PBS)/2% FBS. The
1093 cells were stained in FACS buffer (PBS containing 0.5% bovine serum albumin and 0.05% sodium
1094 azide) with fluorescently labelled antibodies from BioLegend (CD11c-APC/Cy7, CD11b-BV421,
1095 CD40-FITC, CD80-APC, CD86-PE, CD8-PE/Cy7, CD4-PerCp/Cy5.5, CD69-PE, CD25-APC,
1096 CD3-BV421, CD44-BD427, CD45.1-FITC, CD3-PerCp/Cy5.5, and CD44-FITC) or Tonbo
1097 Biosciences (HLA-DR-PerCp/Cy5.5) to identify DC and T cells. Percentage for each marker was

1098 determined by flow cytometry on a Sony SH800 cell sorter and data were analyzed using FlowJo
1099 software (Tree Star, San Carlos, CA). Fluorescence minus one (FMO) control for each marker
1100 used to identify gating boundaries. DC responses were examined by flow cytometry after staining
1101 with anti-CD11c, -MHCII, -CD8, -CD4, -CD11b, -GR-1, -CD103, -CD80, and -CD86 antibodies.
1102 TipDC were sorted using CD11b^{hi}, Ly6c/GR-1^{hi}, MHCII ^{hi} DC surface marker staining on a FACS
1103 Aria cell sorter (BDbioscience).

1104 **T cell activation assay.** CD8+ T cells were isolated and co-cultured with drug treated and/or
1105 infected DC in 1:5 ratio (DC/T cell) for 24 hours at 37 °C with 5% CO2. Extracellular acidification
1106 rate (ECAR) was measured to detect T cell activation in real time using anti-CD3/CD28-coated
1107 DynaBeads (Life Technologies) on Xfe96 (Agilent) as previously described [85-88]. ECAR was
1108 measured in unbuffered RPMI without phenol red supplemented with glucose (10mM), L-
1109 glutamine (2 mM), and sodium pyruvate (1 mM) final concentrations per well. Three rate
1110 measurements were done to establish basal rate followed by 15 cycles of real-time
1111 measurements of ECAR. Data files were converted to excel files using Wave 2.4.1. Data tables
1112 were combined from multiples experiments and plotted and analyzed in GraphPad Prism.

1113 **RNA and protein assays.**

1114 **Quantitative Real-time PCR.** RNA was isolated from cultured DC and or treated with cMyc for
1115 4, 8 and 17 hours by using Direct-zol RNA MiniPrep Kit (Genesee Scientific) as per the
1116 manufacturer's instructions. cDNA synthesis was performed using the iScript^{TM} cDNA Synthesis
1117 Kit (Bio-Rad) per the manufacturer's instructions. The cDNA synthesis used 7 µl of reaction mix
1118 consisting of 4 µl 5× iScript reaction mix, 1 µl iScript reverse transcriptase, with the remainder
1119 nuclease-free H2O. This was incubated at 25°C for 5 minutes, 42°C for 30 minutes, and 85°C for
1120 5 minutes. Real time RT-PCR was performed using the SYBR^{TM} Green mastermix (Applied
1121 Biosystems). Simple relative quantification of target gene expression normalized to βeta
1122 actin was performed using the $2^{-\Delta\Delta Ct}$ method [129]. The following primers were used: cMyc,

1123 forward primer: 5′- CGGACACACAACGTCTTGGAA-3′; cMyc, reverse primer: 5′-
1124 AGGATGTAGGCGGTGGCTTTT-3′, the primers were purchased from Integrated DNA
1125 Technologies.

1126 **Immunoblotting**. Cells were rinsed and pelleted and the pellets were homogenized on ice in a
1127 cold Tris-EDTA+0.1% NP-40 lysis buffer. 15 µg of lysates were reduced in NuPAGE reducing
1128 reagent (Invitrogen) and boiled for 5 min prior to loading in 4-12% NuPAGE Bis-Tris Gel for
1129 separation by electrophoresis. Proteins were transferred to nitrocellulose membrane and blocked
1130 with 3% bovine serum albumin (Thermo Scientific) in 1XTBST for 1 hour. The membrane was
1131 incubated with cMyc overnight at 4°C followed by washing and incubation with horseradish
1132 peroxidase (HRP) secondary antibody. The protein bands were detected using ECL plus
1133 (Amersham) on Amersham Imager 600 (GE Healthcare).

1134 Acknowledgments

1135 Portions of this research were supported by: Le Bonheur Children's Hospital and the Children's
1136 Foundation Research Institute https://www.lebonheur.org/research-and-education/research/
1137 (H.S.), National Institute of Health National Center for Research Resources (Grant RR018522)
1138 https://www.nih.gov/research-training/research-resources (L.P.), The W.R. Wiley Environmental
1139 Molecular Science Laboratory: a national scientific user facility sponsored by the U.S. Department
1140 of Energy's Office of Biological and Environmental Research and located at the Pacific Northwest
1141 National Laboratory, which is operated by Battelle Memorial Institute for the U.S. Department of
1142 Energy under contract DE-AC05-76RL0 1830 (User proposal numbers 37501 & 34745)
1143 https://www.pnnl.gov/environmental-molecular-sciences-laboratory (H.S.), National Institute of
1144 Health (1UO1CA232488-01 and 1R01AI114581) https://www.nih.gov/ (R.W.), National Institute
1145 of Health National Institute of Allergy and Infectious Diseases (R56AI091938 and
1146 HHSN266200700005C)) https://www.niaid.nih.gov/ (P.T.), and American Lebanese Syrian

1147 Associated Charities (ALSAC) https://www.stjude.org/about-st-jude/faq/whats-alsac.html (P.T.).
1148 The funders had no role in study design, data collection and analysis, decision to publish, or
1149 preparation of the manuscript.

1150 We thank Richard Cross and Greig Lennon for cell sorting and assistance in flow cytometry.

1151

1152 # References

1153 1. Smallwood, H.S., et al., *Targeting Metabolic Reprogramming by Influenza Infection for*
1154 *Therapeutic Intervention.* Cell Rep, 2017. **19**(8): p. 1640-1653.
1155 2. Vermaelen, K. and R. Pauwels, *Pulmonary dendritic cells.* Am J Respir Crit Care Med, 2005. **172**(5):
1156 p. 530-51.
1157 3. von Garnier, C., et al., *Anatomical location determines the distribution and function of dendritic*
1158 *cells and other APCs in the respiratory tract.* J Immunol, 2005. **175**(3): p. 1609-18.
1159 4. Stumbles, P.A., J.W. Upham, and P.G. Holt, *Airway dendritic cells: co-ordinators of immunological*
1160 *homeostasis and immunity in the respiratory tract.* APMIS, 2003. **111**(7-8): p. 741-55.
1161 5. McGill, J., J.W. Heusel, and K.L. Legge, *Innate immune control and regulation of influenza virus*
1162 *infections.* J Leukoc Biol, 2009. **86**(4): p. 803-12.
1163 6. Guillot, L., et al., *Involvement of toll-like receptor 3 in the immune response of lung epithelial cells*
1164 *to double-stranded RNA and influenza A virus.* J Biol Chem, 2005. **280**(7): p. 5571-80.
1165 7. Lund, J.M., et al., *Recognition of single-stranded RNA viruses by Toll-like receptor 7.* Proc Natl Acad
1166 Sci U S A, 2004. **101**(15): p. 5598-603.
1167 8. Le Goffic, R., et al., *Cutting Edge: Influenza A virus activates TLR3-dependent inflammatory and*
1168 *RIG-I-dependent antiviral responses in human lung epithelial cells.* J Immunol, 2007. **178**(6): p.
1169 3368-72.
1170 9. Hammerbeck, D.M., et al., *Administration of a dual toll-like receptor 7 and toll-like receptor 8*
1171 *agonist protects against influenza in rats.* Antiviral Res, 2007. **73**(1): p. 1-11.
1172 10. Geeraedts, F., et al., *Superior immunogenicity of inactivated whole virus H5N1 influenza vaccine*
1173 *is primarily controlled by Toll-like receptor signalling.* PLoS Pathog, 2008. **4**(8): p. e1000138.
1174 11. Wang, J.P., et al., *Toll-like receptor-mediated activation of neutrophils by influenza A virus.* Blood,
1175 2008. **112**(5): p. 2028-34.
1176 12. Kawai, T. and S. Akira, *Toll-like receptors and their crosstalk with other innate receptors in infection*
1177 *and immunity.* Immunity, 2011. **34**(5): p. 637-50.
1178 13. Pulendran, B. and M.S. Maddur, *Innate immune sensing and response to influenza.* Curr Top
1179 Microbiol Immunol, 2015. **386**: p. 23-71.
1180 14. Wang, R., et al., *The transcription factor Myc controls metabolic reprogramming upon T*
1181 *lymphocyte activation.* Immunity, 2011. **35**(6): p. 871-82.
1182 15. Zeng, H., et al., *mTORC1 couples immune signals and metabolic programming to establish T(reg)-*
1183 *cell function.* Nature, 2013. **499**(7459): p. 485-90.
1184 16. Huang, S.C., et al., *Metabolic Reprogramming Mediated by the mTORC2-IRF4 Signaling Axis Is*
1185 *Essential for Macrophage Alternative Activation.* Immunity, 2016. **45**(4): p. 817-830.
1186 17. Everts, B., et al., *Commitment to glycolysis sustains survival of NO-producing inflammatory*
1187 *dendritic cells.* Blood, 2012. **120**(7): p. 1422-31.
1188 18. Everts, B., et al., *TLR-driven early glycolytic reprogramming via the kinases TBK1-IKKvarepsilon*
1189 *supports the anabolic demands of dendritic cell activation.* Nat Immunol, 2014. **15**(4): p. 323-32.
1190 19. Krawczyk, C.M., et al., *Toll-like receptor-induced changes in glycolytic metabolism regulate*
1191 *dendritic cell activation.* Blood, 2010. **115**(23): p. 4742-9.
1192 20. Hartmann, B.M., et al., *Mouse dendritic cell (DC) influenza virus infectivity is much lower than that*
1193 *for human DCs and is hemagglutinin subtype dependent.* J Virol, 2013. **87**(3): p. 1916-8.
1194 21. Ioannidis, L.J., et al., *Abortive replication of influenza virus in mouse dendritic cells.* J Virol, 2012.
1195 **86**(10): p. 5922-5.
1196 22. Bender, A., et al., *The distinctive features of influenza virus infection of dendritic cells.*
1197 Immunobiology, 1998. **198**(5): p. 552-67.

1198 23. Lopez-Ferrer, D., et al., *Evaluation of a high-intensity focused ultrasound-immobilized trypsin*
1199 *digestion and 18O-labeling method for quantitative proteomics.* Anal Chem, 2009. **81**(15): p. 6272-
1200 7.
1201 24. Dennis, G., Jr., et al., *DAVID: Database for Annotation, Visualization, and Integrated Discovery.*
1202 Genome Biol, 2003. **4**(5): p. P3.
1203 25. Tkach, J.M., et al., *Dissecting DNA damage response pathways by analysing protein localization*
1204 *and abundance changes during DNA replication stress.* Nature Cell Biology, 2012. **14**: p. 966.
1205 26. Wygrecka, M., et al., *Enolase-1 promotes plasminogen-mediated recruitment of monocytes to the*
1206 *acutely inflamed lung.* Blood, 2009. **113**(22): p. 5588-98.
1207 27. Walter, L. and G. Hajnoczky, *Mitochondria and endoplasmic reticulum: the lethal interorganelle*
1208 *cross-talk.* J Bioenerg Biomembr, 2005. **37**(3): p. 191-206.
1209 28. John, S., J.N. Weiss, and B. Ribalet, *Subcellular localization of hexokinases I and II directs the*
1210 *metabolic fate of glucose.* PLoS One, 2011. **6**(3): p. e17674.
1211 29. Hedbacker, K., R. Townley, and M. Carlson, *Cyclic AMP-Dependent Protein Kinase Regulates the*
1212 *Subcellular Localization of Snf1-Sip1 Protein Kinase.* Molecular and Cellular Biology, 2004. **24**(5):
1213 p. 1836-1843.
1214 30. Huttemann, M., et al., *Regulation of mitochondrial oxidative phosphorylation through cell*
1215 *signaling.* Biochim Biophys Acta, 2007. **1773**(12): p. 1701-20.
1216 31. Sancho, P., et al., *MYC/PGC-1alpha Balance Determines the Metabolic Phenotype and Plasticity of*
1217 *Pancreatic Cancer Stem Cells.* Cell Metab, 2015. **22**(4): p. 590-605.
1218 32. Shakery, A., et al., *Beta-Hydroxybutyrate Promotes Proliferation, Migration and Stemness in a*
1219 *Subpopulation of 5FU Treated SW480 Cells: Evidence for Metabolic Plasticity in Colon Cancer.*
1220 Asian Pac J Cancer Prev, 2018. **19**(11): p. 3287-3294.
1221 33. Prieto, J., et al., *MYC Induces a Hybrid Energetics Program Early in Cell Reprogramming.* Stem Cell
1222 Reports, 2018. **11**(6): p. 1479-1492.
1223 34. Phillips, R.M., et al., *Bittersweet tumor development and progression: Emerging roles of epithelial*
1224 *plasticity glycosylations.* Adv Cancer Res, 2019. **142**: p. 23-62.
1225 35. Simoes, R.V., et al., *Metabolic plasticity of metastatic breast cancer cells: adaptation to changes*
1226 *in the microenvironment.* Neoplasia, 2015. **17**(8): p. 671-84.
1227 36. Jia, D., et al., *Elucidating the Metabolic Plasticity of Cancer: Mitochondrial Reprogramming and*
1228 *Hybrid Metabolic States.* Cells, 2018. **7**(3).
1229 37. Rosenzweig, A., J. Blenis, and A.P. Gomes, *Beyond the Warburg Effect: How Do Cancer Cells*
1230 *Regulate One-Carbon Metabolism?* Front Cell Dev Biol, 2018. **6**: p. 90.
1231 38. Jia, D., et al., *Elucidating cancer metabolic plasticity by coupling gene regulation with metabolic*
1232 *pathways.* Proceedings of the National Academy of Sciences, 2019. **116**(9): p. 3909-3918.
1233 39. Ananieva, E.A., J.D. Powell, and S.M. Hutson, *Leucine Metabolism in T Cell Activation: mTOR*
1234 *Signaling and Beyond.* Adv Nutr, 2016. **7**(4): p. 798S-805S.
1235 40. Palmer, C.S., et al., *Glucose metabolism regulates T cell activation, differentiation, and functions.*
1236 Front Immunol, 2015. **6**: p. 1.
1237 41. Pearce, E.L., *Metabolism in T cell activation and differentiation.* Curr Opin Immunol, 2010. **22**(3):
1238 p. 314-20.
1239 42. Verbist, K.C., R. Wang, and D.R. Green, *T cell metabolism and the immune response.* Semin
1240 Immunol, 2012. **24**(6): p. 399-404.
1241 43. Aibibula, M., K.M. Naseem, and R.G. Sturmey, *Glucose metabolism and metabolic flexibility in*
1242 *blood platelets.* J Thromb Haemost, 2018. **16**(11): p. 2300-2314.
1243 44. Gao, Y., et al., *Lipoprotein Lipase Maintains Microglial Innate Immunity in Obesity.* Cell Rep, 2017.
1244 **20**(13): p. 3034-3042.

1245 45. Yao, C.H., et al., *Identifying off-target effects of etomoxir reveals that carnitine*
1246 *palmitoyltransferase I is essential for cancer cell proliferation independent of beta-oxidation.* PLoS
1247 Biol, 2018. **16**(3): p. e2003782.
1248 46. Legmann, R., et al., *Analysis of glycolytic flux as a rapid screen to identify low lactate producing*
1249 *CHO cell lines with desirable monoclonal antibody yield and glycan profile.* BMC Proc, 2011. **5**
1250 **Suppl 8**: p. P94.
1251 47. TeSlaa, T. and M.A. Teitell, *Techniques to monitor glycolysis.* Methods Enzymol, 2014. **542**: p. 91-
1252 114.
1253 48. Zhou, Y., et al., *Regulation of Na(+)/H(+) Exchanger in Dendritic Cells by Akt1.* Cell Physiol Biochem,
1254 2015. **36**(3): p. 1237-49.
1255 49. Thomas, D.C., *The phagocyte respiratory burst: Historical perspectives and recent advances.*
1256 Immunol Lett, 2017. **192**: p. 88-96.
1257 50. Sener, A., M.H. Giroix, and W.J. Malaisse, *Underestimation of D-glucose utilisation as judged from*
1258 *the conversion of D-[3-(3)H]glucose to (3)HOH.* Diabetologia, 2002. **45**(9): p. 1274-80.
1259 51. Bonnafous, P., et al., *Treatment of influenza virus with beta-propiolactone alters viral membrane*
1260 *fusion.* Biochim Biophys Acta, 2014. **1838**(1 Pt B): p. 355-63.
1261 52. Pawar, S.D., et al., *Evaluation of different inactivation methods for high and low pathogenic avian*
1262 *influenza viruses in egg-fluids for antigen preparation.* J Virol Methods, 2015. **222**: p. 28-33.
1263 53. Herrera-Rodriguez, J., et al., *Inactivated or damaged? Comparing the effect of inactivation*
1264 *methods on influenza virions to optimize vaccine production.* Vaccine, 2019. **37**(12): p. 1630-1637.
1265 54. Yepez, V.A., et al., *OCR-Stats: Robust estimation and statistical testing of mitochondrial respiration*
1266 *activities using Seahorse XF Analyzer.* PLoS One, 2018. **13**(7): p. e0199938.
1267 55. van der Windt, G.J., C.H. Chang, and E.L. Pearce, *Measuring Bioenergetics in T Cells Using a*
1268 *Seahorse Extracellular Flux Analyzer.* Curr Protoc Immunol, 2016. **113**: p. 3 16B 1-3 16B 14.
1269 56. Brand, M.D. and D.G. Nicholls, *Assessing mitochondrial dysfunction in cells.* Biochem J, 2011.
1270 **435**(2): p. 297-312.
1271 57. Brown, G.C. and V. Borutaite, *There is no evidence that mitochondria are the main source of*
1272 *reactive oxygen species in mammalian cells.* Mitochondrion, 2012. **12**(1): p. 1-4.
1273 58. Chacko, B.K., et al., *The Bioenergetic Health Index: a new concept in mitochondrial translational*
1274 *research.* Clin Sci (Lond), 2014. **127**(6): p. 367-73.
1275 59. Pearce, E.J. and B. Everts, *Dendritic cell metabolism.* Nat Rev Immunol, 2015. **15**(1): p. 18-29.
1276 60. Kelly, B. and L.A. O'Neill, *Metabolic reprogramming in macrophages and dendritic cells in innate*
1277 *immunity.* Cell Res, 2015. **25**(7): p. 771-84.
1278 61. O'Neill, L.A. and E.J. Pearce, *Immunometabolism governs dendritic cell and macrophage function.*
1279 J Exp Med, 2016. **213**(1): p. 15-23.
1280 62. Wculek, S.K., et al., *Metabolic Control of Dendritic Cell Functions: Digesting Information.* Front
1281 Immunol, 2019. **10**: p. 775.
1282 63. Wise, D.R., et al., *Myc regulates a transcriptional program that stimulates mitochondrial*
1283 *glutaminolysis and leads to glutamine addiction.* Proceedings of the National Academy of
1284 Sciences, 2008. **105**(48): p. 18782-18787.
1285 64. Goetzman, E.S. and E.V. Prochownik, *The Role for Myc in Coordinating Glycolysis, Oxidative*
1286 *Phosphorylation, Glutaminolysis, and Fatty Acid Metabolism in Normal and Neoplastic Tissues.*
1287 Front Endocrinol (Lausanne), 2018. **9**: p. 129.
1288 65. Gao, P., et al., *c-Myc suppression of miR-23a/b enhances mitochondrial glutaminase expression*
1289 *and glutamine metabolism.* Nature, 2009. **458**(7239): p. 762-5.
1290 66. Wise, D.R., et al., *Myc regulates a transcriptional program that stimulates mitochondrial*
1291 *glutaminolysis and leads to glutamine addiction.* Proc Natl Acad Sci U S A, 2008. **105**(48): p. 18782-
1292 7.

1293 67. Fan, Y., K.G. Dickman, and W.X. Zong, *Akt and c-Myc differentially activate cellular metabolic*
1294 *programs and prime cells to bioenergetic inhibition.* J Biol Chem, 2010. **285**(10): p. 7324-33.
1295 68. Gnanaprakasam, J.N. and R. Wang, *MYC in Regulating Immunity: Metabolism and Beyond.* Genes
1296 (Basel), 2017. **8**(3).
1297 69. Kc, W., et al., *L-Myc expression by dendritic cells is required for optimal T-cell priming.* Nature,
1298 2014. **507**(7491): p. 243-7.
1299 70. Dang, C.V., *c-myc target genes involved in cell growth, apoptosis, and metabolism.* Molecular and
1300 Cellular Biology, 1999. **19**(1): p. 1-11.
1301 71. Choi, Y.K. and K.G. Park, *Targeting Glutamine Metabolism for Cancer Treatment.* Biomol Ther
1302 (Seoul), 2018. **26**(1): p. 19-28.
1303 72. Dang, C.V., *MYC, microRNAs and glutamine addiction in cancers.* Cell Cycle, 2009. **8**(20): p. 3243-
1304 5.
1305 73. Lewis, B.C., et al., *Tumor induction by the c-Myc target genes rcl and lactate dehydrogenase A.*
1306 Cancer Res, 2000. **60**(21): p. 6178-83.
1307 74. Osthus, R.C., et al., *Deregulation of glucose transporter 1 and glycolytic gene expression by c-Myc.*
1308 J Biol Chem, 2000. **275**(29): p. 21797-800.
1309 75. Dang, C.V., et al., *The c-Myc target gene network.* Semin Cancer Biol, 2006. **16**(4): p. 253-64.
1310 76. Morrish, F., et al., *The oncogene c-Myc coordinates regulation of metabolic networks to enable*
1311 *rapid cell cycle entry.* Cell Cycle, 2008. **7**(8): p. 1054-66.
1312 77. Li, F., et al., *Myc stimulates nuclearly encoded mitochondrial genes and mitochondrial biogenesis.*
1313 Mol Cell Biol, 2005. **25**(14): p. 6225-34.
1314 78. Kim, J., J.H. Lee, and V.R. Iyer, *Global identification of Myc target genes reveals its direct role in*
1315 *mitochondrial biogenesis and its E-box usage in vivo.* PLoS One, 2008. **3**(3): p. e1798.
1316 79. Legge, K.L. and T.J. Braciale, *Accelerated migration of respiratory dendritic cells to the regional*
1317 *lymph nodes is limited to the early phase of pulmonary infection.* Immunity, 2003. **18**(2): p. 265-
1318 77.
1319 80. Yoon, H., et al., *Sequential activation of CD8+ T cells in the draining lymph nodes in response to*
1320 *pulmonary virus infection.* J Immunol, 2007. **179**(1): p. 391-9.
1321 81. Nonacs, R., et al., *Mechanisms of mouse spleen dendritic cell function in the generation of*
1322 *influenza-specific, cytolytic T lymphocytes.* J Exp Med, 1992. **176**(2): p. 519-29.
1323 82. Macatonia, S.E., et al., *Primary stimulation by dendritic cells induces antiviral proliferative and*
1324 *cytotoxic T cell responses in vitro.* J Exp Med, 1989. **169**(4): p. 1255-64.
1325 83. Bhardwaj, N., et al., *Influenza virus-infected dendritic cells stimulate strong proliferative and*
1326 *cytolytic responses from human CD8+ T cells.* J Clin Invest, 1994. **94**(2): p. 797-807.
1327 84. Gubser, P.M., et al., *Rapid effector function of memory CD8+ T cells requires an immediate-early*
1328 *glycolytic switch.* Nature Immunology, 2013. **14**: p. 1064.
1329 85. Menk, A.V., et al., *Early TCR Signaling Induces Rapid Aerobic Glycolysis Enabling Distinct Acute T*
1330 *Cell Effector Functions.* Cell reports, 2018. **22**(6): p. 1509-1521.
1331 86. Zhou, Y., et al., *Evidence for a direct link between PAD4-mediated citrullination and the oxidative*
1332 *burst in human neutrophils.* Scientific Reports, 2018. **8**(1): p. 15228.
1333 87. Guak, H., et al., *Glycolytic metabolism is essential for CCR7 oligomerization and dendritic cell*
1334 *migration.* Nature Communications, 2018. **9**(1): p. 2463.
1335 88. O'Connor, R.S., et al., *The CPT1a inhibitor, etomoxir induces severe oxidative stress at commonly*
1336 *used concentrations.* Scientific Reports, 2018. **8**(1): p. 6289.
1337 89. Jenkins, M.R., et al., *Addition of a prominent epitope affects influenza A virus-specific CD8+ T cell*
1338 *immunodominance hierarchies when antigen is limiting.* J Immunol, 2006. **177**(5): p. 2917-25.
1339 90. Schell, A.M., et al., *Dendritic cell migration limits the duration of CD8+ T-cell priming to peripheral*
1340 *viral antigen.* J Virol, 2010. **84**(7): p. 3586-94.

1341 91. Aldridge, J.R., Jr., et al., *TNF/iNOS-producing dendritic cells are the necessary evil of lethal*
1342 *influenza virus infection.* Proc Natl Acad Sci U S A, 2009. **106**(13): p. 5306-11.
1343 92. Russ, B.E., et al., *Distinct epigenetic signatures delineate transcriptional programs during virus-*
1344 *specific CD8(+) T cell differentiation.* Immunity, 2014. **41**(5): p. 853-65.
1345 93. Sanders, C.J., et al., *Compromised respiratory function in lethal influenza infection is characterized*
1346 *by the depletion of type I alveolar epithelial cells beyond threshold levels.* Am J Physiol Lung Cell
1347 Mol Physiol, 2013. **304**(7): p. L481-8.
1348 94. Oshansky, C.M. and P.G. Thomas, *The human side of influenza.* J Leukoc Biol, 2012. **92**(1): p. 83-
1349 96.
1350 95. Pearce, E.L., et al., *Enhancing CD8 T-cell memory by modulating fatty acid metabolism.* Nature,
1351 2009. **460**(7251): p. 103-7.
1352 96. Chang, C.H., et al., *Posttranscriptional control of T cell effector function by aerobic glycolysis.* Cell,
1353 2013. **153**(6): p. 1239-51.
1354 97. Sun, J., et al., *TLR ligands can activate dendritic cells to provide a MyD88-dependent negative*
1355 *signal for Th2 cell development.* J Immunol, 2005. **174**(2): p. 742-51.
1356 98. Haas, R., et al., *Lactate Regulates Metabolic and Pro-inflammatory Circuits in Control of T Cell*
1357 *Migration and Effector Functions.* PLoS Biol, 2015. **13**(7): p. e1002202.
1358 99. van Horssen, R., et al., *Modulation of cell motility by spatial repositioning of enzymatic ATP/ADP*
1359 *exchange capacity.* J Biol Chem, 2009. **284**(3): p. 1620-7.
1360 100. Vermaelen, K.Y., et al., *Specific migratory dendritic cells rapidly transport antigen from the airways*
1361 *to the thoracic lymph nodes.* J Exp Med, 2001. **193**(1): p. 51-60.
1362 101. Filipp, F.V., et al., *Glutamine-fueled mitochondrial metabolism is decoupled from glycolysis in*
1363 *melanoma.* Pigment Cell Melanoma Res, 2012. **25**(6): p. 732-9.
1364 102. Dong, H.J., et al., *The Wnt/beta-catenin signaling/Id2 cascade mediates the effects of hypoxia on*
1365 *the hierarchy of colorectal-cancer stem cells.* Sci Rep, 2016. **6**: p. 22966.
1366 103. Davis, A.C., et al., *A null c-myc mutation causes lethality before 10.5 days of gestation in*
1367 *homozygotes and reduced fertility in heterozygous female mice.* Genes Dev, 1993. **7**(4): p. 671-82.
1368 104. Nicklin, P., et al., *Bidirectional transport of amino acids regulates mTOR and autophagy.* Cell, 2009.
1369 **136**(3): p. 521-34.
1370 105. DeBerardinis, R.J., et al., *Beyond aerobic glycolysis: transformed cells can engage in glutamine*
1371 *metabolism that exceeds the requirement for protein and nucleotide synthesis.* Proc Natl Acad Sci
1372 U S A, 2007. **104**(49): p. 19345-50.
1373 106. Eilers, M. and R.N. Eisenman, *Myc's broad reach.* Genes Dev, 2008. **22**(20): p. 2755-66.
1374 107. Bush, A., et al., *c-myc null cells misregulate cad and gadd45 but not other proposed c-Myc targets.*
1375 Genes Dev, 1998. **12**(24): p. 3797-802.
1376 108. Graves, L.M., et al., *Regulation of carbamoyl phosphate synthetase by MAP kinase.* Nature, 2000.
1377 **403**(6767): p. 328-32.
1378 109. Yuneva, M., et al., *Deficiency in glutamine but not glucose induces MYC-dependent apoptosis in*
1379 *human cells.* J Cell Biol, 2007. **178**(1): p. 93-105.
1380 110. Altman, B.J., Z.E. Stine, and C.V. Dang, *From Krebs to clinic: glutamine metabolism to cancer*
1381 *therapy.* Nat Rev Cancer, 2016. **16**(10): p. 619-34.
1382 111. Goto, M., et al., *Importance of glutamine metabolism in leukemia cells by energy production*
1383 *through TCA cycle and by redox homeostasis.* Cancer Invest, 2014. **32**(6): p. 241-7.
1384 112. Gardner, P.R., et al., *Superoxide radical and iron modulate aconitase activity in mammalian cells.*
1385 J Biol Chem, 1995. **270**(22): p. 13399-405.
1386 113. Yoo, H., et al., *Quantifying reductive carboxylation flux of glutamine to lipid in a brown adipocyte*
1387 *cell line.* J Biol Chem, 2008. **283**(30): p. 20621-7.

1388 114. Jiang, L., et al., *Reductive carboxylation supports redox homeostasis during anchorage-*
1389 *independent growth.* Nature, 2016. **532**(7598): p. 255-8.
1390 115. Zorov, D.B., M. Juhaszova, and S.J. Sollott, *Mitochondrial reactive oxygen species (ROS) and ROS-*
1391 *induced ROS release.* Physiol Rev, 2014. **94**(3): p. 909-50.
1392 116. Lindsay, D.P., et al., *Differential effects of buffer pH on Ca(2+)-induced ROS emission with inhibited*
1393 *mitochondrial complexes I and III.* Front Physiol, 2015. **6**: p. 58.
1394 117. Swamy, M., et al., *Glucose and glutamine fuel protein O-GlcNAcylation to control T cell self-*
1395 *renewal and malignancy.* Nat Immunol, 2016. **17**(6): p. 712-20.
1396 118. Langenkamp, A., et al., *T cell priming by dendritic cells: thresholds for proliferation, differentiation*
1397 *and death and intraclonal functional diversification.* Eur J Immunol, 2002. **32**(7): p. 2046-54.
1398 119. Kilbourne, E.D., *Future influenza vaccines and the use of genetic recombinants.* Bull World Health
1399 Organ, 1969. **41**(3): p. 643-5.
1400 120. Reed LJ, M.H., *A simple method of estimating fifty per cent endpoints. .* American Journal of
1401 Epidemiology, 1938. **27**(3): p. 493–497.
1402 121. Shannon, P., et al., *Cytoscape: a software environment for integrated models of biomolecular*
1403 *interaction networks.* Genome Res, 2003. **13**(11): p. 2498-504.
1404 122. Antonov, A.V., et al., *PPI spider: A tool for the interpretation of proteomics data in the context of*
1405 *protein–protein interaction networks.* PROTEOMICS, 2009. **9**(10): p. 2740-2749.
1406 123. Hue, L., F. Sobrino, and L. Bosca, *Difference in glucose sensitivity of liver glycolysis and glycogen*
1407 *synthesis. Relationship between lactate production and fructose 2,6-bisphosphate concentration.*
1408 Biochem J, 1984. **224**(3): p. 779-86.
1409 124. Moon, A. and W.J. Rhead, *Complementation analysis of fatty acid oxidation disorders.* J Clin Invest,
1410 1987. **79**(1): p. 59-64.
1411 125. Brand, K., J.F. Williams, and M.J. Weidemann, *Glucose and glutamine metabolism in rat*
1412 *thymocytes.* Biochem J, 1984. **221**(2): p. 471-5.
1413 126. Willems, H.L., et al., *Determination of pyruvate oxidation rate and citric acid cycle activity in intact*
1414 *human leukocytes and fibroblasts.* Clin Chem, 1978. **24**(2): p. 200-3.
1415 127. Katz, J. and H.G. Wood, *The use of C14O2 yields from glucose-1- and -6-C14 for the evaluation of*
1416 *the pathways of glucose metabolism.* J Biol Chem, 1963. **238**: p. 517-23.
1417 128. Neumayer, H.P., et al., *Importance of ICAM-1 for accessory cell function of monocytic cells.*
1418 Immunobiology, 1990. **180**(4-5): p. 458-66.
1419 129. Livak, K.J. and T.D. Schmittgen, *Analysis of relative gene expression data using real-time*
1420 *quantitative PCR and the 2(-Delta Delta C(T)) Method.* Methods, 2001. **25**(4): p. 402-8.

1421 # Supporting information

1422 ## Supplemental Figure Legends

1423 **S1 Fig. Validation and experimental design of proteomics for IAV infected DC.** DC were left
1424 untreated (Ctl) or infected for 17 hours at MOI 5 with viable virus (IAV). (A) DC were also infected
1425 for 17 hours at MOI 5 with β-propiolactone inactivated virus (IAV^{BPL}). DC were fixed and stained
1426 for DAPI, influenza nuclear protein or murine α-enolase protein and visualized with confocal
1427 microscopy. (B) Control uninfected cells or IAV infected BMDC (MOI 5 pfu for 17 hours) were
1428 separated into soluble and insoluble fractions. The iTRAQ labeled samples were subjected to
1429 FASP digestion while the SIL samples received trypsin-catalyzed $^{18}O/^{16}O$ labeling. The samples
1430 were desalted with C18 SPE, processed with a custom RPLC system and analyzed with a Velos
1431 Orbitrap mass spectrometer (iTRAQ) or LTQ-Orbitrap (SIL). (C) Venn-diagram depicting the
1432 distinct total number of proteins identified by iTRAQ and SIL, as well as the overlapping number

of proteins. Venn-diagram illustrating the statistically significant number of proteins identified by iTRAQ and SIDL in soluble and insoluble fractions which were up and down regulated as well as the overlapping number of proteins. (D) Both soluble and insoluble SIL DC proteomes were submitted to DAVID and PPI spider to define glycolytic protein-protein interaction networks. The glycolytic network was put into Cytoscape and integrated with quantitative data from the proteomic analysis. Alpha enolase increased in soluble and insoluble (inset) proteomes and was validated with immunoblotting revealing the monomer and dimer increased in both soluble (S) and insoluble (I) networks.

S2 Fig. DC metabolic adaptation to fuel respiration following IAV infection. DC were left untreated (Ctl), infected for 17 hours at MOI 5 with viable virus (IAV). (A-D) The rates of pyruvate, glutamine, or long chain fatty acids oxidation for respiration were calculated as the percentage of inhibition of oxygen consumption by UK5099, BPTES, or Etomoxir specific inhibitors of mitochondrial pyruvate carrier, glutaminase, and carnitine palmitoyl-transferase 1A. Capacity for a specific substrate to drive respiratory OCR was tested by determining baseline OCR then inhibiting the 2 off target substrates determining OCR then inhibiting import of the target metabolite. Percent capacity is one minus the baseline OCR less the off-target OCR divided by the baseline OCR less the OCR after all targets inhibited times 100. Dependency on a specific substrate was tested as above reversing the inhibitor sequence and the percent dependence was calculated by deducting the target OCR from the baseline and dividing by the baseline OCR less the OCR after all targets inhibited times 100. Fuel Flexibility was calculated as the difference between Capacity and Dependency. The average capacity of uninfected or infected DC to use either pyruvate, glutamine, or long chain fatty acids was determined. The average dependence of uninfected or infected DC on the oxidation of either pyruvate, glutamine, or long chain fatty acids was determined. The average flexibility of DC to use either pyruvate, glutamine, or long chain fatty acids was determined for uninfected or infected. (E-F) DC were pretreated with UK5099, Etomoxir (ETO), or BPTES +/- IAV for 17 hours, rinsed and lysed for quantification of intracellular glutamine (E) or α-ketoglutarate activity (F). The bar graphs represent the values of 4-5 independent experiments and presented as experimental mean +/- SD p-value <0.05 (*), p-value < 0.01 (**), and p-value < 0.0001 (****). B-D show one representative experiment of 5 independent experiments with corresponding capacity, dependence, and flexibility values inset.

S3 Fig. Confidence intervals and mean differences of bioenergetics comparing TLR agonists and IAV. (A-D) DC were infected or treated with TLA agonists lipopolysaccharide (LPS), polyinosinic polycytidylic acid (PolyIC), or Resiquimod (R848) for 17 hours followed by metabolic analysis with Seahorse Xfe96 Flux Analyzer. (A) Glycolytic function was tested while monitoring extracellular acidification rate (ECAR) with sequential injections of glucose, oligomycin (Oligo), and 2-Deoxy-D-glucose (2-DG) indicated by arrows. (B) Glucose uptake was monitored from the medium using a standard blood glucometer with glucose standard calibration curves. (C) Mitochondrial respiration was tested while monitoring oxygen consumption rates (OCR) with sequential injections of oligomycin (Oligo), carbonyl cyanide-p-trifluoromethoxyphenylhydrazone (FCCP), and a mixture of rotenone and antimycin A (Rot/AntA) indicated by arrows. (D) DC maximal mitochondrial ATP changes induced by oligomycin plotted against maximal ATP changes upon glucose depletion determined by respirometry using Xfe96. The graphs represent the difference of the mean values from 3-4 independent experiments measured (3 ≥ technical replicates) and 95% confidence intervals. Statistical differences among means was found with ANOVA followed by Tukey, validated with Dunnett's multiple comparison tests. Dashed line appears at 1 and red circles indicate confidence intervals do not overlap.

S4 Fig. Live to dead ration of DC in response to infection or TLR agonists with metabolite restriction. (A&B) DC were infected with CA04 or X31 influenza virus (MOI = 5) for 17 hours

1484 followed by metabolic analysis with Seahorse Xfe96 Flux Analyzer. (A) Glycolytic function was
1485 tested while monitoring extracellular acidification rate (ECAR) with sequential injections of
1486 glucose, oligomycin (Oligo), and 2-Deoxy-D-glucose (2-DG) indicated by arrows. (B)
1487 Mitochondrial respiration was tested while monitoring oxygen consumption rates (OCR) with
1488 sequential injections of oligomycin (Oligo), carbonyl cyanide-p-trifluoromethoxyphenylhydrazone
1489 (FCCP), and a mixture of rotenone and antimycin A (Rot/AntA) indicated by arrows. The bar
1490 graphs represent mean and error bars standard deviation. Statistical differences among means
1491 was found with ANOVA followed by Tukey's Honest Significant Difference (Tukey's HSD) method.
1492 The difference of the means are plotted with Tukey's HSD 95% confidence intervals. The red
1493 circles indicate confidence intervals do not overlap. Tukey adjusted p values are symbolized by
1494 asterisks indicating adjusted p-values (* $p \leq 0.05$, ** $p \leq 0.001$, *** $p \leq 0.0001$, and **** $p < 0.0001$). (C)
1495 DC growth medium was replaced with deplete medium 3 hours prior to infection or agonist
1496 treatment in blank or viral laden infection medium (MOI = 5) for 2 hours followed by a return to
1497 deplete medium for 17 hours. Viable, dead, and total DC were stained with calcein AM, ethidium
1498 homodimer and DAPI, respectively, and measured fluorescence intensity using a microplate
1499 reader. Then mean fluorescence intensities (MFI) and the ratio of live to dead DC were calculated.
1500 The graphs represent the mean values of 3 independent experiments measured +/- SD. Statistical
1501 differences among means was found with ANOVA followed by Tukey's HSD and results
1502 summarized using with compact letter display such that groups that are detectably different get
1503 different letters.
1504
1505 **S5 Fig. Limiting glycolysis or mitochondrial oxidation of pyruvate, glutamine or long chain**
1506 **fatty acids impairs infected DC function.** (A) DC were seeded on precoated Oris™ 96-well
1507 migration plate allowed to adhere 18+ hours followed by plug removal and infection (MOI = 5) for
1508 17 hours. Live cells were stained with CalcienAM and images acquired with EVOS, two
1509 representative microscopy images of control and IAV migration are presented. (B) DC were left
1510 untreated (Ctl) or pretreated with cMyc (2 μM), BPTES (3 μM) and UK5099 (2 μM) and etomoxir
1511 (4 μM) respectively, infected for 17 hours (MOI = 5) with IAV. 1mg/ml FITC-Dextran 40S was
1512 added and phagocytosis was terminated after 1 hour at 37°C and 4°C then fluorescence per cell
1513 was measured using flow cytometry (C-F) CD8+ T cells were isolated by negative depletion from
1514 fresh splenocytes of homologous primed female C57BL/6 mice and co-cultured with DC at 5:1
1515 ratio T cells to DC for 24 hours. Cells were fixed and stained for surface markers then quantified
1516 and compensated for using FlowJo software (2 other independent experiments were performed
1517 on different instruments and quantified/compensated using different software produced similar
1518 trends but were excluded due to compensation methods differences). (C) Representative FACS
1519 plots with gating strategy. (D) Bar graphs represent the mean values of 2 independent
1520 experiments +/- SD. Statistical differences among means was found with ANOVA followed by
1521 Tukey's HSD with asterisks indicating adjusted p-values (* $p \leq 0.05$, ** $p \leq 0.001$, *** $p \leq 0.0001$, and
1522 **** $p < 0.0001$). (E) Tukey's HSD results summarized with the circles representing the mean
1523 difference and the error bars the 95% confidence intervals. (F) Tukey's HSD results to from Figure
1524 5D are summarized with the circles representing the mean difference and the error bars the 95%
1525 confidence intervals corresponding.
1526
1527 **S6 Fig. Unsupervised multivariant principal component analysis (PCA) of Tip DC and**
1528 **volcano plot of transcripts.** At zero or nine days following intranasal infection of mice with IAV
1529 at (EID_{50}: 2000) the lungs were homogenized and cells extracted. Cells were antibody stained for
1530 TipDC surface markers CD11b, Ly6c, GR-1, and MHCII. TipDC controls (Ctl) from day 0 were
1531 sorted based on high levels of CD11b, Ly6c, and GR-1. TipDC from day 9 of the IAV infection
1532 (IAV) were sorted based on high levels of CD11b, Ly6c, GR-1, and MHCII. cDNA libraries were
1533 generated from RNA, sequenced, and narrowed to confidentially identified transcripts. (A)
1534 Unsupervised multivariant principal component analysis (PCA) resulting in F1 and F2 with a

1535 cumulative percent variability of 78.56% Each circle represents a TipDC transcriptome, the open
1536 circles are control and the solid black IAV. (B) Differential expression differences were determined
1537 using Tukey HSD test for multiple comparisons with a Benjamini-Hochberg post-hoc false
1538 discover rate correction. 6642 transcripts were removed with nonspecific filtering to remove
1539 transcripts that were not modulated by IAV (i.e. 50% standard deviation threshold). Log10 p-
1540 values are plotted against the Log2 ratio
1541
1542
1543
1544

1545 **Supplemental File Legends**

1546 **S1 File. Significantly enriched KEGG pathways altered by influenza infection of DC.**
1547 Approximately 25 000 peptides were detected with corresponding reporter ions (available in the
1548 PRIDE repository). (A) 7520 confidentially identified peptides from the stable isotopically labeled
1549 (SIL) and isobaric tagged (iTRAQ) proteomes and mapped to National Center for Biotechnology
1550 Information (NCBI) reference sequence accession numbers. (B&C) Confidently identified protein
1551 identifiers from the soluble and insoluble fractions were segregated into up regulated (B) or down
1552 regulated (C) based on 2-fold or greater abundances changes and submitted to DAVID for KEGG
1553 pathway analysis. Significantly enriched KEGG pathways are listed and gene symbols associated
1554 to NCBI accession numbers provided along with corresponding KEGG class and subclass from
1555 the BRITE hierarchy (colored circles correspond to subclasses from figure 1).

1556 **S2 File. TipDC transcriptome.** At zero or nine days following intranasal infection of mice with
1557 IAV at (EID_{50}: 2000) the lungs were homogenized and cells extracted. Cells were antibody stained
1558 for TipDC surface markers CD11b, Ly6c, GR-1, and MHCII. TipDC controls (Ctl) from day 0 were
1559 sorted based on high levels of CD11b, Ly6c, and GR-1. TipDC from day 9 of the IAV infection
1560 (IAV) were sorted based on high levels of CD11b, Ly6c, GR-1, and MHCII. cDNA libraries were
1561 generated from RNA, sequenced, and narrowed to confidentially identified transcripts. (A)
1562 Unsupervised multivariant principal component analysis (PCA) resulting in F1 and F2 with a
1563 cumulative percent variability of 78.56% Each circle represents a TipDC transcriptome, the open
1564 circles are control and the solid black IAV. (B) Differential expression differences were determined
1565 using Tukey HSD test for multiple comparisons with a Benjamini-Hochberg post-hoc false
1566 discover rate correction. (C) Transcripts that increased following IAV infection were submitted to
1567 DAVID and significantly enriched KEGG pathways are listed with corresponding KEGG class and
1568 subclass from the BRITE hierarchy. (D) Transcripts from the KEGG metabolic classes were
1569 submitted to DAVID and significantly enriched metabolic pathways are listed. (E) Transcripts that
1570 decreased following IAV infection were submitted to DAVID and significantly enriched KEGG
1571 pathways are listed with corresponding KEGG class and subclass from the BRITE hierarchy. (F)
1572 Unique transcripts from the Immune Pathway and Influenza A pathway were differentially
1573 expressed and corresponding protein names are listed under their functional category. (G) Gene
1574 symbols of the metabolic transcripts from TipDC and proteins from the in vitro differentiated DC
1575 are listed per pathway with the counts per cell type by down regulated (Down) or up regulate (Up)
1576 following IAV infection.
1577
1578

1579 **Figure legends**

1580 **Figure 1. Infection induced changes in DC protein abundance and localization.** Influenza
1581 virus strain A/PuertoRico/34 (IAV) was added to DC for 2 hours to allow entry, then medium
1582 replaced, and the infection proceeded for 17 hours followed by cell lysis and protein extraction.
1583 Proteins were labeled with either SIL or iTRAQ subjected to LC-MS/MS. Both proteomes were
1584 combined, redundancies removed and confidently identified peptides with abundance changes of
1585 2-fold or greater linked to protein identifiers. The lists of upregulated and downregulated proteins
1586 were submitted to the Database for Annotation, Visualization, and Integrated Discovery (DAVID)
1587 v6.7 and mapped to KEGG pathways. (A-B**)** Significantly enriched KEGG pathways were grouped
1588 by KEGG Orthology (KO) Class for the increased (A) and decreased (B) proteomes. (C**)** In the
1589 network summary of metabolic protein dynamics, the soluble and insoluble proteomes were
1590 subdivided by abundance change. Proteins with relative expression changes of two-fold or greater
1591 are connected to their location in the soluble or insoluble fraction by red (top) or blue (bottom)
1592 edges indicating increased or decreased abundance change, respectively. Each protein node
1593 size was held static and color coded by KEGG subclass with the corresponding metabolic
1594 pathway the protein mapped to delineated in the legend. The nodes of each KEGG subclass were
1595 arranged into circles that are proportional to the number of proteins with abundance changes in
1596 each significantly enriched metabolic pathway.
1597

1598 **Figure 2. Metabolic changes in infected DC**. DC were infected at MOI of 1 for 17 hours. (A-E)
1599 Use of isotopically labeled substrates, as indicated on the y axis, were used to monitor the
1600 generation of traceable products ($^{3}H_2O$ or $^{14}CO_2$) two hours after DC treatments substrates were
1601 quenched and allowed to accumulate overnight. Substrates were indicative of the following
1602 metabolic pathways: (A) [3-^{3}H]glucose (glycolysis), (B) [1-^{14}C]glucose (pentose phosphate
1603 pathway), (C) [2-^{14}C]pyruvate (TCA cycle), (D) [U-^{14}C]glutamine (glutaminolysis), and (E) [9,10-
1604 ^{3}H]palmitic acid (fatty acid oxidation). (F) The concentration of fatty acids (≥C8) in DC was
1605 determined by a coupled enzyme assay releasing fluorometric product proportional to the fatty
1606 acids present and quantifiable with standards after treatments. (G-I) The rates of pyruvate,
1607 glutamine, or long chain fatty acids oxidation for respiration were calculated as the percentage of
1608 inhibition of oxygen consumption by UK5099, BPTES, or Etomoxir specific inhibitors of
1609 mitochondrial pyruvate carrier, glutaminase, and carnitine palmitoyl-transferase 1A. Capacity for
1610 a specific substrate to drive respiratory OCR was tested by determining baseline OCR then
1611 inhibiting the 2 off target substrates determining OCR then inhibiting import of the target
1612 metabolite. Percent capacity is one minus the baseline OCR less the off-target OCR divided by
1613 the baseline OCR less the OCR after all targets inhibited times 100. Dependency on a specific
1614 substrate was tested as above reversing the inhibitor sequence and the percent dependence was
1615 calculated by deducting the target OCR from the baseline and dividing by the baseline OCR less
1616 the OCR after all targets inhibited times 100. Fuel Flexibility was calculated as the difference
1617 between Capacity and Dependency. (G) The average capacity of uninfected or infected DC to
1618 use pyruvate, glutamine, or long chain fatty acids was determined. (H) The average dependence
1619 of uninfected or infected DC on the oxidation of pyruvate, glutamine, or long chain fatty acids was
1620 determined. I) The average flexibility of DC to alternate oxidation of pyruvate, glutamine, or long
1621 chain fatty acids was determined for uninfected or infected. The graphs represent the values of
1622 two (E&F), three (B-D), or four (A, G-I) independent experiments measured (3 ≥ technical
1623 replicates) and presented as experimental mean +/- SD. Normality of these data were tested
1624 followed by the appropriate parametric (t-test) or nonparametric (Wilcoxon signed rank test) for
1625 normal distributions (A, B, E-H)) or not normal distributions (C,D,I), respectively. Asterisks
1626 correspond to p-values <0.05 (*) and a p-value < 0.01 (**).
1627

1628 **Figure 3. IAV infection induces distinct bioenergetics compared to TLR agonists primarily**
1629 **through aerobic glycolysis.** (A-D) DC were infected or treated with TLA agonists
1630 lipopolysaccharide (LPS), polyinosinic polycytidylic acid (PolyIC), or Resiquimod (R848) for 17
1631 hours followed by metabolic analysis with Seahorse Xfe96 Flux Analyzer. (A) Glycolytic function
1632 was tested with the Glycolysis Stress Test while monitoring real-time extracellular acidification
1633 rate (ECAR) with the Xfe96 metabolic analyzer during sequential injections of glucose, oligomycin
1634 (Oligo), and 2-Deoxy-D-glucose (2-DG) indicated by arrows. (B) Glucose uptake was monitored
1635 from the medium using a standard blood glucometer with glucose standard calibration curves. (C)
1636 Mitochondrial respiration was tested with the Mitochondrial Stress Test while monitoring oxygen
1637 consumption rates (OCR) in real-time with the Xfe96 metabolic analyzer during sequential
1638 injections of oligomycin (Oligo), carbonyl cyanide-p-trifluoromethoxyphenylhydrazone (FCCP),
1639 and a mixture of rotenone and antimycin A (Rot/AntA) indicated by arrows. (D) DC maximal
1640 mitochondrial ATP changes induced by oligomycin plotted against maximal ATP changes upon
1641 glucose depletion determined by respirometry using Xfe96. Each dataset represents the mean of
1642 3 experiments +/- SD for bar graphs or +/- SEM for energetic traces. Statistical differences among
1643 means was found with ANOVA followed by Tukey and validated with Dunnett's multiple
1644 comparison tests. Tukey test derived p values are symbolized by asterisks indicating adjusted p-
1645 values (* $p \leq 0.05$, ** $p \leq 0.001$, *** $p \leq 0.0001$, and **** $p < 0.0001$).
1646

1647 **Figure 4. c-Myc inhibition blocks IAV induced glycolysis.** (A) Up to 17 hours PI qPCR and
1648 immunoblotting of RNA and lysates were performed and quantification of target gene expression
1649 normalized to βeta actin using the 2−ΔΔCt method. One representative blot is presented in inset.
1650 (B-E) DCs were seeded in Seahorse XFe-96 plates and pretreated with 2 μM cMyc inhibitor (MI)
1651 for 4 hours then IAV infected for 17 hours. (B-C) Glycolytic function was tested with the Glycolysis
1652 Stress Test while monitoring real-time extracellular acidification rate (ECAR) with the Xfe96
1653 metabolic analyzer during sequential injections of glucose, oligomycin (Oligo), and 2-Deoxy-D-
1654 glucose (2-DG). Data represent means ± SD of 4 experiments. (D-E) Mitochondrial respiration
1655 was tested with the Mitochondrial Stress Test while monitoring oxygen consumption rates (OCR)
1656 in real-time with the Xfe96 metabolic analyzer during sequential injections of oligomycin (Oligo),
1657 carbonyl cyanide-p-trifluoromethoxyphenylhydrazone (FCCP), and a mixture of rotenone and
1658 antimycin A (Rot/AntA). These graphs represent the mean values of 3-4 independent experiments
1659 +/- SD. Statistical differences among means wese found with ANOVA followed by Tukey's multiple
1660 comparisons test with asterisks indicating adjusted p-values (* $p \leq 0.05$, ** $p \leq 0.001$, *** $p \leq 0.0001$,
1661 and **** $p < 0.0001$).
1662
1663

1664 **Figure 5. Limiting glycolysis or mitochondrial oxidation of pyruvate, glutamine or long**
1665 **chain fatty acids impairs infected DC function.** (A) DC were seeded on precoated Oris™ 96-
1666 well migration plate allowed to adhere 18+ hours followed by 4 hours of inhibitor treatment (2uM
1667 c-Myc inhibitor, 3uM BPTES, 4uM etomoxir or 2uM UK5099) plug removal and infection (MOI =
1668 5) for 17 hours. Cells were stained with calcein AM (2μM), viability and migration were determined
1669 with fluorescence at 485/528nm). The graph represents the mean values of 3 experiments +/-
1670 SD. (B-C) CD8+ T cells were isolated by negative depletion from fresh splenocytes of female
1671 C57BL/6 mice and co-cultured with DC at 5:1 ratio T cells to DC for 24 hours. Basal ECAR was
1672 established and T cell activation by anti-CD3/CD28-coated DynaBeads was monitored for 2 hours
1673 and maximal ECAR determined. (B) One representative graph is shown from 3 independent
1674 experiments. (C) The graph represents the mean values of 3 experiments +/- SD. (D) CD8+ T
1675 cells were isolated by negative depletion from fresh splenocytes derived from C57BL/6-
1676 Tg(TcraTcrb)1100Mjb/J (OT1) and co-cultured with DC at 5:1 ratio of T cells to DC for 24 hours.
1677 T cell were then stained for CD8, CD45.1, CD25, and CD44 and enumerated with flow cytometry.
1678 We selected CD8 and CD45.1 positive and then gated on CD25 and CD44. The graph represent
1679 the mean values of 2 experiments +/- SD. Statistical differences among means was found with
1680 ANOVA followed by Tukey's multiple comparisons test with asterisks indicating adjusted p-values
1681 (* $p \leq 0.05$, ** $p \leq 0.001$, *** $p \leq 0.0001$, and **** $p < 0.0001$).
1682

1683 **Figure 6. TipDC reprogram metabolism after accumulating in the lungs of IAV infected**
1684 **mice**. At zero or nine days following intranasal infection of mice with IAV (PR8) lungs were
1685 homogenized and cells extracted. Cells were antibody stained for TipDC surface markers CD11b,
1686 Ly6c, GR-1, and MHCII. TipDC controls (Ctl) from day 0 were sorted based on high levels of
1687 CD11b, Ly6c, and GR-1. TipDC from day 9 of the IAV infection (IAV) were sorted based on high
1688 levels of CD11b, Ly6c, GR-1, and MHCII. cDNA libraries were generated from RNA and
1689 sequenced. (A) Confidentially identified transcripts were k-means clustered followed by
1690 ascendant hierarchical clustering and genes with standard deviation threshold < 50% were
1691 removed. The data values were replaced by corresponding color intensities of blue to red through
1692 white based on interquartile range. (B-D) Significance in gene expression differences were
1693 determined using Tukey honest significant difference test for multiple comparisons with a
1694 Benjamini-Hochberg post-hoc false discover rate correction. TipDC genes that were either
1695 upregulated (red) or downregulated (blue) following IAV infection were mapped to KEGG
1696 pathways and significantly enriched pathways identified and sorted by KEGG Class (B-C). All
1697 isoforms of the central enzymes in glycolysis from the TipDC transcriptome are presented and
1698 colored including those that were unchanged (gray).
1699
1700

1701 **Figure 7. Dendritic cells globally reprogram metabolism in response to IAV infection.**
1702 Proteins were extracted from *in vitro* differentiated uninfected and infected DC, separated into
1703 insoluble and soluble fractions and subjected to mass spectrometry. RNA was extracted from
1704 lung TipDC on day 0 or 9 of IAV infection and subjected to RNA-Seq. The log2 ratio (IAV/Ctl) of
1705 transcripts and peptides were determined. Identifiers were converted to gene symbols and
1706 official protein names, each dataset were manually searched for all NCBI listed genes and
1707 synonyms corresponding to the major regulatory enzymes of glycolysis, pyruvate metabolism,
1708 and TCA cycle. (A) All isoforms of each enzyme were grouped (y-axis) and log2 ratios plotted.
1709 (B) Transcripts were grouped into glycolysis, pyruvate metabolism, and TCA cycle. (C) Peptides
1710 of enzymes were grouped into glycolysis, pyruvate metabolism, and TCA cycle.
1711
1712
1713
1714

1715 **Graphical abstract. Schematic of global metabolic changes in IAV infected DC.** Arrows
1716 indicate flow of metabolic products. Bar graph represents the percent difference between control
1717 uninfected and infected DC for experiments detailed in Figs 2 & 3 +/- SD.
1718

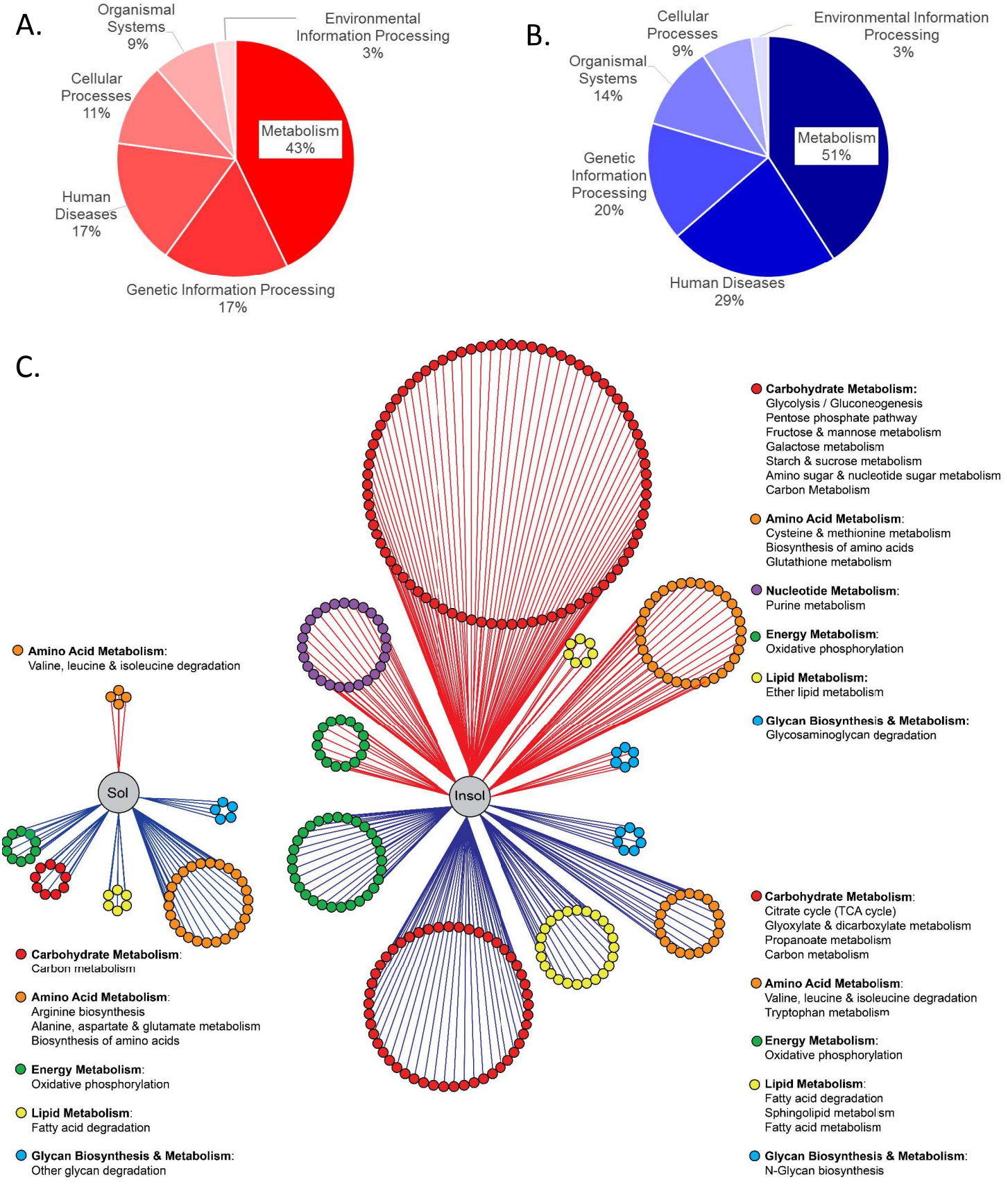
A.
Organismal Systems 9%
Environmental Information Processing 3%
Cellular Processes 11%
Metabolism 43%
Human Diseases 17%
Genetic Information Processing 17%
B.
Cellular Processes 9%
Environmental Information Processing 3%
Organismal Systems 14%
Metabolism 51%
Genetic Information Processing 20%
Human Diseases 29%
C.
Carbohydrate Metabolism:
Glycolysis / Gluconeogenesis
Pentose phosphate pathway
Fructose & mannose metabolism
Galactose metabolism
Starch & sucrose metabolism
Amino sugar & nucleotide sugar metabolism
Carbon Metabolism
Amino Acid Metabolism:
Cysteine & methionine metabolism
Biosynthesis of amino acids
Glutathione metabolism
Nucleotide Metabolism:
Purine metabolism
Energy Metabolism:
Oxidative phosphorylation
Lipid Metabolism:
Ether lipid metabolism
Glycan Biosynthesis & Metabolism:
Glycosaminoglycan degradation
Amino Acid Metabolism:
Valine, leucine & isoleucine degradation
Sol
Insol
Carbohydrate Metabolism:
Carbon metabolism
Amino Acid Metabolism:
Arginine biosynthesis
Alanine, aspartate & glutamate metabolism
Biosynthesis of amino acids
Energy Metabolism:
Oxidative phosphorylation
Lipid Metabolism:
Fatty acid degradation
Glycan Biosynthesis & Metabolism:
Other glycan degradation
Carbohydrate Metabolism:
Citrate cycle (TCA cycle)
Glyoxylate & dicarboxylate metabolism
Propanoate metabolism
Carbon metabolism
Amino Acid Metabolism:
Valine, leucine & isoleucine degradation
Tryptophan metabolism
Energy Metabolism:
Oxidative phosphorylation
Lipid Metabolism:
Fatty acid degradation
Sphingolipid metabolism
Fatty acid metabolism
Glycan Biosynthesis & Metabolism:
N-Glycan biosynthesis

Figure 1

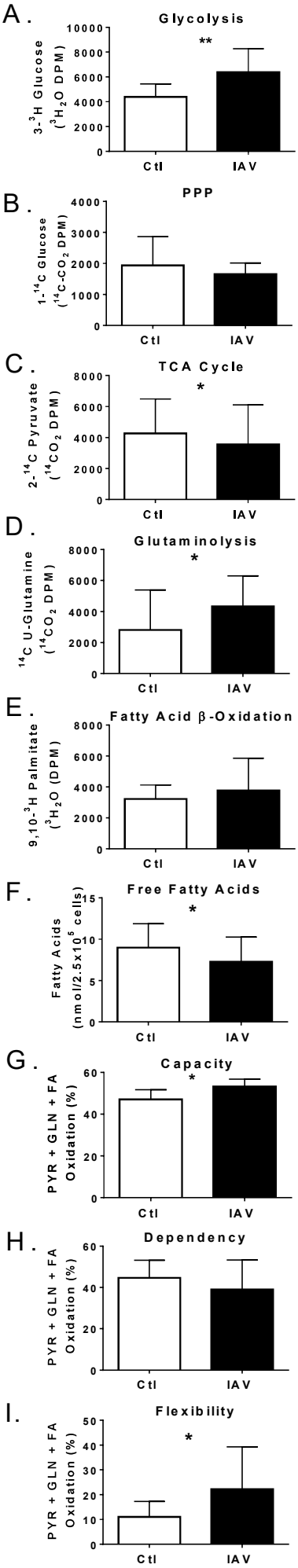
A.
Glycolysis
3-^{3}H Glucose (^3H_2O DPM)
10000
8000
6000
4000
2000
0
**
Ctl
IAV
B.
PPP
1-^{14}C Glucose (^{14}C-CO_2 DPM)
4000
3000
2000
1000
0
Ctl
IAV
C.
TCA Cycle
2-^{14}C Pyruvate ($^{14}CO_2$ DPM)
8000
6000
4000
2000
0
*
Ctl
IAV
D.
Glutaminolysis
^{14}C U-Glutamine ($^{14}CO_2$ DPM)
8000
6000
4000
2000
0
*
Ctl
IAV
E.
Fatty Acid β-Oxidation
9,10-^{3}H Palmitate (^3H_2O (DPM)
8000
6000
4000
2000
0
Ctl
IAV
F.
Free Fatty Acids
Fatty Acids (nmol/2.5x10^5 cells)
15
10
5
0
*
Ctl
IAV
G.
Capacity
PYR + GLN + FA Oxidation (%)
60
40
20
0
*
Ctl
IAV
H.
Dependency
PYR + GLN + FA Oxidation (%)
60
40
20
0
Ctl
IAV
I.
Flexibility
PYR + GLN + FA Oxidation (%)
50
40
30
20
10
0
*
Ctl
IAV

Figure 2

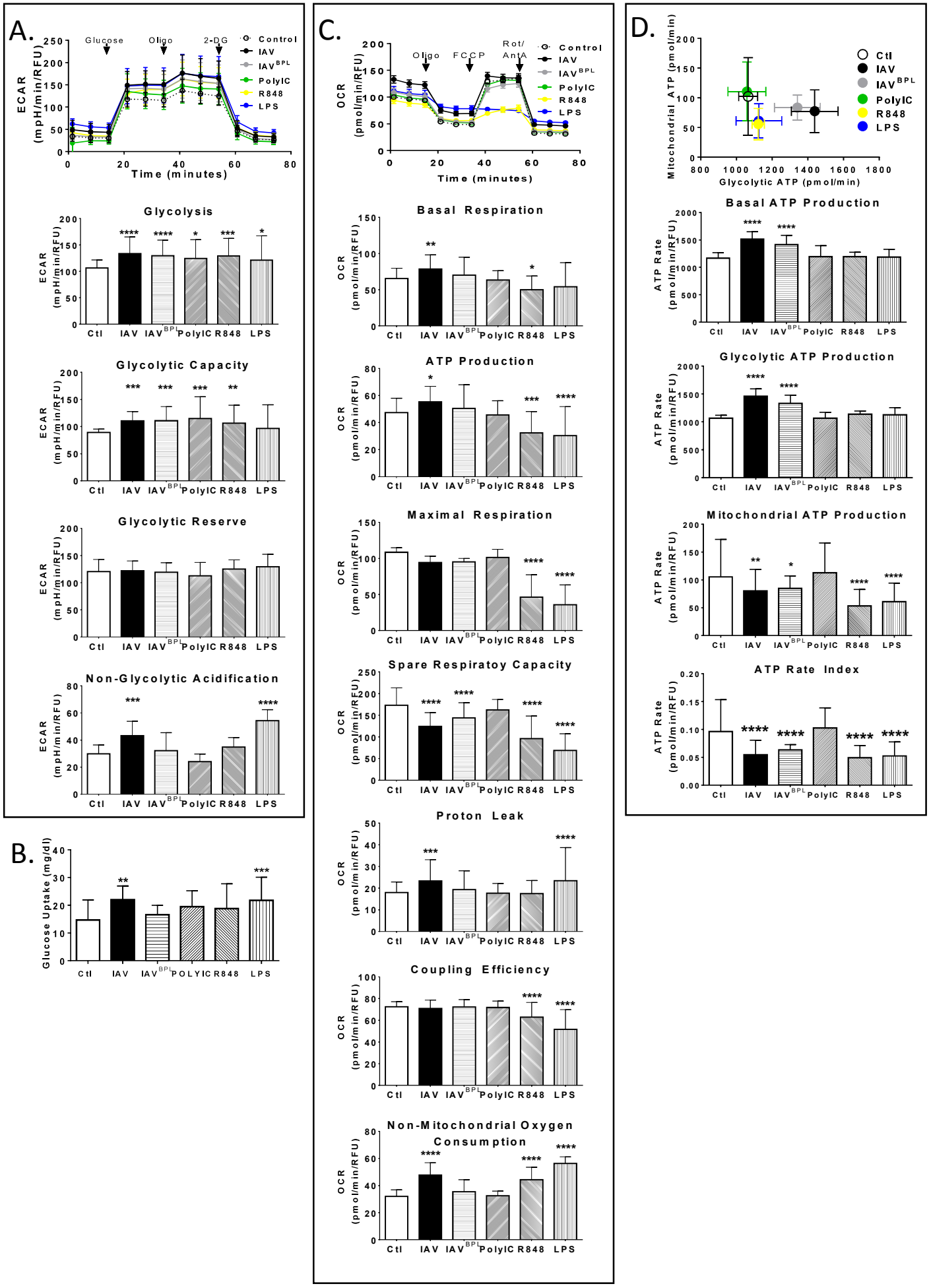
A.
Glucose
Oligo
2-DG
Control
IAV
IAV BPL
PolyIC
R848
LPS
ECAR (mpH/min/RFU)
Time (minutes)
Glycolysis
Glycolytic Capacity
Glycolytic Reserve
Non-Glycolytic Acidification
B.
Glucose Uptake (mg/dl)
C.
Oligo
FCCP
Rot/ AntA
OCR (pmol/min/RFU)
Basal Respiration
ATP Production
Maximal Respiration
Spare Respiratoy Capacity
Proton Leak
Coupling Efficiency
Non-Mitochondrial Oxygen Consumption
D.
Mitochondrial ATP (pmol/min)
Glycolytic ATP (pmol/min)
Ctl
Basal ATP Production
Glycolytic ATP Production
Mitochondrial ATP Production
ATP Rate Index
ATP Rate (pmol/min/RFU)

Figure 3

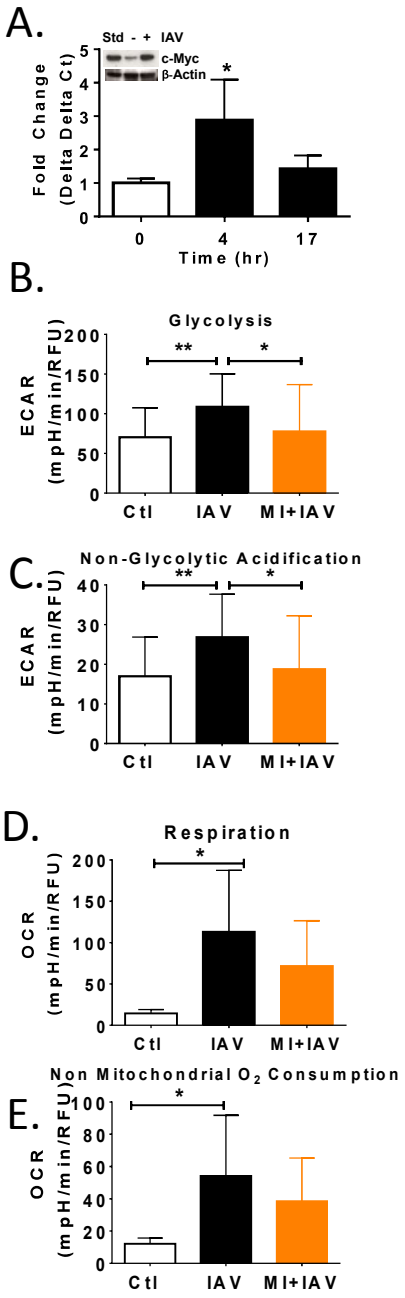
A.
Std - + IAV
c-Myc
β-Actin
Fold Change (Delta Delta Ct)
Time (hr)
B.
Glycolysis
ECAR (mpH/min/RFU)
Ctl
IAV
MI+IAV
C.
Non-Glycolytic Acidification
ECAR (mpH/min/RFU)
D.
Respiration
OCR (mpH/min/RFU)
E.
Non Mitochondrial O2 Consumption
OCR (mpH/min/RFU)

Figure 4

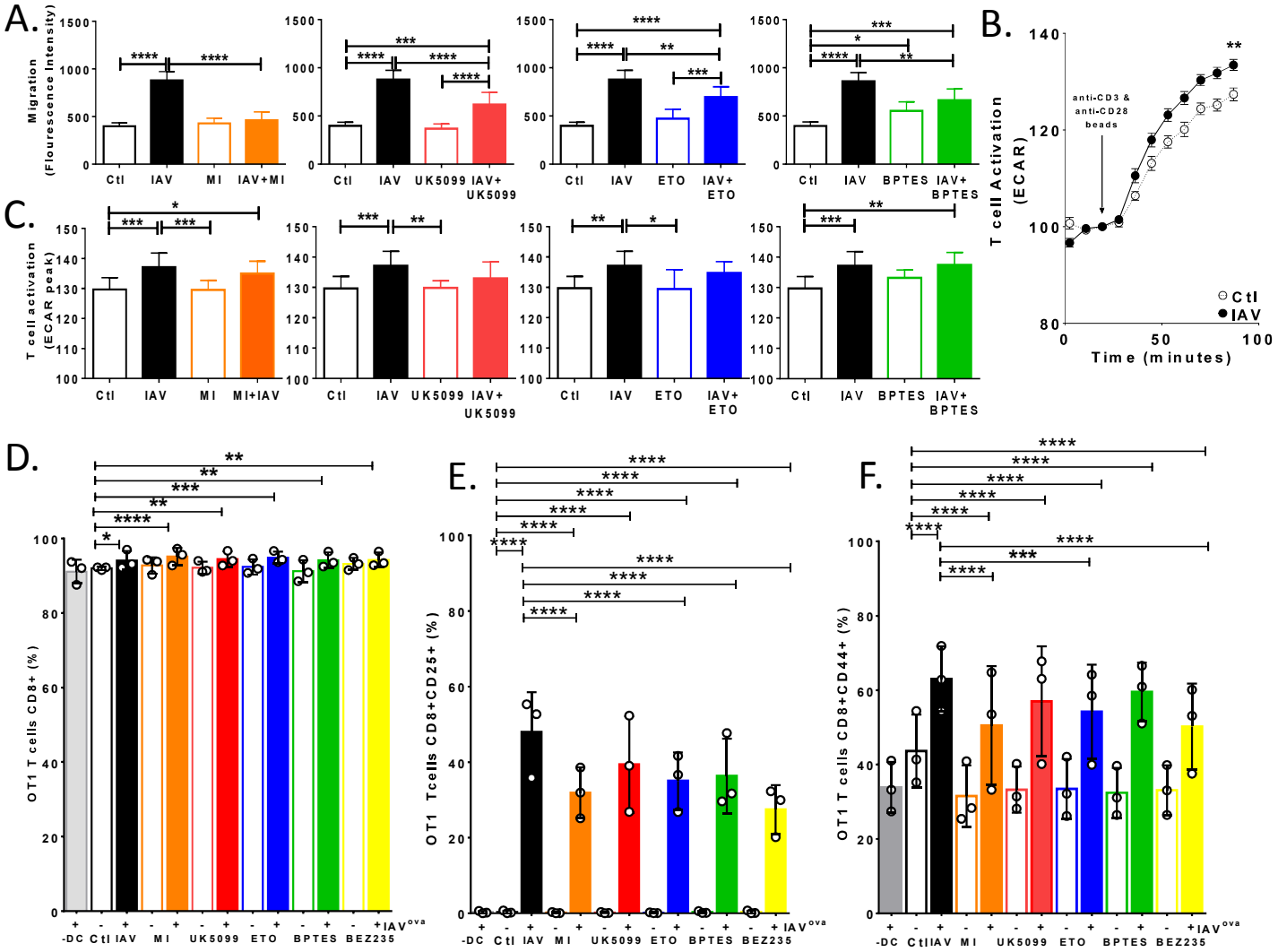
A.
Migration (Flourescence Intensity)
Ctl
IAV
MI
IAV+MI
UK5099
IAV+ UK5099
ETO
IAV+ ETO
BPTES
IAV+ BPTES
B.
T cell Activation (ECAR)
anti-CD3 & anti-CD28 beads
Ctl
IAV
Time (minutes)
C.
T cell activation (ECAR peak)
MI+IAV
D.
OT1 T cells CD8+ (%)
-DC
BEZ235
IAV ova
E.
OT1 Tcells CD8+CD25+ (%)
F.
OT1 T cells CD8+CD44+ (%)

Figure 5

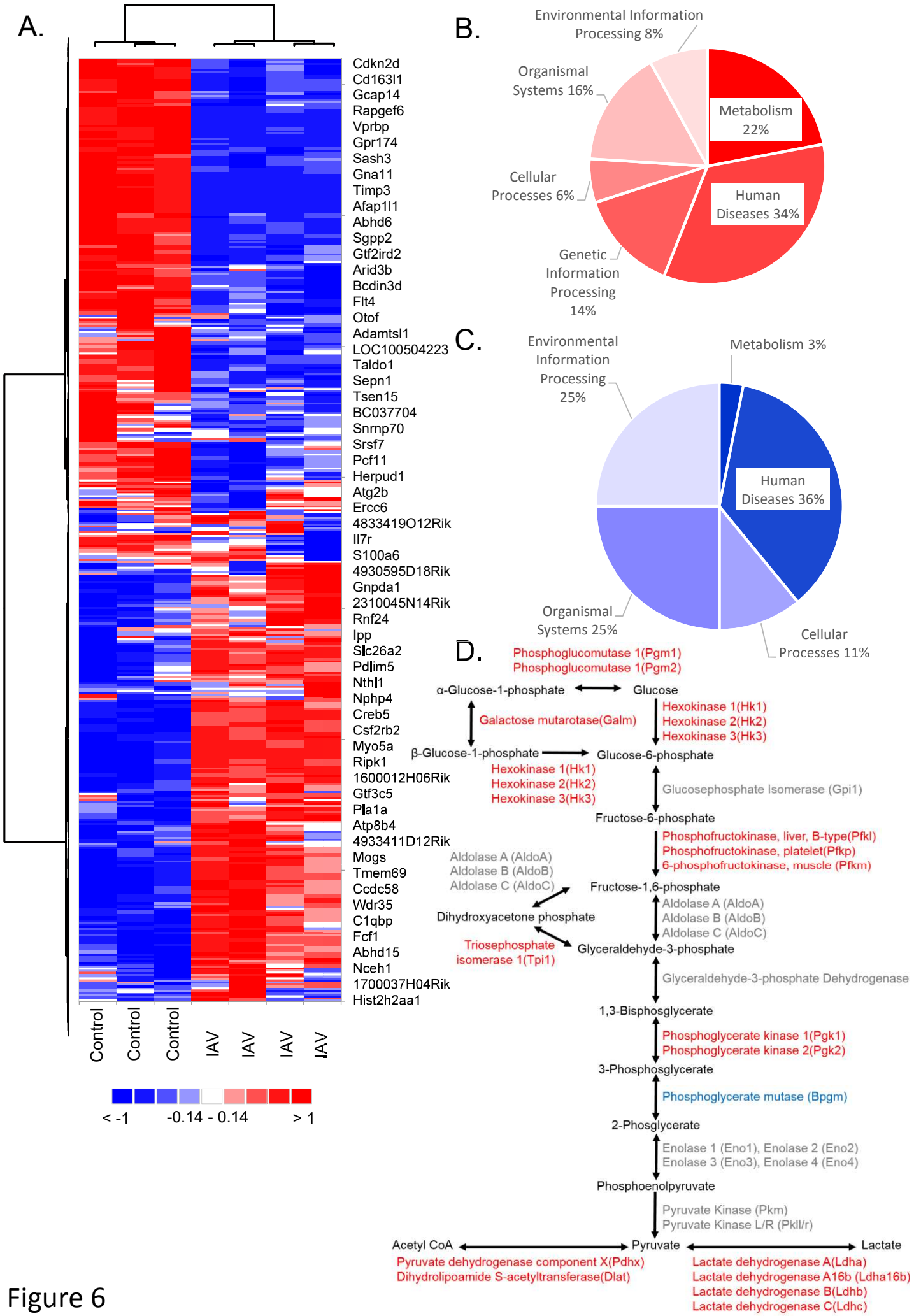
A.
Cdkn2d
Cd163l1
Gcap14
Rapgef6
Vprbp
Gpr174
Sash3
Gna11
Timp3
Afap1l1
Abhd6
Sgpp2
Gtf2ird2
Arid3b
Bcdin3d
Flt4
Otof
Adamtsl1
LOC100504223
Taldo1
Sepn1
Tsen15
BC037704
Snrnp70
Srsf7
Pcf11
Herpud1
Atg2b
Ercc6
4833419O12Rik
Il7r
S100a6
4930595D18Rik
Gnpda1
2310045N14Rik
Rnf24
Ipp
Slc26a2
Pdlim5
Nthl1
Nphp4
Creb5
Csf2rb2
Myo5a
Ripk1
1600012H06Rik
Gtf3c5
Pla1a
Atp8b4
4933411D12Rik
Mogs
Tmem69
Ccdc58
Wdr35
C1qbp
Fcf1
Abhd15
Nceh1
1700037H04Rik
Hist2h2aa1
Control
Control
Control
IAV
IAV
IAV
IAV
< -1
-0.14 - 0.14
> 1
B.
Environmental Information Processing 8%
Organismal Systems 16%
Metabolism 22%
Cellular Processes 6%
Human Diseases 34%
Genetic Information Processing 14%
C.
Environmental Information Processing 25%
Metabolism 3%
Human Diseases 36%
Organismal Systems 25%
Cellular Processes 11%
D.
Phosphoglucomutase 1(Pgm1)
Phosphoglucomutase 1(Pgm2)
α-Glucose-1-phosphate
Glucose
Galactose mutarotase(Galm)
Hexokinase 1(Hk1)
Hexokinase 2(Hk2)
Hexokinase 3(Hk3)
β-Glucose-1-phosphate
Glucose-6-phosphate
Hexokinase 1(Hk1)
Hexokinase 2(Hk2)
Hexokinase 3(Hk3)
Glucosephosphate Isomerase (Gpi1)
Fructose-6-phosphate
Phosphofructokinase, liver, B-type(Pfkl)
Phosphofructokinase, platelet(Pfkp)
6-phosphofructokinase, muscle (Pfkm)
Aldolase A (AldoA)
Aldolase B (AldoB)
Aldolase C (AldoC)
Fructose-1,6-phosphate
Aldolase A (AldoA)
Aldolase B (AldoB)
Aldolase C (AldoC)
Dihydroxyacetone phosphate
Triosephosphate isomerase 1(Tpi1)
Glyceraldehyde-3-phosphate
Glyceraldehyde-3-phosphate Dehydrogenase
1,3-Bisphosglycerate
Phosphoglycerate kinase 1(Pgk1)
Phosphoglycerate kinase 2(Pgk2)
3-Phosphosglycerate
Phosphoglycerate mutase (Bpgm)
2-Phosglycerate
Enolase 1 (Eno1), Enolase 2 (Eno2)
Enolase 3 (Eno3), Enolase 4 (Eno4)
Phosphoenolpyruvate
Pyruvate Kinase (Pkm)
Pyruvate Kinase L/R (Pkll/r)
Acetyl CoA
Pyruvate
Lactate
Pyruvate dehydrogenase component X(Pdhx)
Dihydrolipoamide S-acetyltransferase(Dlat)
Lactate dehydrogenase A(Ldha)
Lactate dehydrogenase A16b (Ldha16b)
Lactate dehydrogenase B(Ldhb)
Lactate dehydrogenase C(Ldhc)

Figure 6

A.

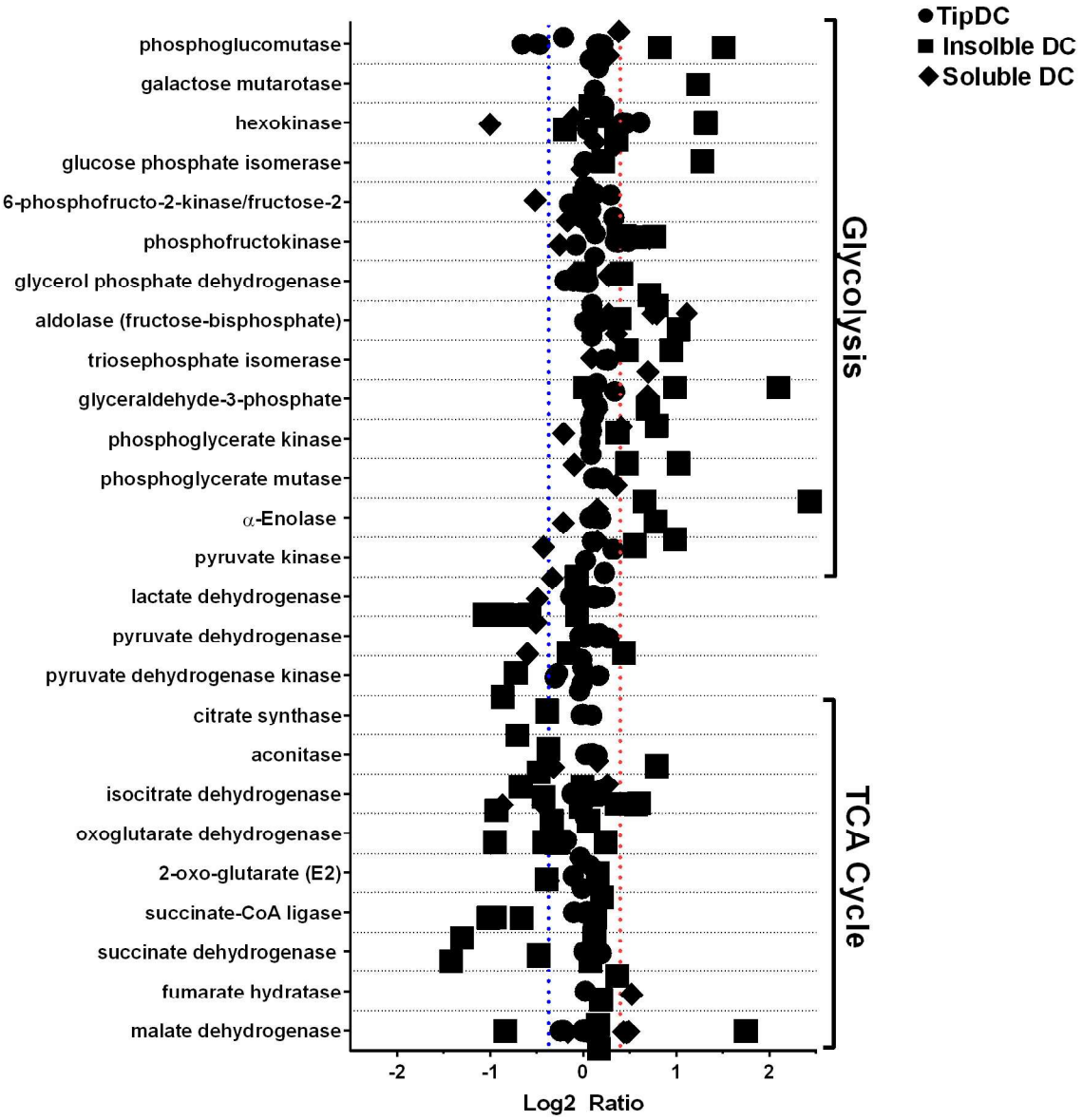
TipDC
Insolble DC
Soluble DC
phosphoglucomutase
galactose mutarotase
hexokinase
glucose phosphate isomerase
6-phosphofructo-2-kinase/fructose-2
phosphofructokinase
glycerol phosphate dehydrogenase
aldolase (fructose-bisphosphate)
triosephosphate isomerase
glyceraldehyde-3-phosphate
phosphoglycerate kinase
phosphoglycerate mutase
α-Enolase
pyruvate kinase
lactate dehydrogenase
pyruvate dehydrogenase
pyruvate dehydrogenase kinase
citrate synthase
aconitase
isocitrate dehydrogenase
oxoglutarate dehydrogenase
2-oxo-glutarate (E2)
succinate-CoA ligase
succinate dehydrogenase
fumarate hydratase
malate dehydrogenase
Glycolysis
TCA Cycle
-2
-1
0
1
2
Log2 Ratio

B.

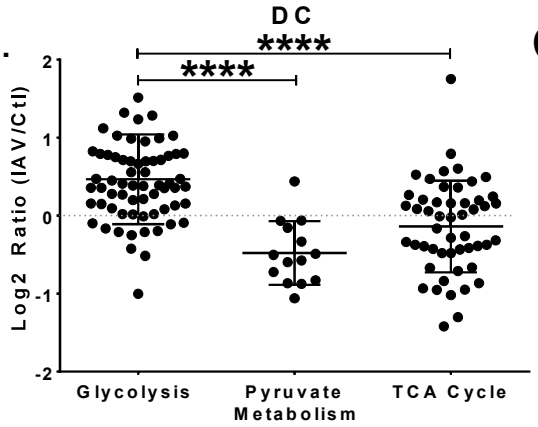
DC
****
****
Log2 Ratio (IAV/Ctl)
2
1
0
-1
-2
Glycolysis
Pyruvate Metabolism
TCA Cycle

C.

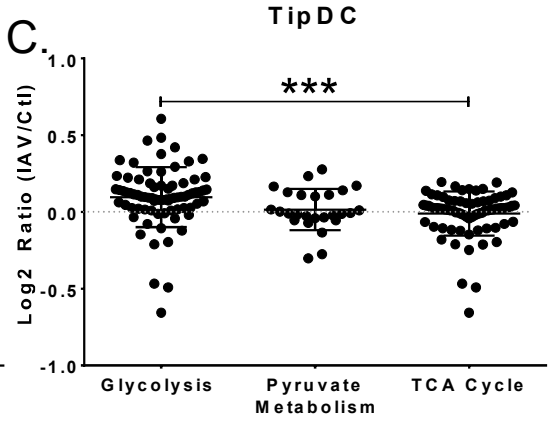
TipDC
***
Log2 Ratio (IAV/Ctl)
1.0
0.5
0.0
-0.5
-1.0
Glycolysis
Pyruvate Metabolism
TCA Cycle

Figure 7

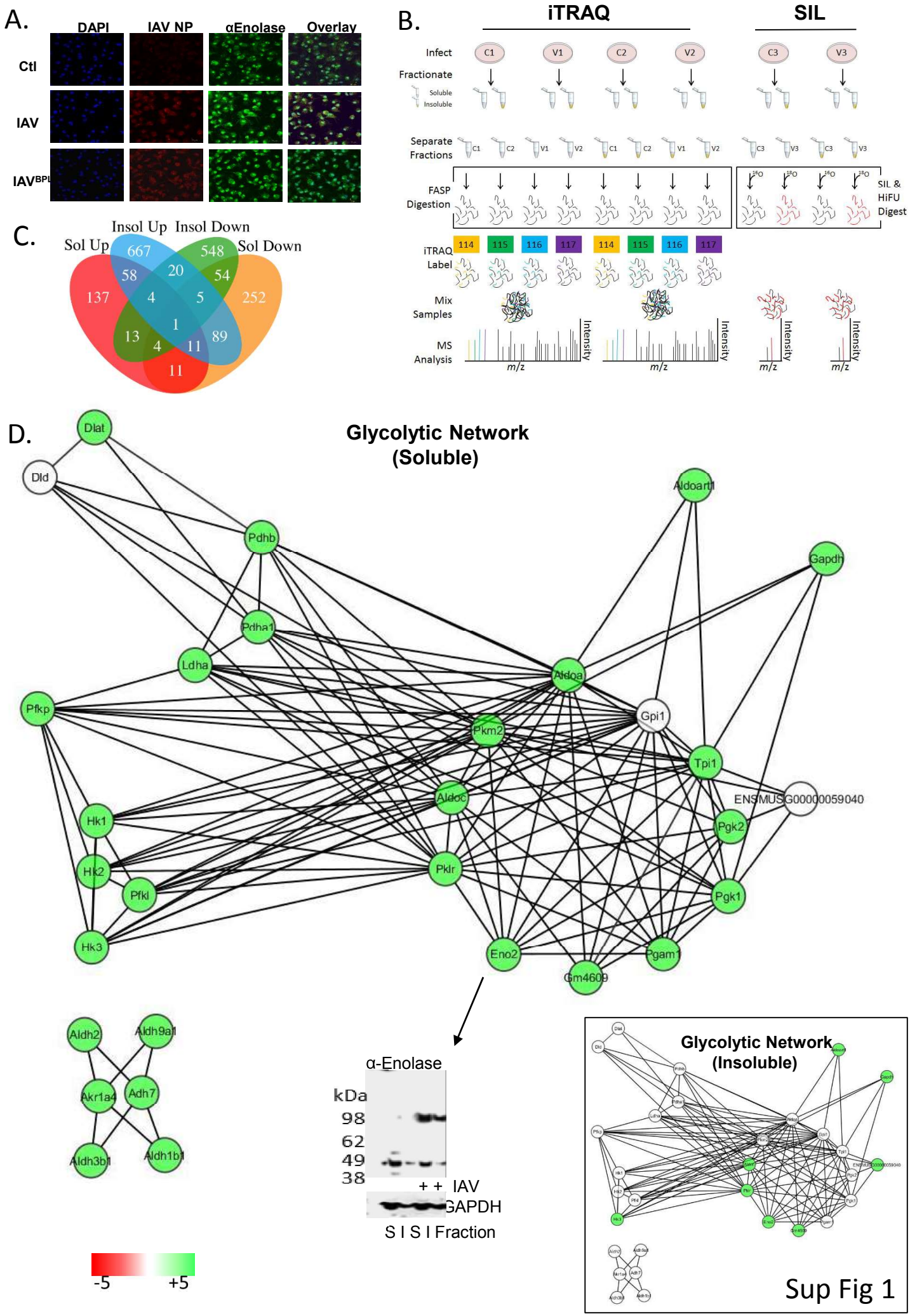
A.
DAPI
IAV NP
αEnolase
Overlay
Ctl
IAV
IAVBPL
B.
iTRAQ
SIL
Infect
C1
V1
C2
V2
C3
V3
Fractionate
Soluble
Insoluble
Separate Fractions
FASP Digestion
SIL & HiFU Digest
iTRAQ Label
114
115
116
117
Mix Samples
MS Analysis
Intensity
m/z
C.
Insol Up
Insol Down
Sol Up
Sol Down
667
548
58
20
54
137
4
5
252
1
13
4
11
89
11
D.
Glycolytic Network (Soluble)
Dlat
Dld
Pdhb
Pdha1
Ldha
Pfkp
Hk1
Hk2
Pfkl
Hk3
Aldoartl
Gapdh
Aldoa
Gpi1
Pkm2
Tpi1
Aldoc
ENSMUSG00000059040
Pgk2
Pklr
Pgk1
Eno2
Pgam1
Gm4609
Aldh2
Aldh9a1
Akr1a4
Adh7
Aldh3b1
Aldh1b1
-5
+5
α-Enolase
kDa
98
62
49
38
+ + IAV
GAPDH
S I S I Fraction
Glycolytic Network (Insoluble)
Sup Fig 1

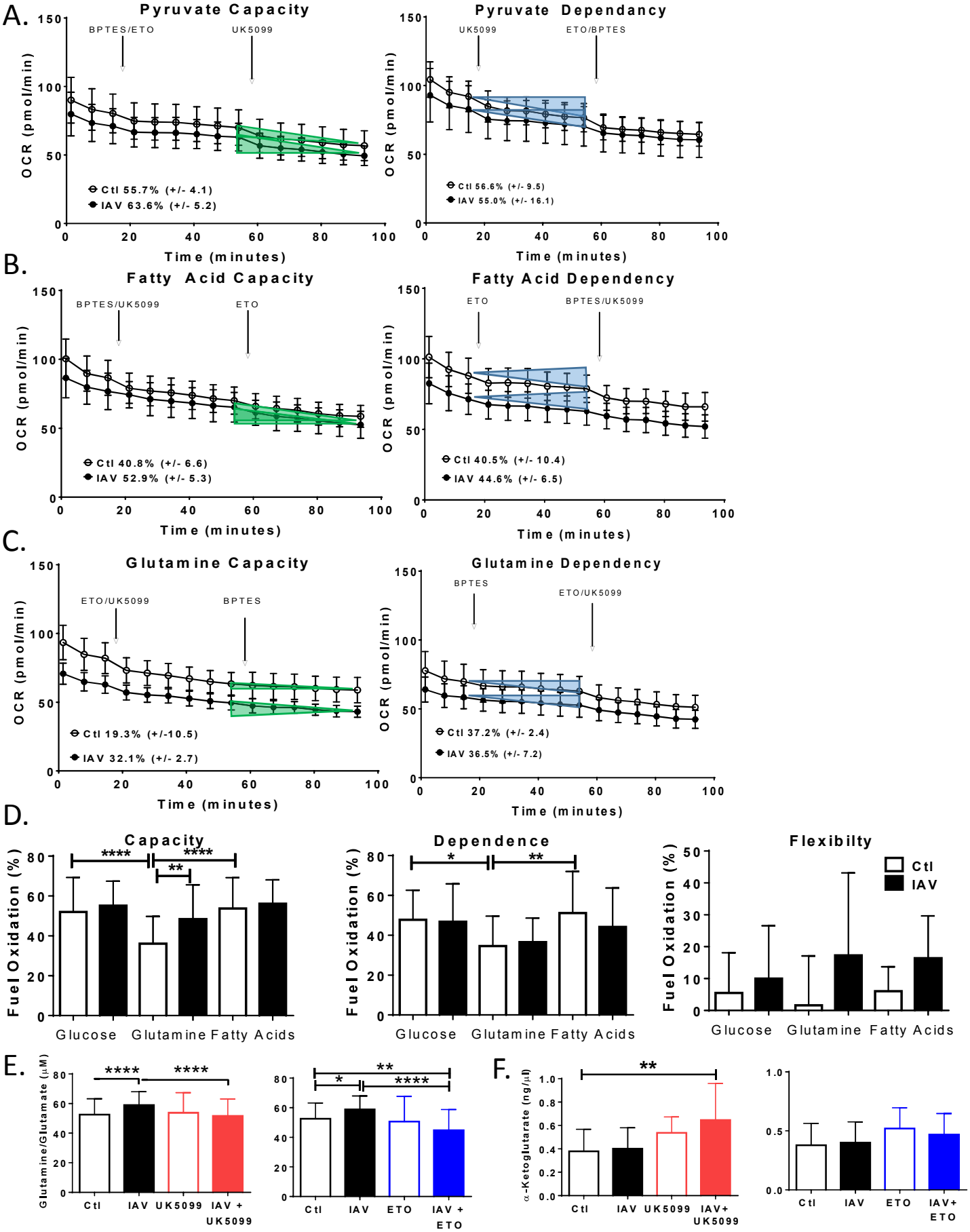
A.
Pyruvate Capacity
BPTES/ETO
UK5099
OCR (pmol/min)
Ctl 55.7% (+/- 4.1)
IAV 63.6% (+/- 5.2)
Time (minutes)
Pyruvate Dependancy
UK5099
ETO/BPTES
Ctl 56.6% (+/- 9.5)
IAV 55.0% (+/- 16.1)
B.
Fatty Acid Capacity
BPTES/UK5099
ETO
Ctl 40.8% (+/- 6.6)
IAV 52.9% (+/- 5.3)
Fatty Acid Dependency
ETO
BPTES/UK5099
Ctl 40.5% (+/- 10.4)
IAV 44.6% (+/- 6.5)
C.
Glutamine Capacity
ETO/UK5099
BPTES
Ctl 19.3% (+/-10.5)
IAV 32.1% (+/- 2.7)
Glutamine Dependency
BPTES
ETO/UK5099
Ctl 37.2% (+/- 2.4)
IAV 36.5% (+/- 7.2)
D.
Capacity
Fuel Oxidation (%)
Glucose
Glutamine
Fatty Acids
Dependence
Flexibilty
Ctl
IAV
E.
Glutamine/Glutamate (µM)
Ctl
IAV
UK5099
IAV + UK5099
ETO
IAV + ETO
F.
α-Ketoglutarate (ng/µl)
IAV+ UK5099
IAV+ ETO

Sup Fig 2

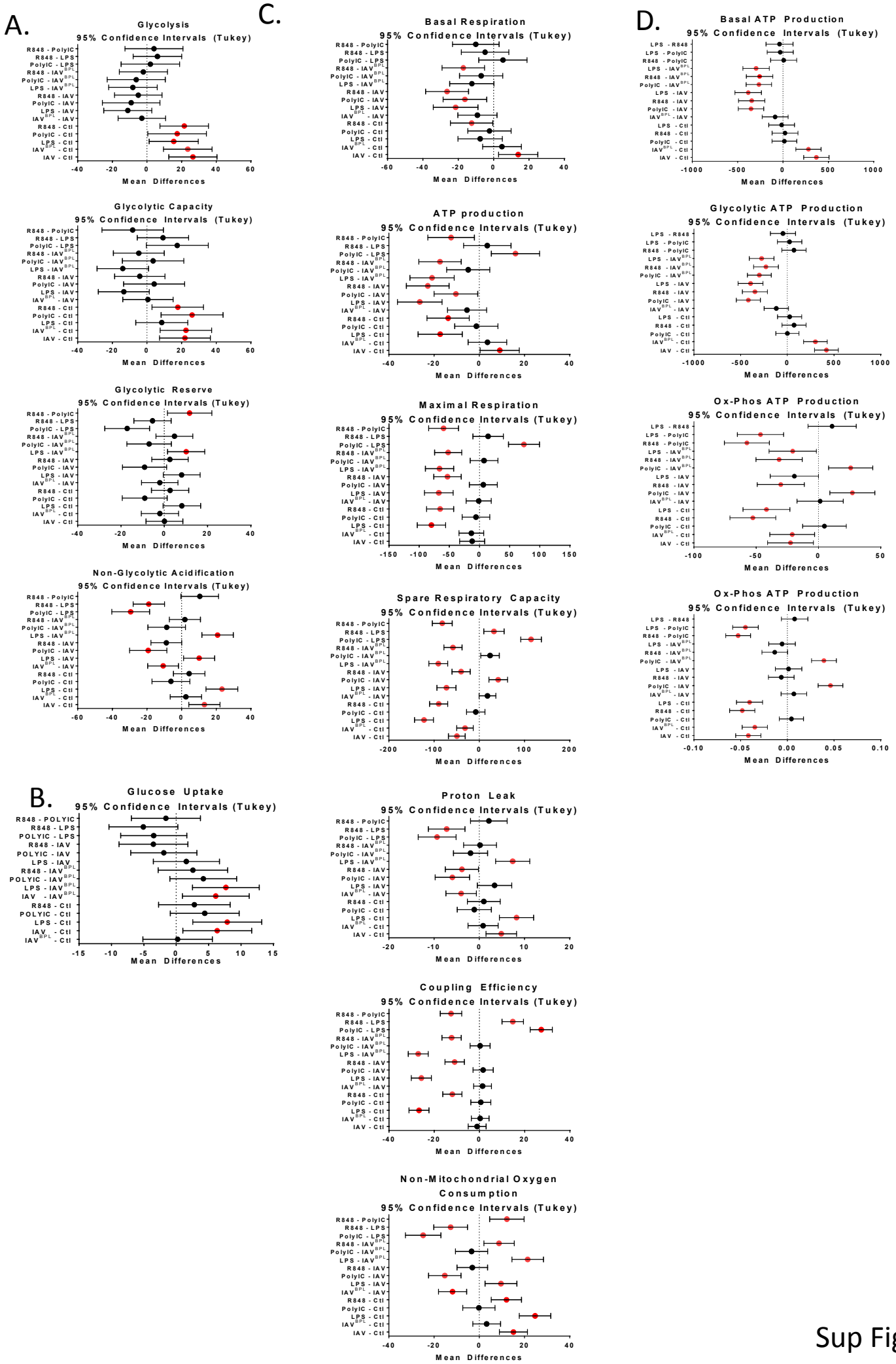
A.
Glycolysis
95% Confidence Intervals (Tukey)
R848 - PolyIC
R848 - LPS
PolyIC - LPS
R848 - IAV^BPL
PolyIC - IAV^BPL
LPS - IAV^BPL
R848 - IAV
PolyIC - IAV
LPS - IAV
IAV^BPL - IAV
R848 - Ctl
PolyIC - Ctl
LPS - Ctl
IAV^BPL - Ctl
IAV - Ctl
-40 -20 0 20 40 60
Mean Differences
Glycolytic Capacity
95% Confidence Intervals (Tukey)
-40 -20 0 20 40 60
Mean Differences
Glycolytic Reserve
95% Confidence Intervals (Tukey)
-40 -20 0 20 40
Mean Differences
Non-Glycolytic Acidification
95% Confidence Intervals (Tukey)
-60 -40 -20 0 20 40
Mean Differences
B.
Glucose Uptake
95% Confidence Intervals (Tukey)
R848 - POLYIC
R848 - LPS
POLYIC - LPS
R848 - IAV
POLYIC - IAV
LPS - IAV
R848 - IAV^BPL
POLYIC - IAV^BPL
LPS - IAV^BPL
IAV - IAV^BPL
R848 - Ctl
POLYIC - Ctl
LPS - Ctl
IAV - Ctl
IAV^BPL - Ctl
-15 -10 -5 0 5 10 15
Mean Differences
C.
Basal Respiration
95% Confidence Intervals (Tukey)
-60 -40 -20 0 20 40
Mean Differences
ATP production
95% Confidence Intervals (Tukey)
-40 -20 0 20 40
Mean Differences
Maximal Respiration
95% Confidence Intervals (Tukey)
-150 -100 -50 0 50 100 150
Mean Differences
Spare Respiratory Capacity
95% Confidence Intervals (Tukey)
-200 -100 0 100 200
Mean Differences
Proton Leak
95% Confidence Intervals (Tukey)
-20 -10 0 10 20
Mean Differences
Coupling Efficiency
95% Confidence Intervals (Tukey)
-40 -20 0 20 40
Mean Differences
Non-Mitochondrial Oxygen Consumption
95% Confidence Intervals (Tukey)
-40 -20 0 20 40
Mean Differences
D.
Basal ATP Production
95% Confidence Intervals (Tukey)
LPS - R848
LPS - PolyIC
R848 - PolyIC
LPS - IAV^BPL
R848 - IAV^BPL
PolyIC - IAV^BPL
LPS - IAV
R848 - IAV
PolyIC - IAV
IAV^BPL - IAV
LPS - Ctl
R848 - Ctl
PolyIC - Ctl
IAV^BPL - Ctl
IAV - Ctl
-1000 -500 0 500 1000
Mean Differences
Glycolytic ATP Production
95% Confidence Intervals (Tukey)
-1000 -500 0 500 1000
Mean Differences
Ox-Phos ATP Production
95% Confidence Intervals (Tukey)
-100 -50 0 50
Mean Differences
Ox-Phos ATP Production
95% Confidence Intervals (Tukey)
-0.10 -0.05 0.00 0.05 0.10
Mean Differences

Sup Fig 3

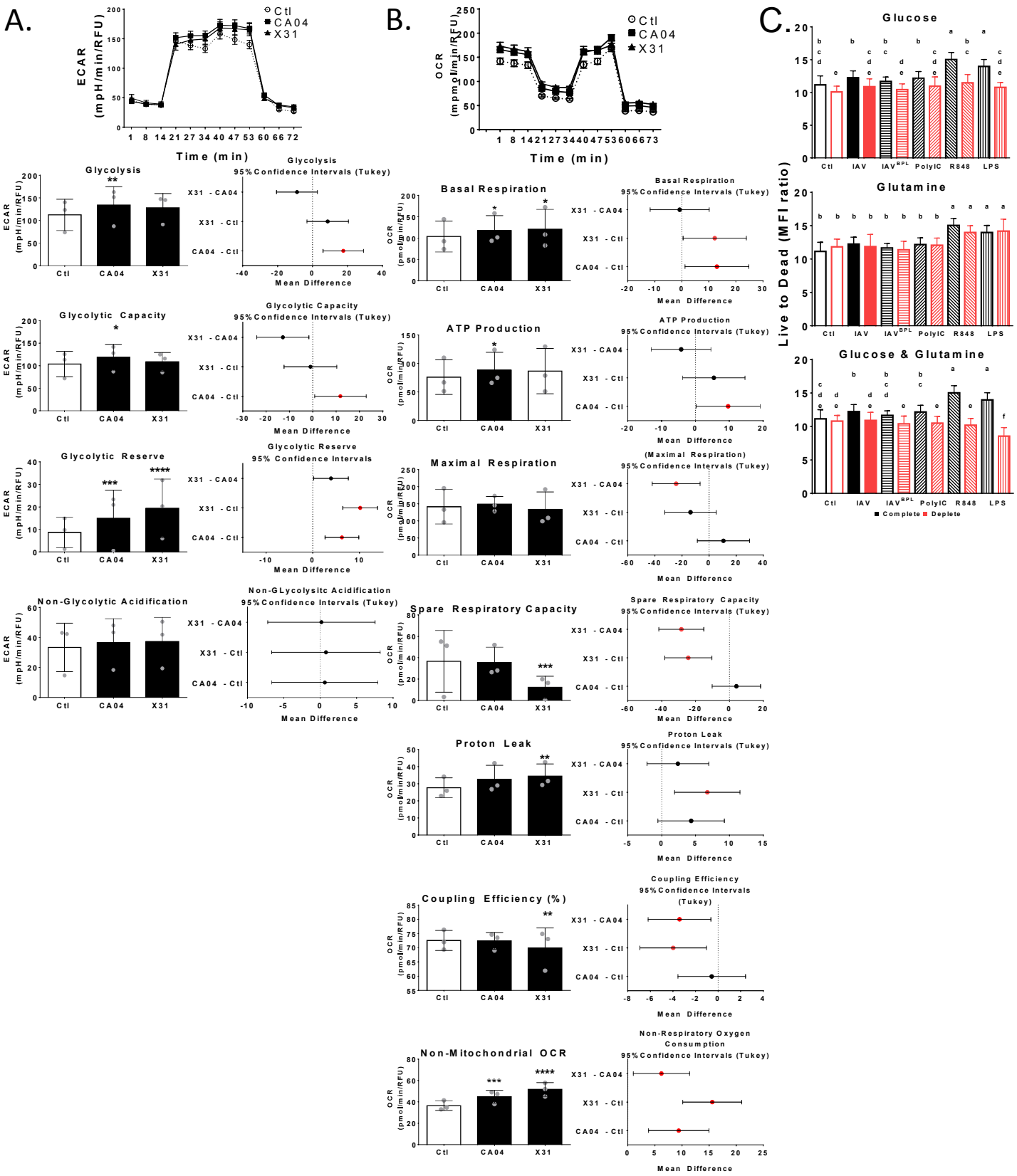
A.
B.
C.
Ctl
CA04
X31
ECAR (mpH/min/RFU)
OCR (pmol/min/RFU)
Time (min)
Glycolysis
Glycolytic Capacity
Glycolytic Reserve
Non-Glycolytic Acidification
Basal Respiration
ATP Production
Maximal Respiration
Spare Respiratory Capacity
Proton Leak
Coupling Efficiency (%)
Non-Mitochondrial OCR
95% Confidence Intervals (Tukey)
Mean Difference
Glucose
Glutamine
Glucose & Glutamine
Live to Dead (MFI ratio)
IAV
IAV BPL
PolyIC
R848
LPS
Complete
Deplete

Sup Fig 4

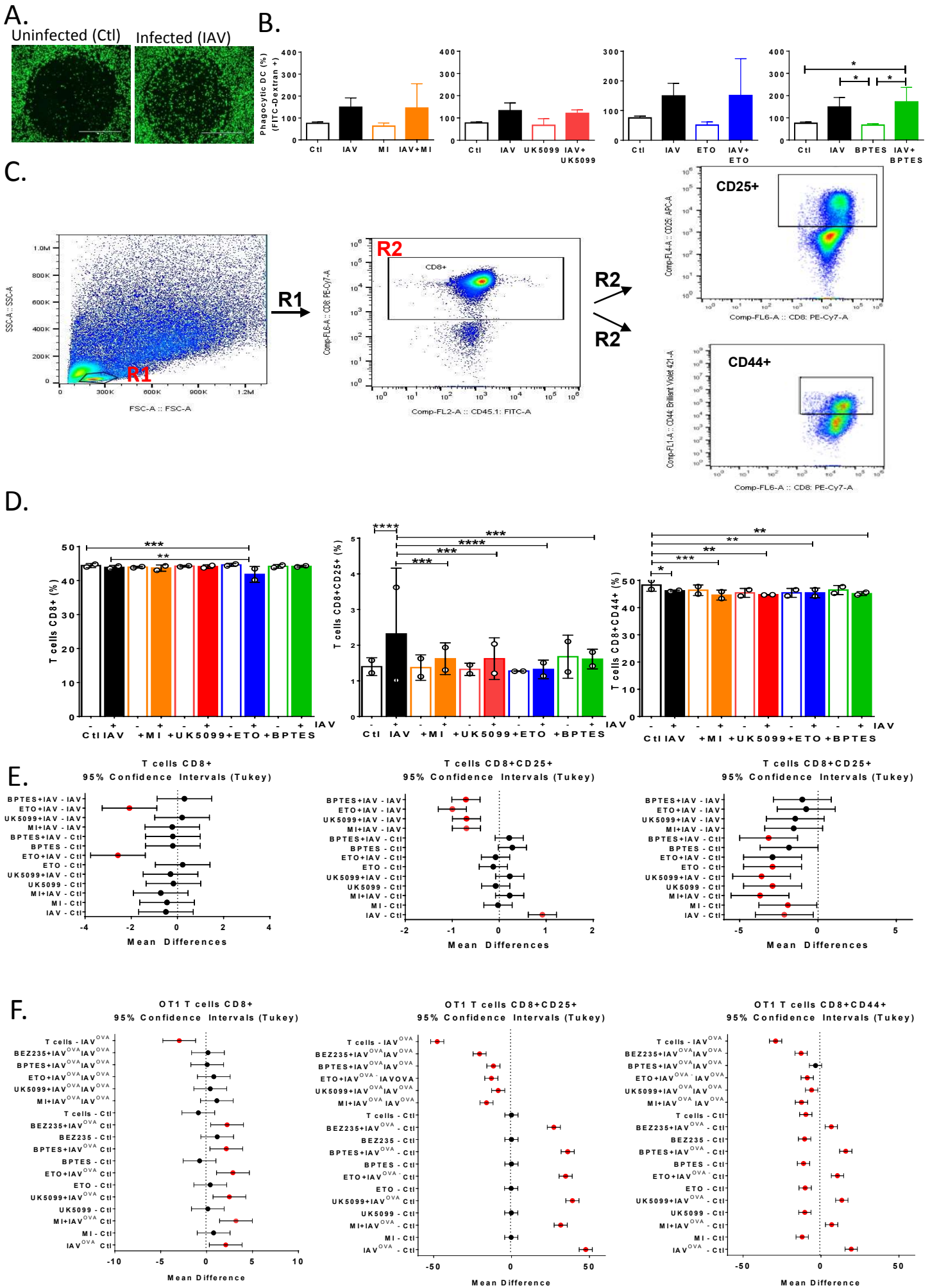
A.
Uninfected (Ctl)
Infected (IAV)
B.
Phagocytic DC (%) (FITC-Dextran +)
Ctl
IAV
MI
IAV+MI
UK5099
IAV+ UK5099
ETO
IAV+ ETO
BPTES
IAV+ BPTES
C.
R1
R2
CD8+
CD25+
CD44+
SSC-A :: SSC-A
FSC-A :: FSC-A
Comp-FL6-A :: CD8: PE-Cy7-A
Comp-FL2-A :: CD45.1: FITC-A
Comp-FL4-A :: CD25: APC-A
Comp-FL1-A :: CD44: Brilliant Violet 421-A
D.
T cells CD8+ (%)
T cells CD8+CD25+ (%)
T cells CD8+CD44+ (%)
Ctl IAV +MI +UK5099+ETO +BPTES
E.
T cells CD8+
95% Confidence Intervals (Tukey)
T cells CD8+CD25+
Mean Differences
F.
OT1 T cells CD8+
OT1 T cells CD8+CD25+
OT1 T cells CD8+CD44+
Mean Difference

Sup Fig 5

A.

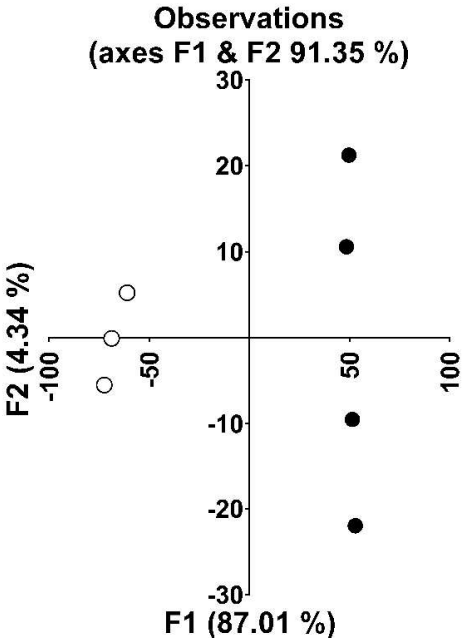
Observations
(axes F1 & F2 91.35 %)
30
20
10
-10
-20
-30
-100
-50
50
100
F2 (4.34 %)
F1 (87.01 %)

B.

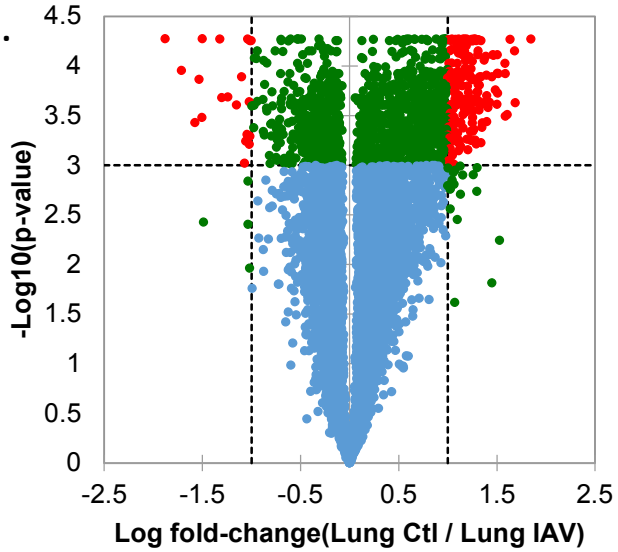
4.5
4
3.5
3
2.5
2
1.5
1
0.5
0
-2.5
-1.5
-0.5
0.5
1.5
2.5
-Log10(p-value)
Log fold-change(Lung Ctl / Lung IAV)

Sup Fig 6